Mars in Multi-Dimensions
—
A Global Geological Survey

Oscar Matthijs Kamps

MARS IN MULTI-DIMENSIONS
—
A GLOBAL GEOLOGICAL SURVEY

DISSERTATION

to obtain
the degree of doctor at the University of Twente,
on the authority of the rector magnificus,
Prof. dr. ir. A. Veldkamp,
on account of the decision of the Doctorate Board,
to be publicly defended
on 10^{th} of March 2021 at 16.45

by

Oscar Matthijs Kamps
born on March 16, 1992
in Purmerend, The Netherlands

This dissertation has been approved by:

Prof. dr. F. D. van der Meer (supervisor)
Dr. R.D. Hewson (co-supervisor)
Dr. F.J.A van Ruitenbeek (co-supervisor)

ITC dissertation number 393
ITC, P.O. Box 217, 7500 AE Enschede, The Netherlands

ISBN: 978-90-365-51427
DOI: http://dx.doi.org/10.3990//1.97890365
Printed by: CTRL-P, Enschende, Netherlands

Graduation committee:

Chairman/secretary:
Dean of ITC
Supervisor:
Prof. dr. F.D. van der Meer
Co-supervisors:
Dr. F.J.A. van Ruitenbeek
Dr. R.D. Hewson

Committee members:
Prof. dr. V.G. Jetten (*University of Twente*)
Prof. dr. M. van der Meijde (*University of Twente*)
Prof. dr. C.E. Viviano (*John Hopkins University – Applied Physics Laboratory*)
Prof. dr. B.H. Foing (*Vrije Universiteit Amsterdam/*
European Space Research and Technology Centre)
Prof. dr. H. Hiesinger (*Westfälische Wilhelms – Universität Münster*)

I would like to dedicate this thesis to my grandfather, Piet Struik

Summary

The availability of global orbital data has advanced the understanding of the geology of Mars. However, the limited availability of verification data complicates the interpretation of the data, resulting in multiple hypotheses on the geological history and past conditions to explain interpreted mineralogical- and geochemical differences. Also, it is unlikely that sufficient in-situ validation data will be available in the near future to explain such differences. For this reason, the research performed in this thesis is initiated with the purpose that new global perspectives on the Martian geology can come from either new orbital datasets or the use of novel analysis techniques on existing data. The title "Mars in multi-dimensions" can be explained in multiple ways. It refers to the multi-dimensions of multi-variate data analysis techniques applied in most of the studies within this thesis, and refers to the different dimensions or perspectives of the different orbital instruments used in this study to characterize mineralogy and geochemistry.

The CRISM (Compact Reconnaissance Imaging Spectrometer) mapping mode data is used to develop new global maps indicating the important spectral features characteristic for primary mafic and secondary alteration minerals. Because of known difficulties with this data, such as observational differences between different orbit observations and the shallow nature of some spectral absorption features, the global mapping mode dataset of the CRISM is a rarely used dataset for global mapping. This mapping and characterizing the surface geology and composition was one of the pre-defined primary goals of the CRISM instrument. The results have shown that distinct compositional provinces on Mars can be characterized by the CRISM dataset. Besides this study's consistent results with previous global mineralogical studies, the data has provided new perspectives by classifying new regions that are potentially geologically interesting regions, around for example Hellas Basin and Ophir Planum.

After demonstrating the geological mapping potential of the CRISM data, the data is used as input for quantitative modeling of the Gamma-Ray Spectrometer (GRS) geochemical element concentrations. Studying these element distributions is challenging due to the coarse spatial resolution of this data (e.g. 5^o x 5^o). Using quantitative modeling of the GRS data, statistical, robust and transparent comparisons between mineralogical information and the element concentration was undertaken. The results have shown how well the datasets relate to each other and which CRISM derived summary products contribute most to the model. With these modeling results, local anomalies in the element concentrations are interpreted for geological processes based on their geochemical and mineralogical nature.

The interpretations of the Martian surface geology are supported here by Mars analog rock analysis. In this thesis, a variety of sedimentary, volcanic and altered rocks are studied with geochemical analysis as well as imaging and point spectroscopy. A selection of Pilbara greenstone rocks, which are similar in age and composition as the rocks on Mars, are studied to test whether the absorption wavelengths of chlorite can be used to distinguish hydrothermal alteration from metamorphosed rocks. In addition, a selection of rocks, considered as Mars analog rocks, from the geoscience lab of ITC were measured with imaging spectrometers. By calculating the same equivalent summary products as those derived from CRISM for Mars, it was possible to evaluate these products for their intended mineralogy and possible alternative interpretations.

In conclusion, despite the earlier mentioned difficulties with the CRISM data, the exploratory work in this thesis has indicated the potential of this dataset for geological remote sensing. The surface type classification using the CRISM data has provided new information of earlier defined surface types but also described regions that are not described before by previous surface type studies. The predictive modeling of the geochemical element concentrations has quantified the relation between this geochemical dataset with mineralogical infrared data. The importance of the spectral parameters for the model was used to locally interpret the geology based on geochemical and mineralogical data resulting in new perspectives on the geological history. The spectral measurements of Mars analog rocks were found useful to verify the interpretation of the commonly used spectral parameters for Martian remote sensing. It showed the usefulness of spectral parameters to describe the intended spectral features of minerals but also the alternative interpretations for other minerals. Many questions remain regarding the geological history of Mars, but with the work in this thesis, presenting new data and novel application of statistical analysis, has shown to be a valuable addition to the current understanding of the Martian geology.

Samenvatting

De beschikbaarheid van satellietdata in banen om Mars heeft gezorgd voor veel kennis over zijn geologische geschiedenis. Er bestaat echter weinig verificatiedata, waardoor er verschillende hypotheses zijn ontwikkeld over de geologische geschiedenis en de geologische omstandigheden die de mineralogische- en geochemische verschillen op de planeet beschrijven. Het is onwaarschijnlijk dat deze validatie data in de nabije toekomst wel voldoende beschikbaar is. Daarom zullen nieuwe globale inzichten van de geologie van Mars moeten komen van nieuwe satellietdata of van het gebruik van innovatieve analyses op huidige datasets. Dit is de inspiratie geweest voor het onderzoek van dit proefschrift. De titel “Mars in multi-dimensions” (oftewel: Mars in meerdere dimensies) kan op verschillende manieren worden uitgelegd. Het verwijst ten eerste naar meerdere dimensies van de statistische multivariate analyses toegepast in de meeste onderzoeken in dit proefschrift. Daarnaast verwijst het ook naar de verschillende dimensies, of perspectieven, van de verschillende satellietinstrumenten.

Data van de CRISM (Compact Reconnaissance Imaging Spectrometer) mapping mode is gebruikt om nieuwe globale kaarten te maken van de belangrijke spectrale eigenschappen karakteristiek voor mafische vulkanische, of alteratie mineralen. Vanwege de al bekende uitdagingen met deze dataset, zoals verschillen tussen orbitale observaties en kleine veranderingen in het absorptie spectrum, is de CRISM data een weinig gebruikte data voor globale onderzoeken. Toch is het in kaart brengen en beschrijven van de oppervlaktegeologie en samenstelling één van de gestelde doelen voor het CRISM instrument. Deze thesis toont aan dat de CRISM data gebruikt kan worden om regio’s met een unieke geologische samenstelling te beschrijven. Deze bevindingen komen overeen met geologische verschillen die zijn aangetoond door eerdere onderzoeken. Daarnaast heeft de data ook nieuwe inzichten verschaft door gebieden te classificeren met een mogelijk unieke geologische samenstelling die nog niet eerder geïdentificeerd zijn, zoals de gebieden rond Hellas Basin en Ophir Planum.

Nadat de toepasbaarheid van deze data voor geologisch onderzoek is aangetoond, is de data gebruikt voor het kwantitatief modelleren van de door Gamma-Ray Spectrometer (GRS) gemeten geochemische element concentraties. Vanwege de lage pixelresolutie van deze data (5*5°) is het bestuderen van deze data lastig. Door middel van kwantitatieve modellen is er een robuuste, statistische, en transparante vergelijking gemaakt tussen mineralogische informatie en de element concentraties. De resultaten hebben laten zien in hoeverre de data goed met elkaar overeenkomt en welk deel van de spectrale data het meest bijdraagt aan het statistische model. Aan de hand van deze modellen, zijn lokale veranderingen in element concentraties geologisch geïnterpreteerd gebaseerd op zowel de mineralogische- en geochemische veranderingen.

De bevindingen over de geologie van Mars zijn hier ondersteund door analyses van aardse gesteentes vergelijkbaar met die op Mars. In dit proefschrift zijn verschillende sedimentaire-, vulkanische- en omzettingsgesteenten onderzocht door middel van geochemische en spectrale analyses. Een selectie van Pilbara greenstone gesteentes, die zowel in samenstelling als ouderdom vergelijkbaar zijn met gesteentes op Mars, zijn bestudeerd om te onderzoeken of de absorptiegolflengte van chlorietmineralen bruikbaar is om hydrothermale alteratie gesteentes van metamorfe gesteentes te onderscheiden. Daarnaast is een selectie gesteentes vanuit het geowetenschap laboratorium van het ITC gebruikt voor het maken van spectrale beelden. Hiermee zijn de spectrale parameters geïdentificeerd die gebruikt worden voor Mars onderzoek. Vervolgens is bepaald hoe succesvol deze parameters zijn in beschrijven van bepaalde mineralogische samenstellingen.

Als conclusie heeft dit onderzoek, ondanks de eerder beschreven uitdagingen van de CRISM data, de potentie en toepasbaarheid van deze data voor geologisch onderzoek aangetoond. De oppervlakte classificatie heeft nieuwe informatie verschaft over bekende geologische eenheden maar heeft daarnaast ook eenheden beschreven die nog niet eerder als zodanig zijn gedefinieerd. Door het modelleren van de geochemische concentraties is de relatie tussen de geochemische- en mineralogische data gekwantificeerd. De significantie van de spectrale parameters op het model is gebruikt om lokaal de geologie te interpreteren met zowel geochemische en mineralogische informatie, wat nieuwe inzichten heeft verschaft in de geologische geschiedenis. De spectrale metingen van gesteentes analoog aan die van Mars hebben hun nut aangetoond. Door veelgebruikte spectrale parameters te evalueren is aangetoond in welke mate ze de mineralogische samenstelling voorspellen en worden mogelijke alternatieve interpretaties geïdentificeerd. Ook na dit onderzoek blijven nog veel vragen over de geologie van Mars onbeantwoord, maar het werk beschreven in dit proefschrift heeft bijgedragen aan de huidige kennis over de geologie van Mars en het belang aangetoond van het toepassen van onconventionele methodes.

Acknowledgment

This thesis in front of you presents the result of four years of rock and image analysis. I could never have completed this research without the support of the many people around me. These are not just those who have been involved directly in the research process, but also those who have asked me the most difficult questions: What are you doing the whole day, and wherefore? Did you already find water (or beer) on Mars?

First of all, I want to express my gratitude to my supervisors, Rob Hewson, Frank van Ruitenbeek and Freek van der Meer. It was my pleasure to explore the red planet together. Although Mars has never been the core business of either of you, your guidance has helped me a lot to complete this Ph.D. By giving me the freedom in defining the research approach, you gave me the confidence to develop myself as a scientist. I have always felt your support and appreciated our informal way of working together. Our meetings often started with either an update on Rob's garden, evaluations of the posters in Freek's office, or Frank's desire for coffee, and I almost felt sorry to interrupt with an update of my latest results and starting a discussion on the dust on Mars.

During my internships and travels abroad I have been fortunate to meet wonderful people in the small research field of planetary science. I want to thank all of you for your help and feedback on my work, or the fun reunions at conferences. The enthusiasm of each of you for the work you do was inspiring. I first want to mention Marloes Offringa and Bernard Foing, who introduced me to the research field of planetary science, a direction I have never considered as a possibility for myself before. I want to thank Don Hood and Suniti Karunatillake for your help in improving the GRS modeling work. But also thank you for your hospitality at LSU and showing me the culture in the Mississippi delta. A special thanks to Christina Viviano for your valuable feedback on my CRISM work. I want to thank the people of the 2016 LPI summer exploration team who I have met just before this Ph.D. We have created valuable moments, and I enjoyed the time spent with you, even the moments when I was the one who was made fun of.

These corona times have made me realize the importance of colleagues in your social life. At ITC I found an environment with many unique people with different cultural backgrounds. I very much appreciate the great memories we have made. These include all the coffee breaks with ’racist’ jokes, the cooking parties where everyone was making fun of my food, and the beers we drank in the city center.

In every step of my life and career, I have been lucky to meet wonderful friends. I fooled myself to believe that the fun you made about my research could be considered as support. Moving to Enschede, what felt like emigrating for some of you, did not stop us from spending good times. I cherish these moments of holidays, doing sports, hanging out at home or in a bar, and even playing ‘FIFA bij Kevin’. These moments to relax have been very valuable to me. I hope I can soon organize a party to celebrate this promotion with all of you.

The last sentences I want to dedicate to my family. Sometimes these special moments are necessary to remind you how lucky you are. I could not have done this without your endless support. Mom, dad, and Judith, I am very lucky to have you as my family. A special mention to my grandparents, and my grandfather Piet Struik in particular. ‘Opa’, I can easily say without your passion for rocks and geology I would not have been defending a geology thesis today.

List of Figures

List of Tables

Contents

Introduction

1

These days, most Mars geological remote sensing studies focus on site-specific, high-resolution studies, or as phrased by Ehlmann et al.: ”think local, not global” [31]. On the other hand, there are many geological processes not well understood that affected the geology on a global scale. Therefore global studies remain important to provide the global context of Mars research.

The studies performed in this thesis are driven with the motivation that new insights on the global Martian geology can come from either new datasets or new analytical approaches on the established datasets. At the moment, the CRISM (Compact Reconnaissance Imaging Spectrometer [74]) multispectral mapping mode data is an underused datasets for global remote sensing studies. The title ”Mars in multi-dimensions - a global geological survey” refers to the global aspect of this study and the multi-variate (i.e. multi-dimensions) data-analysis approach used for the remote sensing studies. Multi-dimension also refers to the different perspectives provided by the various orbital instruments of which the data is used in this thesis. With exploratory data-analysis techniques the application of the CRISM data for geological remote sensing is studied.

1.1 Problem statement

The difficulty with any planetary remote sensing studies is the lack of in-situ validation information. For Mars, the various landers and rovers have been providing valuable geological information but on a global scale, their surface coverage is negligible. Therefore, it is difficult to use in-situ data to verify remote sensing analysis. The lack of opportunity for validation leads to uncertainty in the geological conclusions drawn from remote sensing studies.

Data integration between orbital instruments is a way to deal with this uncertainty and could strengthen the geological interpretation. However, differences in surface coverage and spatial resolution make it difficult to make such a comparison. This problem is most apparent for the data integration of the OMEGA (Observatoire pour la Minéralogie, l'Eau, les Glaces et l'Activité [9]) and TES (Thermal Emission Spectrometer [21]) infrared data and geochemical GRS (Gamma-ray Spectrometer) data. Infrared imaging data often have a spatial resolution around hundreds of meters [84, 87] while the geochemical distribution is mapped with a resolution between 200-500 km [10]. For such a data integration a statistical approach is preferred above a visual qualitative comparison. The pitfall of a visual comparison is that it could lead to a confirmation bias of the results.

Most of the global geological studies using infrared data from TES and OMEGA analyze the geology based on mineral spectral modeling techniques. The results have proven to be useful and consistent [84]. The problem with spectral modeling however is that it requires prior assumptions on which minerals to model. As indicated by Morris et al. [73], within the spectral data, absorption features have been found for which no comparable Earth analog is found. These spectral variance will be not be considered when spectral modeling is applied. The alternative is studying the spectral variance itself such as the work done by Bandfield et al. [5] or Rogers et al. [85]. In this thesis studying the variance of the spectra is preferred above spectral modeling. With this approach, using the CRISM data and doing data-integration with GRS geochemical data, it is tried to provide a new perspective on Martian geology and potentially reduce the uncertainty of the geological interpretation.

1.2 Knowledge gap

In general with orbital remote sensing studies, the geological history of Mars is interpreted in consecutive steps. From the infrared spectral data the mineralogical abundance is interpreted and used to estimate the lithology. Based on the lithology, geological processes are hypothesized. The level of uncertainty increases each interpretation step. For example regarding the interpreted variance of mafic minerals that was found to be similar observed by TES and OMEGA observations [84]. But whether the lower content in the northern lowlands is related to a difference in volcanic composition [5], or weathering in aqueous conditions [112, 61] remains a topic of debate.

New orbital data could provide a new perspective on the Martian geology previously proposed geological interpretations. In that sense, for an exploratory research field as Martian remote sensing, just the fact that there is an almost unused dataset can be considered as a knowledge gap itself. The CRISM instrument measures in the visible and short-wave infrared wavelength range and is, therefore, suitable to detect both primary volcanic minerals and secondary alteration

minerals. Therefore this instrument has the potential of giving a new perspective on the global mineral distribution in comparison with those of TES [87] and OMEGA [84]. In addition, the similarity in measured wavelength range as the OMEGA instrument could make it a useful dataset to verify the mineralogical interpretation or presence of absorption features detected by both instruments.
The earlier described difficulties with the GRS geochemical element maps contribute to the number of geological theories to explain the spatial distribution of each element [10]. Several data-integration attempts are performed using different infrared orbital instruments, such as TES [87], OMEGA [84], and CRISM [105], but although they might explain locally the variation of element concentration the global variation remains uncertain. Also, new modeling attempts resulted in new global element maps for Al, Ca, and S which are made available [46] for this study. These maps are interpreted here globally for the first time.

1.3 Objectives

As described before the novelty of the studies described within this thesis are characterized by (1) the use of an underused dataset (2) and the applied methodology. Together this is combined as the main research question *What can the CRISM mapping data in combination with novel application of methods, including multivariate statistical and exploratory spectral analysis and geochemical data integration, contribute to the current knowledge on the geology of Mars?* Based on this question several objectives and sub-questions are formulated that together form the structure of the thesis.

Objectives

1. To test the applicability of CRISM mapping-mode data for characterizing global surface mineralogy surface-type classification
2. To explain the relationships between the geochemical and spectral datasets and how they can complement each other in the interpretations of regions on Mars and of Mars analog rocks
3. To evaluate the added value of the study of Mars analog rocks as a means of verification of the results of Mars remote sensing studies

Corresponding research questions

I What can global CRISM summary product maps contribute to the current understanding of the Martian geology?

II What can infrared spectra say about the geological formation of greenstone rocks from Western Australia, and what are the implications for Mars?

III How do the CRISM summary products respond to the composition of Mars analog rocks?

IV How do global CRISM mapping data and gamma-ray spectrometry geochemistry data correlate, and what does the correlation tell about the effects of geological processes on the mineralogical and element distributions in the Martian surface?

1.4 Datasets

The work in the thesis is based on the processing and analysis of spectral mineralogical and geochemical data sets. These datasets originate from laboratory instruments used for the Mars analog studies and satellite instruments for remote sensing studies. In the next sections, the measuring techniques and specifics of the instruments of which the data is used in this thesis are introduced.

1.4.1 Mars remote sensing

The geochemical and mineralogical interpretations of Mars is done based on two different instruments carried on two different satellites. The global surface mineralogy is interpreted based on the interpretation of spectral features within the data of the CRISM instrument carried on the Mars Reconnaissance Orbiter (in orbit since 2006) [74]. The geochemical element distribution comes from modeling gamma-ray energy measured by the Gamma-Ray Spectrometer on the Mars Global Surveyor (1997-2006) [10].
Besides the modes of measuring, also the spatial resolution and measuring depth of both instruments are completely different. The CRISM instrument measures the visible- (VIS) (0.4 - 0.7 μm) and near-infrared wavelength ranges (NIR) (0.7-3.93 μm) [74]. In push-broom multispectral imaging mode it scans the surface with a spatial resolution of 200 m/pix in 73 wavelengths[74]. The gamma-ray spectrometer measures all gamma-ray energies in contact with the instrument without context from what part of the planet the energy comes from. So the gamma-ray energy can come from anywhere within the visual edges of the planet, and to derive global element concentrations maps, the gamma-ray energy data needs to be modeled within a 5^o*5^o grid, which equals a resolution of 200-500 km depending on the latitude [10]. Different from infrared spectroscopy the gamma-ray can detect from up to approximately 1 m depth. As a consequence, the element maps do not resemble the concentration of the surface but the subsurface. [10]

1.4.2 Laboratory datasets

Multiple different instruments have been used for laboratory studies. Details on the instruments and modes of measuring are provided in the Chapters 3 and 4. Infrared spectroscopy studies are performed both with imaging spectroscopy (SPECIM instrument [95]) as single spectrum measurements (ASD instrument [80]). Geochemical element concentrations are measured of single minerals with an electron microprobe and of bulk rocks with x-ray fluorescence.

1.5 Analytical approach

Most research presented here is characterized by either the use of applying novel analysis techniques or applying common techniques to a new dataset. The details of each method will be discussed in each chapter individually but the studies have a data exploratory approach in common. This means that the geology is interpreted from the variance found in the data, rather than finding evidence in the data to support a geological theory.

The Mars remote sensing studies are both done with unsupervised and multi-variate data analysis techniques. It is hypothesized that such an approach contributes to an unbiased perspective on a dataset, or relations between datasets.

The laboratory studies are done as an attempt to verify the findings based on Martian remote sensing data. The limited spatial coverage of landers and rovers on Mars results in the lack of in-situ validation measurements. The hypotheses of geological processes on Mars and the response of data can be tested on terrestrial rocks similar to those found on Mars.

1.5.1 Analysis techniques CRISM

As mentioned before in the Objectives section 1.3, the CRISM instrument plays a key role in most of the studies in this thesis. The instrument has three types of observations: a targeted mode, a multispectral mapping mode, and an atmospheric mode [74]. The data of the multispectral mode has a close to global coverage but the data is hardly used for global geological studies.

The data is studied with so-called summary products. These are spectral parameters developed in particular to explain the spectral variance in the CRISM dataset [82, 106]. Most of the summary products are developed to describe spectral features that indicate specific mineralogy. The description of the summary products and their formulas are summarized in a Table attached in Appendix 6.4. The continuous data values of these products are thought to be in particular useful for the statistical data exploration approach.

1.6 Organization thesis

The earlier defined objectives form the structure of the chapters. The general variance of the CRISM mapping mode data and the applicability of summary products for global surface type analysis is addressed in Chapter 2. These summary products are evaluated in Chapter 3 by calculating the same summary products on spectral images of Mars analog rocks. This way the interpretations of the summary products can be compared with what was observed on Mars (Chapter 2) and in the lab 3. In Chapter 4 Mars analog rocks from the Pilbara Craton are studied for spectral variances between phyllosilicate minerals, especially chlorite, formed in hydrothermal and metamorphic conditions, and how this relates to rock geochemistry. In a more detailed scale Chapter 5 describes the modeling attempts of the global geochemical variance in relation to the mineralogical information from CRISM.

2

Mars Global Surface Classification [*]

2.1 Introduction

To make the most accurate reconstruction of the global surface composition and geological history of Mars, information is required from all available orbital instruments. So far, the global mapping data of CRISM (Compact Reconnaissance Imaging Spectrometer) has rarely been used for global surface analysis. Shallow absorption features in reflectance spectra and differences between orbital observations complicate the use of this dataset. Nevertheless, it is thought that this dataset can provide important information to understand Mars' global geology.

Most global surface composition studies that use infrared spectroscopy, are performed with the TES (Thermal Emission Spectrometer) [5, 85] and OMEGA (Observatoire pour la Minéralogie, l'Eau, les Glaces et l'Activité) instruments [8, 77, 84]. Based on the analysis with both instruments, the general composition of Mars is estimated to be of basaltic to andesitic composition, with pyroxene, olivine, and feldspar as primary minerals [69, 31]. Additional geological processes contributed to the presence of secondary minerals such as clays, sulfates, ferric-oxides, and carbonates [19, 31]. The mineralogical composition is directly related to the climatic and geologic conditions during their formation, and is therefore of importance to reconstruct the geological history.

The CRISM spectra are analyzed by using so-called summary products, which help to infer the presence of differing minerals by identifying important spectral features in the wavelength range between 0.4 – 4 μm. These products have been developed for the CRISM data by Pelkey et al. [82] and later revised by Viviano-Beck et al. [106]. Spectral features include band depths, spectral peaks, spectral band indices and ratios, spectral slope, and reflection

---

[*] This chapter is based on: Kamps, O. M., Hewson, R. D., van Ruitenbeek, F. J. A., van der Meer, F. D. (2020). Defining surface types of Mars using global CRISM summary product maps. Journal of Geophysical Research: Planets, 125, e2019JE006337

values related to the compositions' absorption spectral features (see Table S.1.1. supplementary information in Kamps et al. [55]). Each of the products can be interpreted for specific mineralogy or surface property, although some have caveats for atmospheric conditions. Earlier studies showed that these products could highlight the presence of both the primary and secondary minerals [82, 106].
The Pelkey products have been previously calculated and analyzed from the global mapping CRISM data [82]. The later Viviano-Beck products, however, are often used for the targeted CRISM observations. Because of the earlier described complications, the applicability of these later products for the multispectral reduced data record (MRDR) dataset is published here for the first time. A visual and statistical comparison is done between the products of Viviano-Beck et al. [106] and those of Pelkey et al. [82], and other global mineral maps based on the data of the OMEGA and TES instruments. The radiometric differences between orbital observations are addressed here by averaging the used summary products for a grid of circa 5^o*5^o, where each grid tile is the size of the mosaic tile of the MRDR dataset. Another advantage of using the resampled grid data is that the resolution provides a good balance between spatial coverage and spatial resolution on a global scale.
An unsupervised clustering analysis will give an overview of the variability in the dataset. The surface composition of these clusters, and the potential geologic processes that formed them will be interpreted. The summary products are studied for correlations and anti-correlations between each other and between external datasets such as the digital elevation of the Mars Orbiter Laser Altimeter (MOLA), and the dust coverage index of the Thermal Emission Spectrometer (TES) instrument. By studying the individual summary product maps in combination with the correlation coefficients the global distribution of the summary product values is interpreted to understand their potential influence from mineralogy, and also from possible other factors such as dust coverage and atmospheric thickness. The combination of the detectable minerals and the almost complete global coverage of the dataset [90] makes the CRISM MRDR dataset valuable for global surface classification. Using the global dataset as input for this clustering analysis approach ensures that most diverse range of possible geological land covers are included.

2.2 Method and Data

The methodology of this study includes several successive analyses: testing for correlations between the summary products, surface type classification and finding the relationships between the surface types and summary products. These analyses are summarized in the flowchart in Figure 2.1. In the following section the CRISM multispectral dataset is introduced (Section 2.2.1), followed by what data-preparation has been done prior to the statistical analysis (Section 2.2.2), with the statistical analysis described in the last section (Section 2.2.3).

2.2.1 CRISM multispectral dataset

The CRISM instrument is an imaging spectrometer on the Mars Reconnaissance Orbiter, which operates in the visible-/ near-infrared wavelength range from 0.36 – 3.93 μm. The instrument has three types of observation modes: a targeted mode, a multispectral mapping mode, and an atmospheric mode [74]. The mapping mode, which is used for this study, corresponds to 73 wavelength channels with a spatial resolution of 200 m/pix. Out of these 73 channels, 55 were measured by the infrared detector and 18 measured by the visible-/ near-infrared detector, which both work in parallel. The dataset with these strips is also referred to as the Multispectral Reduced Data Record (i.e. MRDR). The latest estimation of global coverage is 87 %, and circa 80 % coverage around the equator, with 45 % coverage having repeated sampling [Seelos Murchie, 2018]. MRDR includes image data of I/F (radiance/ irradiance), reflectance, Lambertian albedo, summary products, and derived data records information, such as incidence, emission, phase angle, and surface temperature [74]. The MRDR data were made available on the planetary data system (PDS) of NASA, as individual strips and as mosaic tiles of 5^o*5^oo. The analyses in this study are all performed on the mosaic tiles. Both the Pelkey summary product mosaic tiles and albedo mosaic tiles used for our analyses are PDS version 3 from 2009.

Although the MRDR mosaic tiles are available for all latitudes, only the CRISM tiles between 67.5^o degrees North and South latitudes were used in this study. It is expected that this coverage is less affected by seasonal changes of ices in the polar regions and therefore we try to minimize the ice contribution to the CRISM spectra [93].

Spectral features in the CRISM wavelength range were described by spectral parameters, which are also called summary products (Table S.1.1. in the supplementary material in Kamps et al. [55]). These products are developed by Pelkey et al. [82] and Viviano-Beck et al. [106], and are both used in this study. Hereafter often referred as the Pelkey, and Viviano-Beck dataset, respectively. The summary products of Pelkey et al. [82] are downloaded as mosaic tiles from the PDS. For the products of Viviano-Beck et al. [106], the products are calculated using the IDL programming script from the CRISM processing toolbox, CAT ENVI. These summary products are calculated from the CRISM MRDR mosaic tile albedo dataset, measured in the mapping mode of the CRISM instrument. The supplied albedo data is already corrected for the atmospheric and photometric effect, and shared as similar mosaic tiles for the Pelkey summary products dataset [74]. The Pelkey dataset has a total of 44 summary products, of which 34 products are calculated from the Lambert albedo dataset which are designed to relate with a mineralogy or surface composition [82]. Viviano-Beck et al. [106] revised some of these products and included new products, totally up to 60 products, of which 49 are developed for mineralogy or surface composition purposes. The parameters of Pelkey et al. [82] were developed and tested in particular for the MRDR dataset. The products of Viviano-Beck et al. [106], however, are commonly used for the targeted measuring mode of CRISM, but are designed such that they are also suitable to calculate for the MRDR data. However, the global maps for all of these products are assessed here for the first time.

The spectral features described with these products are one of the following four types: (1) reflectance at a specific wavelength, (2) spectral slope which is a linear slope defined by the reflectance different between two bands divided by the wavelength difference between two bands, (3) band depth, defined as the reflectance corresponding to the position of the minimum of the band divided by the reflectance calculated as a linear continuum fit between two reflectance wavelengths on each side of the band, (4) and indices derived using the ratio of reflectance values from different wavelengths. The summary products are designed so that a higher value represents a more prominent appearance of the spectral feature. For details and formulas of the used summary products, the reader is referred to the Appendix Table 1 attached as supplementary material or the papers of Pelkey et al. [82] and Viviano-Beck et al. [106].

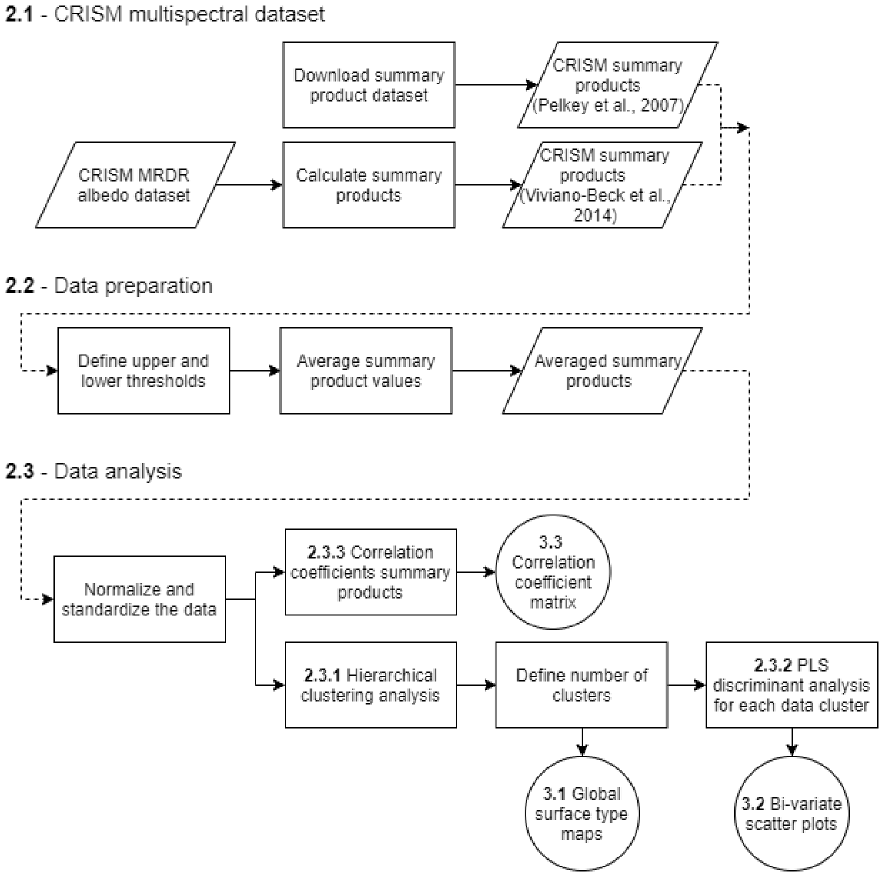

Figure 2.1 Flowchart of the methods presented in this study. Numbers above boxes indicate the section where the methodology is described in detail. Parallelograms indicate datasets, rectangle processes, and circles results.

2.2.2 Data preparation

The Pelkey and Viviano-Beck summary products come with some challenges that are addressed below. One of the problems is that for some summary products, the MRDR data products show inconsistencies between overlapping or adjacent orbital strips. These radiometric residuals between the strips in the mosaic are a result of the atmospheric and photometric corrections done for the MRDR data strips before the mosaic is made [90]. A second problem is that some pixels contain extreme values which are more likely to be artifacts in the data rather than spectral features.

To overcome the problems with unrealistic values, lower and upper thresholds are defined based on the global mosaic data. Values that are lower or higher than these thresholds are masked and discarded from the analysis. These thresholds are defined based on quartile distances, also known as Tukey's fences [100]. Quartiles, or percentiles, of the data defines the percentage of lower data values. Quartile 1 (Q1) refers to the 25th percentile, which means that 25%of the data has lower values than Q1. The median refers to Q2, or 50th percentile, and Q3 to the 75th percentile. The difference between Q3 and Q1 is defined as the inter-quartile distance (IQD). Tukey's fences indicates that lower outliers can be defined by 1.5 times IQD, minus the Q1. The upper threshold is defined by values 1.5 times the IQD, plus Q3. For the band depth defined products, the minimum threshold value is set to zero, meaning that all negative band depths are excluded. A negative band depth refers to an absent spectral absorption feature and therefore indicates mineral's absence. The resulting global summary product maps can be found as supplementary material (Data Set S 1 supplementary information in Kamps et al. [55]) and can be found in unannotated format in Kamps 2019 [54], the maps for HCPINDEX and BD2250 are shown as two examples in Figure 2.2. The global maps of both summary products are presented at the original MRDR resolution (top figures) and the averaged 5^o*5^o pixel size resolution (bottom figures). Underneath each global map also the upper and lower thresholds are indicated, and all pixels that are not considered for the averaging are masked out in the original resolution maps.

After masking all pixels outside the defined thresholds, we averaged the values for each individual summary product within a grid cell. The grid cells coincide for the size of a CRISM mosaic tile (5^o*5^o/pix). For several reasons, such as the lack of pixel values within the defined thresholds or the atmospheric effect on some of the summary products, several products were discarded. In particular, from the Pelkey dataset the products VAR, BD1750 and BD2100 were excluded from the analysis because the data include too little number of pixels with band depths larger than zero. In the averaged dataset this resulted in a lack of spatially coherent patterns which was found unlikely to represent a mineralogy. For the same reason, summary product BD8602 was excluded from the Viviano-Beck dataset. The summary products BD25002 and MIN22952480 from the Viviano-Beck dataset were excluded because all values were negative. The discarded products are categorized separately in Table S 1.1 (supplementary information in Kamps et al. [55]). in the supplementary materials and are not used in either of the analysis.

After averaging several products appear to have no-data values for some pixels. These are the products related to reflectance values >3 μm in the vicinity of Hellas Basin (BD3000, BD3100, BD3200, BD3400, CINDEX). In the Pelkey dataset also some pixels of the product BD860 have no data values for several pixels in the dust-covered regions. Because all products with no-data values are band depth products, the pixel values are set to zero which can be considered as no spectral feature.

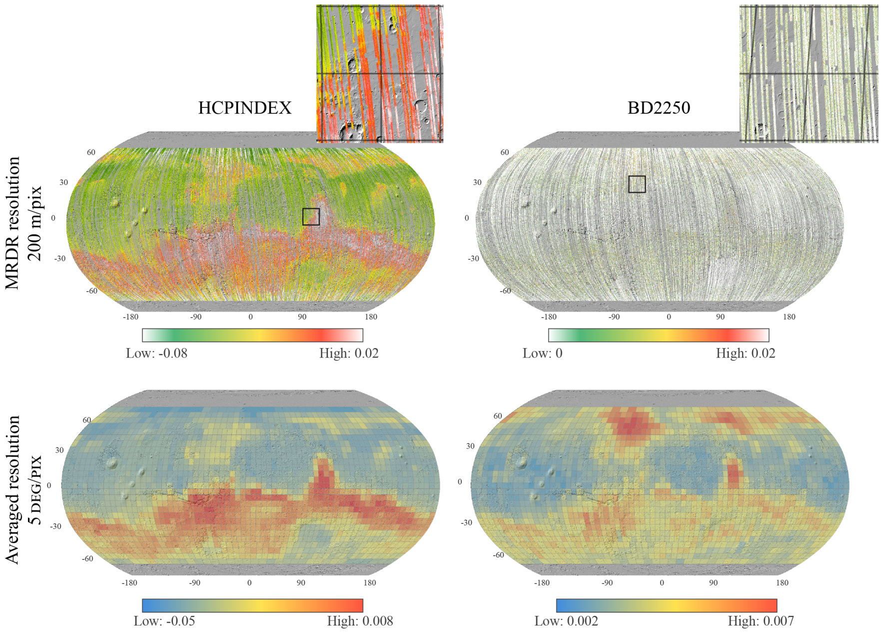

Figure 2.2 Global maps of the summary products HCPINDEX and BD2250, at original MRDR resolution (200 177 m/pix) and averaged resolution (5o/pix). At the original resolution the white pixels are those considered as outliers (Section 2.2.2)

2.2.3 Data analysis

A combination of multivariate data analysis techniques are used to define the surface types and find the products that contributed significantly to defining these surface types. Prior to the statistical analysis, the values for each product are normalized and standardized, which means that for each summary product, the average is subtracted from each observation and divided by the standard deviation.

In the statistical analysis, both the variables (summary products) and samples (pixels) are studied. The summary products are studied to understand their relationship with the mineralogical composition. This is done by testing how the summary products are correlated to each other, and to other variables such as elevation and the dust cover index from the TES-instrument (resolution 16 pixels per degree) [Ruff Christensen, 2002]. The spatial patterns in the global summary product maps are compared with mineral maps based on studies with the CRISM, TES and OMEGA instruments [23, 88, 4, 8, 85, 59, 77, 84].

2.2.3.1 Correlations between summary product

The relationships between the different summary products are studied by calculating the Pearson's correlation coefficients (r), described in Section 3.1 [51]. The dust cover index [88], and MOLA (Mars Orbiter Laser Altimeter) digital elevation [114], are also averaged for the size of a CRISM mosaic tile and included in the correlation analysis. In particular, the Pearson's correlation coefficient calculated between summary products and digital elevation enable the effect of dust and atmosphere on the summary product values to be studied [114].

The correlation coefficient is an indicator of the influence of one variable on the other, and is often used as an effect size. A Pearson's correlation coefficient ranges between -1 and 1, where -1 means an absolute negative correlation, 1 a positive correlation and 0 no correlation at all [25, 26]. Categorizing the effect size in low, moderate and high effect is arbitrary. Here it is classified into the following categories: $-0.6 < r$ or $r < 0.6$ indicating low correlation, $0.6 < r < 0.8$ or $-0.6 > r > -0.8$ for moderate correlation, and $-0.8 > r$ or $r > 0.8$ for high correlation. These thresholds are used in Figure 2.3 to indicate any effects between summary products, between summary products and dust coverage, and between summary products and elevation/atmosphere. As described in Section 2.2 the conservative lower correlation coefficient of 0.6 is used to allow for excluding summary products with possible atmosphere effects.

2.2.3.2 Defining surface types by clustering analysis

To classify the data, we use hierarchical clustering analysis, which is an unsupervised clustering method [51]. Here, hierarchical clustering analysis is favored above other cluster analysis strategies such as k-means, because hierarchical clustering does not require a prior assumption about the number of clusters. Instead, by using a tree-diagram, also known as a dendrogram, the relationship between clusters can be studied. The surface types are studied with a divisive (top-down) approach. With this approach, the clustering analysis is used to find clusters in the data being the most dissimilar, so those with the most unique surface composition [43]. Pixels are clustered by calculating the unweighted averages of the Euclidean distances (Results Section 3.2). Although hierarchical clustering analysis does not require a prior assumption about the number of clusters, it is of interest to this study to know how many clusters describe the variability in the dataset best. At some point defining more clusters would not indicate major variability in the data but smaller changes within clusters instead. The decision on the number of clusters is based on the knowledge of the data and the geology. As described by Hardy [40] the validity of the number of clusters was tested with the elbow method of a graph plotting the mean Euclidean distance against the number of clusters (Results Section 3.2). The elbow method assumes that significant clusters have a high Euclidean distance. At some point, adding new clusters would cause a decrease in slope because these new clusters are explaining minor spectral differences within a cluster instead of significant new clusters [40].

2.2.3.3 Relationships between surface types and summary products by PLS-DA

Summary products can be used to draw conclusions about the mineralogy and related surface types. Because the clustering was performed with multiple summary products, a multi-variate analysis is preferred above comparing each individual map, to define the importance of each summary product on the definition of each surface type.
A common method to reduce the number of axes in the dataset is principal component analysis (PCA) which defines new axes in the dataset that describe the most variance [51]. Since we are interested in the variance between each cluster and the rest of the data, and not in the variance within the complete dataset, we used Partial Least-Squares Discriminant Analysis (PLS-DA) (see Section 3.2). This is a method that originates from the field of chemometrics [15]. Just like PCA, it creates new axes in the dataset, where the first axes in PLS-DA describe most of the variance between groups. In our study the PLS-DA is done for each cluster defined by the hierarchical clustering analysis. All pixels of the cluster we study for that specific PLS-DA are considered as one group and all other pixels as another group. The two groups are used as input for the PLS-DA to create a new axes that describes the most variance between these groups. The outcome of the PLS-DA are components with weight values for all the variables, and score values which are pixel values projected on the new component axis. These can be analyzed as a bi-variate plot, which is a scatter plot presenting both of these results in one figure. Based on this figure it can be observed which variables, i.e. summary products, relate to which surface type (Result Section 3.2).

2.3 Results

2.3.1 Correlation between summary products

Figure 2.3 shows a correlation coefficient matrix of all summary products and the two additional variables, elevation and dust coverage. The brighter the color the higher the positive (green) or negative (red) correlation coefficient. The boxes highlight the correlation coefficient larger than 0.8 and the circles those larger than 0.6. The summary products are grouped into 6 categories based on our interpretation and the descriptions of Pelkey et al. [82] and

Viviano-Beck et al. [106]. Those products describing a mineralogy are categorized in mafic minerals, i.e., olivine and pyroxene, ferric iron, and secondary minerals. We used the term secondary minerals to summarize the mineral groups of carbonates, sulfates, phyllosilicates, and hydrous silicates. These mineral groups have overlapping spectral features in the wavelength range between 2-2.5 μm, which makes it difficult to distinguish them from each other based on an individual spectral parameter. Besides mineralogical summary products, some are interpreted to be related to the dust coverage, the atmosphere conditions, and ices. The atmospheric effect on the summary products is tested by determining their Pearson's correlation coefficients (r) with the digital elevation (see Section 2.3.1). For the products with a moderate correlation coefficient ($r < -0.6$ or $r > 0.6$) with the digital elevation, the spectral features are considered to be significantly affected by atmospheric absorption, and thereby biasing the values of the summary products, assuming that the atmospheric effects are linearly related with elevation. From the Pelkey dataset these are the products ICER2 and BDCARB, and from the Viviano-Beck dataset BD1400, BD1435, BD1900R2, BD2200, BD2355, ICER2 and BD3000. The reason of this relation between these products and the elevation can be that the products are sensitive for the spectral features of atmospheric CO2 near 1.4, 1.9 and 2 μm [68, 16].

Because of the atmospheric effect on these summary products these are excluded for the clustering and PLS-DA analysis. Therefore for the following analysis both the products categorized as discarded and atmospheric in Appendix Table 1 in the supplementary materials are not considered.

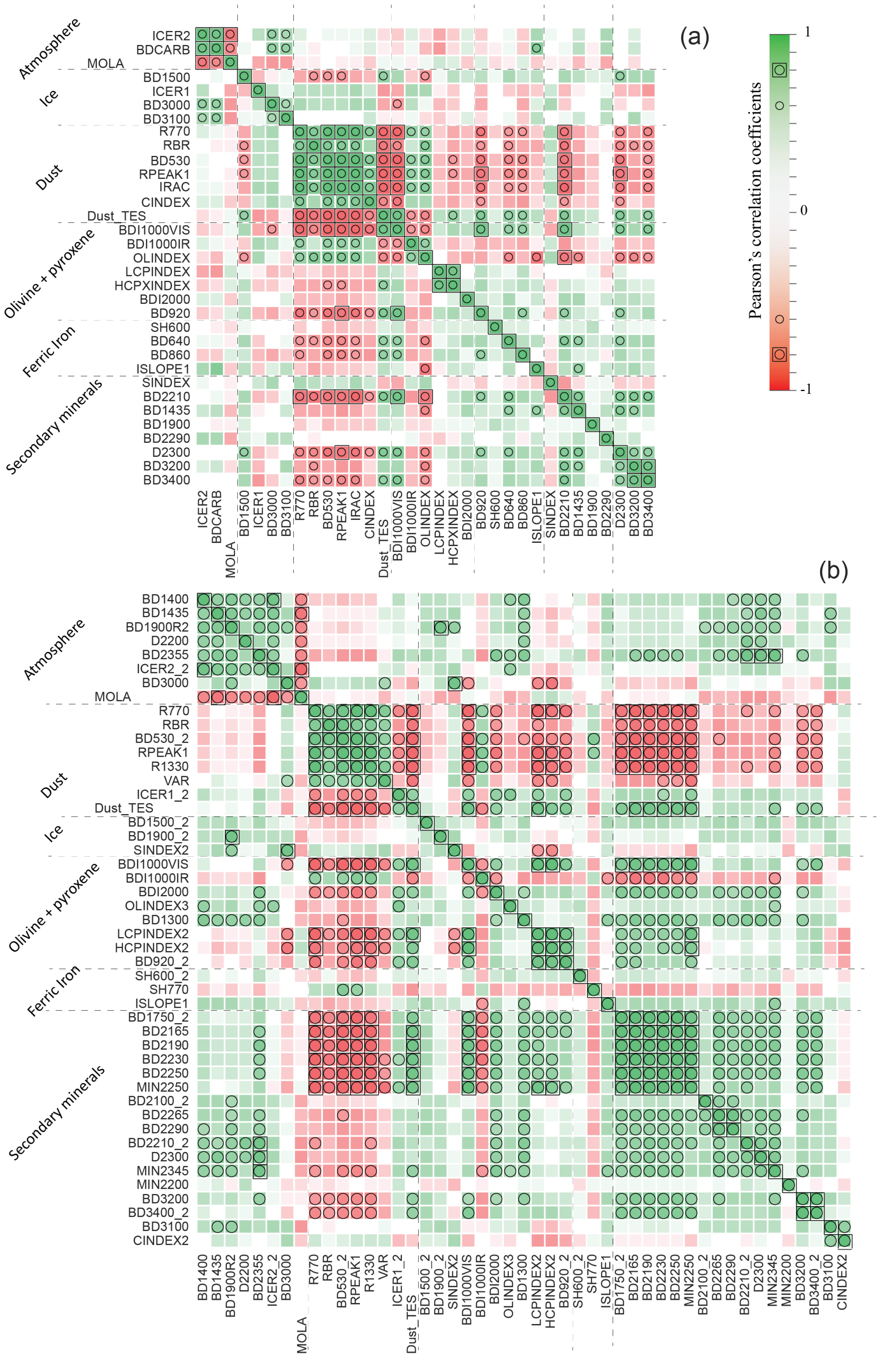

Figure 2.3 Correlation coefficient matrices of summary products of the Pelkey (a) and Viviano-Beck (b) data sets. The brightness of the color shows the positive (green) and negative (red) Pearson's correlation values. The circle highlight the correlation values with moderate correlation (-0.6 > r or r > 0.6) and squares + circles those with high correlation (-0.8 > r or r > 0.8), see the color bar in the upper right of the figure.

2.3.2 Classification into surface types

The results of the clustering analysis are presented as global maps and are shown in Figure 2.4 with the corresponding dendrograms in Figure 2.5. The clustering analysis based on the Pelkey and Viviano-Beck datasets show many similarities. In both analyses the main branches in the dendrograms relate to the following surface types: northern lowlands, southern highlands, Hellas Basin, dust covered regions, and Syrtis Major and Meridiani. A total of 18 clusters have been defined by the summary products of Pelkey, and a total of 17 clusters by those of Viviano-Beck. The names of the clusters in Figure 2.4 will be used the remainder of this paper. The results of the elbow method are attached as supplementary material. In the elbow plot (Figure S 2.1 supplementary information in Kamps et al. [55]) it shows that the number of clusters chosen are around the tipping point (elbow) where the change in Euclidean distance is constant. As mentioned in the Methods Section 2.2.3.2, this is the point where more cluster describe internal variance of cluster instead of significant new clusters.

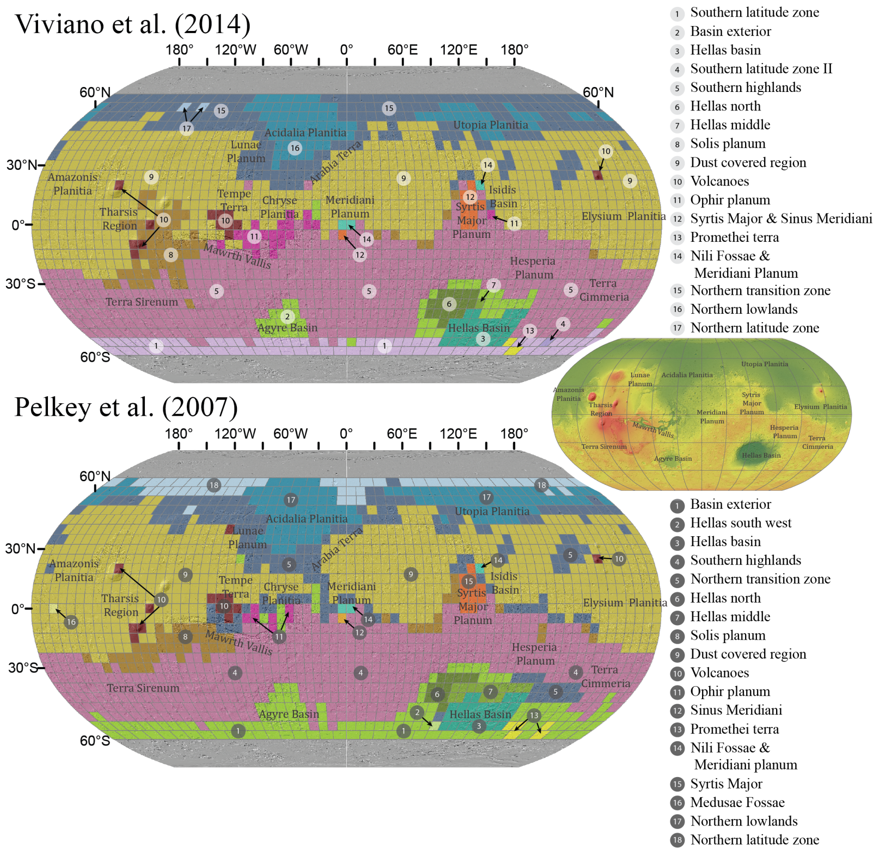

Figure 2.4 Global maps presenting the global surface types based on hierarchical clustering analysis. Upper figure is the surface type map presenting the clusters based on the summary products of Viviano-Beck et al. [106] and the lower figure is based on the products of Pelkey et al. [82]. Numbers shown are the outcome of the hierarchical clustering analysis and correspond to the dendrograms in Figure 2.5. Cluster names were generally assigned based on the geographical location of where they typically appear, except for the dust covered region.

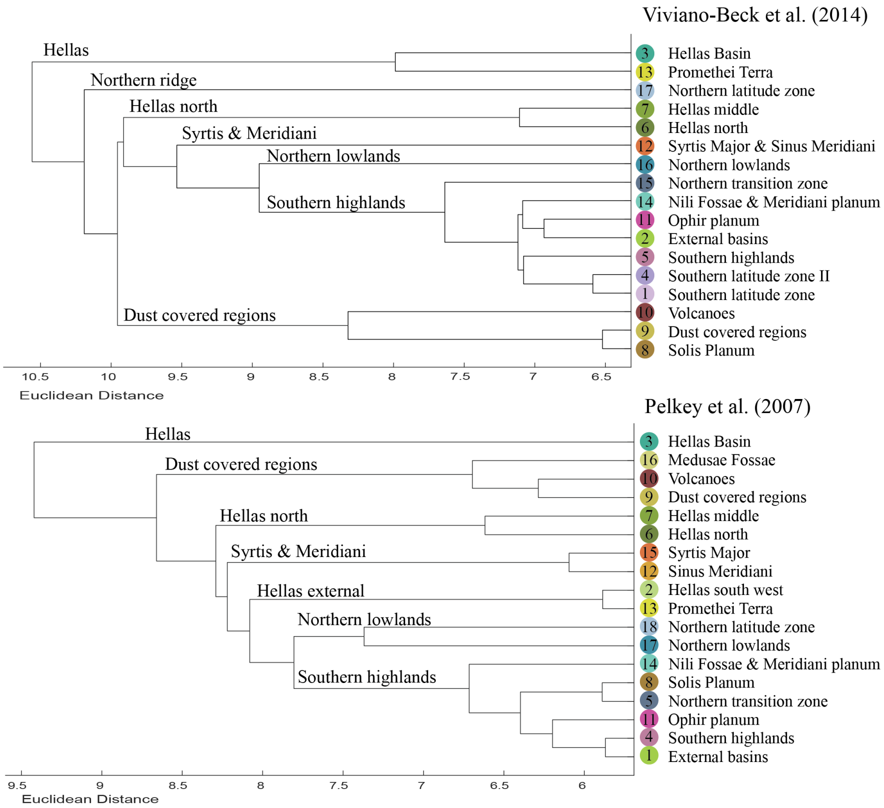

Figure 2.5 Dendrograms of the hierarchical clustering analysis. The main branches are named after the geographic regions in Figure 2.4 that are covered by the surface types.

2.3.3 Relationships of summary products and surface types

For each surface type a PLS-DA is performed to test the contribution of each summary product to the definition of that surface type. Because this involves a total of 35 individual analyses (18 surface types derived from Pelkey 2007 parameters and 17 surface types derived from Viviano-Beck 2014 parameters), four geologically interesting clusters are shown here as an example (Figure 2.6). The examples include Syrtis Major + Sinus Meridiani, Nili Fossae + Meridiani Planum, northern lowlands and the transition zone, all performed with the Viviano-Beck products. These figures present the score and weight values of the first two components of the PLS-DA. As described in the Methods Section 2.2.3 the first components explain most of the variance between the groups. The figures essentially display the same as a bi-variate plot from a principal component analysis. The score values are the pixel values on a projected axis

(PC). Weights are an indicator of how much the summary product contributed to the axis, so the higher the weight, the higher the contribution.

Table 2.1 summarizes all PLS-DA results, and can be found in plot form in the supplementary material (Figures S4.1 - S4.35 in the supplementary information of Kamps et al. [55]). This table indicates for each surface type of both the Pelkey and Viviano-Beck datasets, the summary products that contributed to their classification, based on the weight values of the PLS-DA (see Figure 2.6). The variables that plot close to the specific surface type (encircled in the bi-variate plot in Figure 2.6) have a positive contribution and those that plot opposite have a negative contribution in defining the surface type. Figure 2.6 shows that it is not always clear which summary products contributed most in defining the surface types. Therefore the global maps of the distribution of each summary products are used to evaluate the interpreted importance of the summary product for a specific surface type.

The distance between the pixels of one surface type to all other pixels in the bi-variate plots, indicates how distinct the surface type is compared to all other pixels. For example, the pixels classified as transition zone (Figure 2.6c.) plot between the dust covered pixels and either the northern lowlands pixels or southern highland pixels. Therefore, no specific summary products were listed for the transition zone in Table 2.1.

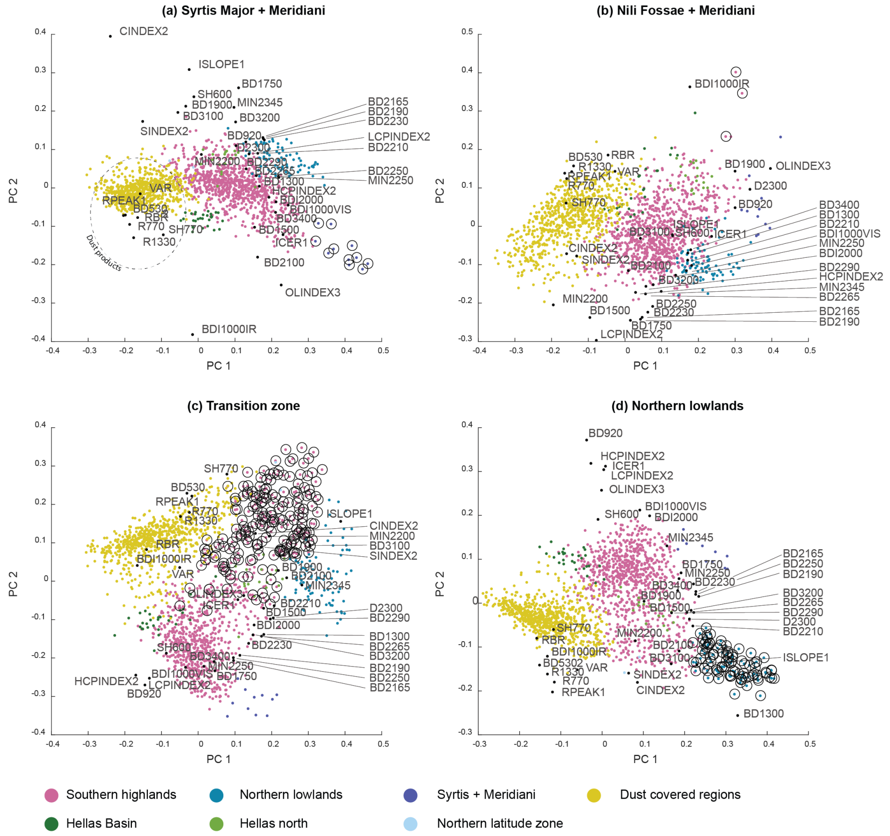

Figure 2.6 Bi-variate plots presenting the score values (colored dots: pixels) and weights (black points and labels: summary product variables) of the summary product of the principal component, resulting from the PLS discriminant analysis. These are the surface types and summary products of Viviano-Beck et al., [106]. The plots show the results for the surface types (a) Syrtis Major + Meridiani, (b) Nili Fossae + Meridiani, (c) transition zone, and (d) northern lowlands. Dots correspond to the colors used for the global maps (Figure 2.2) of the main branches shown in Figure 2.5. The circles highlight the pixels that belong to the surface type labeled with the name above each sub-plot.

Surface type		Pelkey 2007 parameters		Viviano-Beck parameters
Southern highlands	4	BDI1000VIS HCPINDEX LCPINDEX BD920 BD860	5	HCPINDEX2 LCPINDEX2 BD920_2 SINDEX2 BDI1000VIS

Syrtis Major	15	R770 RBR RPEAK1 BDI1000VIS IRA BD2210 BD3000 BD3400 BD640	12	OLINDEX3 R1330 BD1300 VAR ICER1_2 BDI2000 BD2100_2 BD2165 BD2190 BD2230 BD2250 MIN2250 CINDEX2 BD3400_2 R770 RPEAK1 RBR BD530_2 VAR
Nili Fossae + Meridiani planum	14	D2300 BDI1000IR	14	OLINDEX3 D2300 LCPINDEX2 BDI1000IR SINDEX2 BD1900
Ophir Planum	11	SINDEX RBR BD3400 ICER1 ISLOPE1	11	BD1900_2 MIN2200 ICER1_2 BD3400_2
Sinus Meridiani	12	BDI2000 D2300 SH600 BDI1000VIS		See Syrtis Major
Southern latitude zone			1	SH700 R1330 BDI1000IR R770 BD2210_2
Southern latitude zone II			4	SH700 BD2265
Promethei terra	13	CINDEX	13	CINDEX2 BD3400_2
Northern lowlands	17	LCPINDEX HCPXINDEX OLINDEX ISLOPE1 BD3200 BD3400 BD2210 D2300 BD1435 BD2290	16	BD1300 BD920_2 OLINDEX3 LCPINDEX2 HCPINDEX2 ICER1_2 ISLOPE1 BD3200 BD3400 D2300 MIN2250 BD2250 BD2230 BD2190 BD2165 BD1750_2
Transition zone	5	Composition between dust covered region and adjacent surface type	15	Composition between dust covered region and adjacent surface type

Northern latitude zone	18	D2300 BDI1000IR ISLOPE1 BD3100	17	MIN2200 BD1500_2 HCPINDEX_2 LCPINDEX_2 SH600_2
Equatorial region	9	R770 RBR BD530 RPEAK1 IRAC CINDEX OLINDEX BDI1000IR BDI1000VIS ICER1 BD1500 SINDEX	9	R1330 R770 BD530_2 RPEAK1 RBR SH770 BDI1000IR VAR
Volcanoes	10	BD3100 BD3200	10	MIN2200 CINDEX2 BD3400_2 BD3200 BD1500_2 BD2210_2 ICER1_2
Solis Planum	8	ISLOPE 1 BD2290 BDI2000	8	ISLOPE1 BD1900_2 BD2210_2 OLINDEX3
Medusae Fossae	16	BD1900		
Hellas Basin	3	BD3100 CINDEX BD3200 BD3400	3	BD3100 CINDEX2 BD3200 BD3400
Hellas north	6	SINDEX ICER1 BD2210 SH600 BD1435	6	VAR SINDEX2 SH600_2 OLINDEX3 D2300 RBR SH700 MIN2250
Hellas middle	7	BD3200 SH600 BD3400	7	VAR BD3100
Hellas external	1	BD3000 SINDEX BD3400 BD640 BD1500 BD1900	2	SH600_2 RBR SH700
Hellas south west	2	CINDEX		

Table 2.1 Summary of the most important products of Pelkey and Viviano-Beck for each surface unit (“ST”). Products with negative contribution are underlined. Numbers in the column Surface type correspond to those in Figure 2.2 and Figure 2.5

2.4 Discussion

The results show that the CRISM multispectral mapping mode data are useful to assess the global surface geology. The novel approach with the use of summary products in combination with unsupervised data-analysis techniques has proved to be a transparent method to test for the variability in the CRISM data and evaluate for the local geology. The PLS-DA allows us to study the variance of each surface type in multi-dimensions as shown in Figure 2.6, and summarized in Table 2.1. Some are defined based on distinct geological phenomena, and others are related to non-geological processes or to artifacts in the datasets. The method shows to be consistent in that it exhibits similar surface types for the Pelkey and Viviano-Beck datasets and correspond to surface type classification studies based on TES [5, 85, 87], OMEGA [84] and GRS [36].

The spectral differences between the southern highlands and northern lowlands (Figure 2.4) is the most consistent in all global surface types studies. Just as it was observed by the TES and OMEGA instruments, the northern lowlands have limited spectral features related to the mafic minerals olivine and pyroxene in comparison with the southern highlands (Figure 2.6). The CRISM data shows that besides the mafic mineral difference, many secondary mineral summary products have high values for the northern lowland region (Figure 2.6). This could suggest a chemical weathering process in aqueous conditions. However, because of the low values of the band depth products (e.g. third decimal place numbers for BD2250 in Figure 2.2) and the lack of a spatial coherent pattern at the original MRDR resolution, this study is unable to be conclusive regarding the presence of secondary minerals in the northern lowlands. Furthermore, previous studies with the OMEGA instrument concluded that secondary mineral absorption features are rare to absent in the northern lowlands [19]. The compositional change between the major surface types in the southern highlands, northern lowlands and dust-covered regions seems to be gradual and classified as a separate surface type, called the transition zone here (Figure 2.4: cluster 15 Viviano-Beck, cluster 5 Pelkey).

Much of the variability in the data is related to the dust coverage on Mars. This can be observed in the number of pixels that classify in the group dust-covered region (38 %of the pixels classify as cluster 9 in Figure 2.4) and the number of summary products with a moderate or high correlation with the dust cover index of Ruff and Christensen [88] (Figure 2.3). The products related to this surface type are interpreted as the result of the high albedo of the dust and the dusts' ferric component. The ferric component of the dust is often referred as nano-phase ferric oxide [31]. Here the products BD5302 and RPEAK1 are interpreted to be related to the ferric component of the dust. The products OLINDEX and CINDEX are revised by Viviano-Beck et al. [106] because of their sensitivity to high albedo, giving false positives for the interpretation of olivine and carbonates. In contrast with previous studies, our study has highlighted a few different regional groupings (Syrtis Major together with Sinus Meridiani and Meridiani Planum with Nili Fossae), as well as a few new regions of spectral distinctions (e.g. Ophir Planum, Solis Planum and Hellas Basin). As will be described, the previously unrecognized regional groupings show spectral similarities which can be interpreted for the local geology. However, also the averaging and thresholding process used to create the input maps had significant influence on the regional grouping (Section 4.1). The new spectral distinctions (Section 4.2) are discussed whether these might represent previously unrecognized regional differences in composition or surface properties (Section 4.2.1), or are the result of influences of external factors such as dust and ice. The uncertainties of our work and additional explanation on how to interpret our results are discussed in Section 4.3.

2.4.1 New regional groupings

2.4.1.1 Nili Fossae and Meridiani Planum

The regions Nili Fossae and Meridiani Planum classify in this study as similar surface types because of the interpreted high olivine and secondary mineral content. The high olivine content is indicated by the positive impact of the OLINDEX3 product and secondary minerals content indicated based on the products BD1900 and D2300 (Figure 2.6 and Table 2.1).

The interpretation of the summary products of secondary minerals is found difficult because at the original resolution the products lack a clear spatial coherent pattern (BD2250 as an example of a secondary mineral product in Figure 2.2). Also the summary product values of the secondary mineral products are small (third decimal values for BD2250) which introduces some uncertainty because the features cannot easily be recognized in the spectra. The summary products D2300 is displayed at original resolution in Figure 2.7 for the regions Meridiani Planum and Nili Fossae to demonstrate that the pixel values are spatially coherent and can be related to the local geology (Figure 2.7). The local geology is indicated in black, outlining the boundaries of Meridiani Planum and Syrtis Major from the geological map of Tanaka et al. [2014]. Grey squares indicate the outline of the clusters in this study. At the original resolution it can be noticed that the high values of D2300 are occurring within the outline of Meridiani Planum. On this plain both in-situ as orbital observations have detected sulfate evaporates, and Fe/Mg phyllosilicates silicates formed by aqueous alteration [96]. Both D2300 and BD1900 describe spectral features related to Fe/Mg phyllosilicates [106]. The low values of the sulfate index (SINDEX Table 2.1) and lack of a BD1750 feature region suggests that the presence of sulfates could not be detected with our analysis.

For Nili Fossae the product D2300 shows locally high values (Figure 2.7). The region Nili Fossae is often described in literature in relation with the presence of secondary minerals such as carbonates and Fe/Mg phyllosilicates [17, 31]. In these studies, hydrothermal alteration is often named as the circumstance where these minerals have formed. Both carbonates and Fe-Mg phyllosilicates have spectral features around 2.3 and 1.9 μm, and both minerals can form under hydrothermal circumstances.

The OLINDEX3 map is most similar to the mean fractional contribution map for olivine by Koeppen and Hamilton [59] based on the data of the TES instrument. In their study the mean abundance of olivine is relatively high in the regions that overlap with the surface types Nili Fossae and Meridiani Planum in this study. Other surface type studies such as Rogers and Hamilton [87], Hamilton and Christensen [39] [2005], and [45] have also found Nili Fossae to be distinctly mapped because of the high olivine content. Although the values for OLINDEX3 are relatively high for Nili Fossae compared to the rest of Mars, in our maps these are not significantly different compared to the rest of Meridiani and Syrtis. This is different from the olivine maps produced with the TES [5, 59] and OMEGA [77] data. This difference can be explained by the effect of averaging and thresholding of the pixel values that causes masking of the extreme values. A close look at OLINDEX3 product in Nili fossae shows that some high values in this region are masked out because of the defined threshold.

Besides the presence of secondary minerals, other orbital studies have found that Meridiani is unique because of the presence of iron-oxide minerals, especially hematite [23]. Product SH600 is able to capture the presence of hematite Viviano-Beck et al. [106]. The values for this product are high in Meridiani Planum but not significantly higher than the adjacent region Margaritifer Terra (which is not a separately classified surface type in this study).

2.4.1.2 Syrtis Major and Sinus Meridiani

One of the aspects that distinguishes the surface types Syrtis Major and Sinus Meridiani class from the other regions in the southern highlands is the low dust coverage, with the lowest values for all the dust coverage products (see negative weights for dust products in Figure 2.6). Beside the dust, the regions are characterized by high positive values for several secondary mineral products and the OLINDEX3.

In contrast to the previous section on Nili Fossae and Meridiani Planum, there are some doubts whether the OLINDEX3 indicates a high olivine content in Syrtis Major and Sinus Meridiani. These doubts are based on the fact that none of the other olivine maps by the TES or OMEGA instruments indicated high olivine content in this region. This difference might be explained by the fact that the OLINDEX3 is also sensitive to the 1 μm feature of high-calcium pyroxene [106]. The high-calcium pyroxene content is often related to what makes Syrtis unique in other surface type studies [Rogers Hamilton, 2015; Riu et al., 2019]. The elevated high-calcium content in this region would result in high values of the HCPINDEX, which is not the case in this region. Similar to the olivine index values in Nili Fossae, this could be related to the fact that the high values of the HCPINDEX parameter are masked out by the thresholding process and averaging of pixel values (see white pixels in Figure 2.2).

Several secondary mineral summary products have high values in Syrtis Major. One of those products, BD21002, is displayed in Figure 2.7 for both Syrtis Major and Meridiani Planum. BD21002 appears to be more noisy and does not show a clear distribution compared to D2300. This lack of a clear spatial distribution was found for all the secondary mineral summary products related to Syrtis and Sinus Meridiani. Also several secondary mineral summary products appear to be correlated with the dust-coverage (Figure 2.3). These summary products have high values within Syrtis Major but not significantly different from other low dust-covered regions such as northern lowlands, and locally in the southern highlands. Therefore it remains difficult to conclude on the presence of secondary minerals in this region.

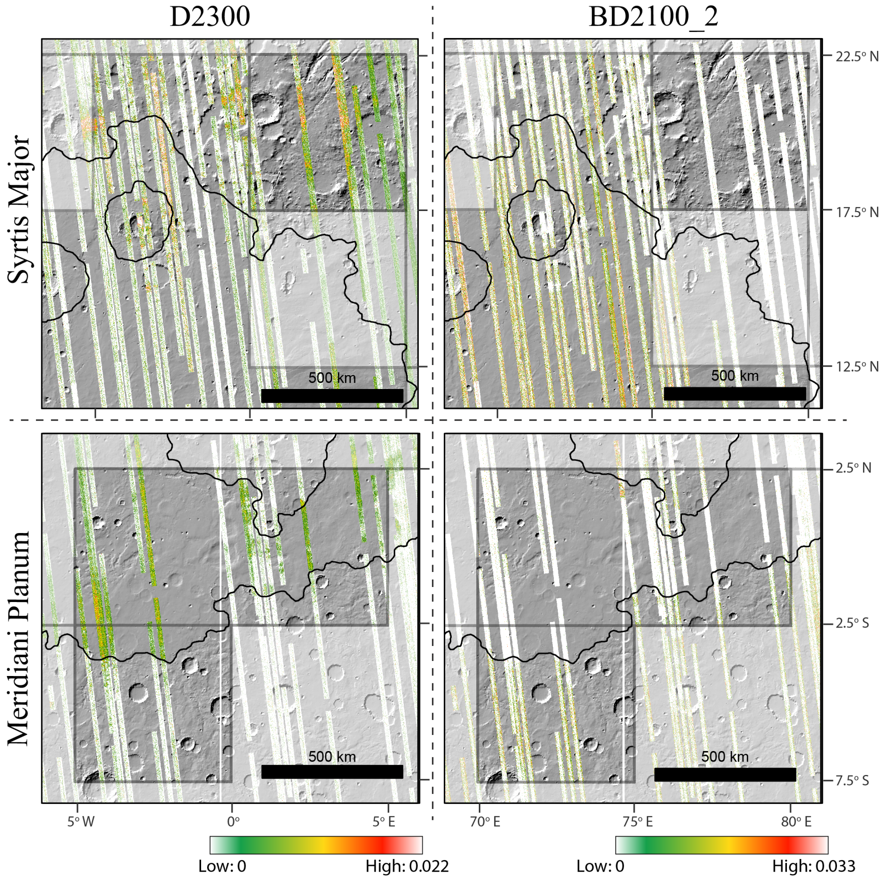

Figure 2.7 Summary product maps of Syrtis Major, Nili Fossae, Sinus Meridiani and Meridiani Planum for the products D2300 and BD2100$_2$. The grey squares indicate the outline of the $5^o * 5^o$ grid size pixels for the above described classes. Black outline are the boundaries of Meridiani Planum and Syrtis Major on the geological map of Tanaka et al. [97]. The color scale represents low values in green and high in red. The white pixels are those with values higher or lower than the defined thresholds.

2.4.2 New spectral distinctions

As described in the Methodology Section the clustering analysis is performed with a top-down approach so that the clusters that are most distinct are identified first. Most of the most distinct clusters have been recognized as spectrally distinctive in previous studies that utilized infrared spectroscopic data sets.. But several clusters of this studies appear new, in comparison with other surface type studies with the OMEGA and TES datasets such as: Hellas, Volcanoes, Promethei Terra, Solis Planum, Ophir Planum, Medussae Fossae. However, for some of these regions the summary products with high impact or defining these regions are interpreted to be related to non-geological conditions such as dust coverage and local atmosphere conditions. These regions are for example the dust-covered regions and the volcanic regions, and Hellas (Section 4.2.2 clusters of non-geological origin). For the clusters Ophir Planum, Solis Planum, Promethei Terra and the higher northern and southern latitude zones it is not well understood whether the spectral uniqueness is related to geological processes or external factors. Since these clusters are new, and overlap with established geological units, the uniqueness of these clusters in the data is discussed in Section 4.2.1 clusters of potential geological origin.

2.4.2.1 Clusters of potential geological origin

Cluster Solis Planum covers in both datasets the Hesperian volcanic region on the geological map of Tanaka et al. [97]. Although the cluster is named the same in both the Viviano-Beck and Pelkey dataset their spatial coverage is different in that the cluster in the Viviano-Beck data extends more to the North towards the Tharsis region. In both datasets the spectral difference with other units is minor, which can be observed from the low Euclidean distance (Figure 2.5). The regions are characterized by high spectral slope (ISLOPE) values and low values for secondary mineral and olivine summary products. Previous laboratory spectral studies have shown that a continuous spectral slope between 1.8-2.5 μm can arise from either the result of acidic alteration of basaltic glass [49], rock exposure [41] or ferric coating on dark rocks [35]. The lower values for hydrated mineral summary products could be explained by more recent volcanism, of which the rocks might have remained unaltered. The low values for OLINDEX3 remains unclear, especially because the detailed studies of Viviano et al. [105] concluded that the composition of this region is similar to other Hesperian regions on Mars.

Ophir Planum is a cluster which consists in both datasets of several of pixels north of Valles Marineris. The high values in this regions for the summary products SINDEX and BD1900 could indicate the presence of sulfate minerals in the region. Cluster Ophir Planum overlaps with some of the chaos terrains in Margaritifer Terra that contain earlier identified light toned deposits [Glotch Rogers, 2007]. The identified sulfate deposits in these interior layered deposits could be a reason for the higher values for the products SINDEX and BD1900 [37]. However both products are also known to be sensitive for the spectral features of ice. This in combination with the lower values of the ICER product in both datasets could also imply the presence of atmospheric water ice. The presence of atmospheric ice in this region is also mentioned for its occurrence during the aerocentric solar longitudes Ls 0-180 [7].

Several clusters, in both dataset, cover the larger basins on Mars, Hellas and Agyre (Figure 2.4). Clusters 3- Hellas Basin and 13 - Promethei Terra are in both datasets classified first and were distinguished with high Euclidean distances (Figure 2.5). The spectral uniqueness of this region is related to the missing values of the summary products using wavelengths > 3 μm as described in the Methods Section 2.2.2. Also the clusters Hellas North and Hellas middle appear spectrally unique with high Euclidean distance with the other clusters. The secondary mineral summary products for example have low values for this region, while the products OLINDEX3, SH6002 and SINDEX have high values. However, studying the individual global summary product maps, it seems that all products have unique values in this region. The known circumstances of high opacity due to dust in the atmosphere [78] and the presence of ice clouds [53] complicates the interpretation whether mineralogy contributed to the spectral uniqueness or these external effects.

2.4.2.2 Clusters of non-geological origin

In addition to the surface types of potentially geological origin, some classes in the clustering analysis such as the volcanoes and the higher latitude zones result from unique summary product values which are interpreted to be of non-geological origin. In the Methods Section 2.2.2 it was already mentioned that several summary products were not used for the analysis because of their high correlation with the elevation ((Pelkey: ICER2, BDCARB; Viviano-Beck: BD1400, BD1435, BD1900R2, BD2200, BD2355, ICER2, BD3000 Figure 2.3). These summary products are interpreted here to be related to the atmosphere thickness.

Not just globally, but also local atmospheric conditions seem to affect the spectra and therefore the summary products. In particular, the pixels covering the elevated volcanoes on Mars are classified as separate surface types because of high values of BD1500, SINDEX, CINDEX, BD3100, BD3200, BD3400 (Table 2.1). These products can be associated with spectral features of sulfate and carbonate, but here we think that they are affected by the local atmospheric conditions around the volcano. It is known that the atmosphere around the volcanoes hosts ice clouds [7], and from the products BD1500 and SINDEX it is known that these are sensitive for H2O and CO2 ice, respectively [106]. Also, the other products capture spectral features that overlap with any of the H2O and CO2 ice spectra. Our two classification maps (Figure 2.4) have both have regions in the higher latitudes that cluster separately. It seems that although most of the polar pixels are excluded, the regions up to 60o latitude are affected by seasonal changes, resulting in spectral differences between orbital strips within the mosaics. Such abrupt spectral changes around 60o latitude were also observed by Pelkey et al. [82] in the OMEGA and

CRISM dataset, and related to season changes.

2.4.3 Uncertainties

In this study choices were made that impacted on the uncertainties/ accuracy of the results. First of all the summary products were normalized and standardized for the region between the 67.5^o latitudes. Therefore, some products that were developed to study ice around the poles, are used to study surface composition where ice might not be expected. We assumed that when the poles are excluded, these summary products describe spectral features that can be related to mineralogy. Also, the normalization and standardization, together with the defined thresholds could have resulted in enhancement of noise within areas of low spectral variation.

The use of thresholds based on quartile distances has proven to be a good method to exclude unrealistic data values. But for some products such as OLINDEX3 in Nili Fossae, it might have masked relevant information. The averaging over such a large grid helped to overcome some of the problems with radiometric differences between strips and smoothened the data.

It was also mentioned in the papers of both Pelkey et al. [82] and Viviano-Beck et al. [106], that the use of summary products contains caveats, and interpretations have to be done with care. Therefore, as a reminder, the interpretations resulting from this study are based on averaged summary products over 5^o*5^o pixels and for a global perspective. Some interpretations might not apply to the original resolution of the MRDR summary product maps since higher resolution data provides more detailed information.

2.5 Conclusions

The global multispectral CRISM data has shown to be a useful dataset for global surface type classification. For the first time, both the spectral parameters of Pelkey et al. [82] and Viviano-Beck et al. [106] are used to capture the small spectral features of the CRISM mapping mode data and interpreted for the local mineralogy. However, several assumptions had to be made such as averaging for a 5^o*5^o grid, and defining thresholds to mask unlikely values. These assumptions had to be made to deal with radiometric differences between strips in the CRISM MRDR data. With a novel and transparent approach, including a combination of multivariate data-analysis techniques, we have classified Syrtis Major, Nili Fossae, Meridiani Planum, Sinus Meridiani, northern lowlands and southern highlands and the global dust deposits as separate surface types, consistent with previous global spectral studies [Bandfield et al., 2000; Rogers et al., 2007; Rogers Hamilton, 2015; Riu et al., 2019]. The effect of external factors such as the dust coverage and the elevation on the summary products is studied using correlation coefficients. The Viviano-Beck products BD1400, BD1435, BD1900R2, D2200, BD2355, ICER2 and BD3000; and the Pelkey products ICER2 and BDCARB were found to be correlated with elevation, which is considered to be inversely related with atmosphere thickness. The clusters covering the higher latitude zones, Hellas and the volcanoes are interpreted to be of non-geological origin, and found to be related to atmosphere conditions, dust-coverage, atmosphere conditions, or missing values in the data. Surface types Solis Planum, Ophir Planum are new in comparison with surface type studies done with other global datasets. For these the geological interpretation of the spectral variability is more uncertain whether it is can be related to geology or possible atmospheric ice.

Mars in the lab

3

Summary products have become commonly used parameters to describe shallow spectral absorption features of both global multispectral and targeted hyperspectral CRISM images [82, 106]. Although such products are useful to describe a mineralogical variation on the surface, various studies, including the one presented in Chapter 2, have shown that there is ambiguity in the interpretation of a summary product for a single mineralogy or rock type [106, 48]. So far, the studies evaluating the CRISM summary products are often performed by using single spectra of individual minerals [106, 48]. In practice orbital images consist of spectra of various mineral mixtures rather than a single mineralogy. Also, the studies on summary product evaluation are done based on spectra with a spectral resolution similar to the orbital data of CRISM measured in hyperspectral targeted mode [106], here the data was resampled to the spectral resolution of the multispectral mapping mode resolution of CRISM. The latter is the CRISM data used in both Chapters 2 and 5

This study tests the summary products calculated from spectral images of Mars analog rocks. These images are obtained in laboratory conditions with VNIR and SWIR imaging spectrometers. Because all studies within this thesis are done with summary products calculated on the CRISM multispectral data, the spectra here are resampled to this spectral resolution.

To get a good representation of the Martian surface a variety of rocks were measured. The collection contained volcanic rocks, sedimentary rocks, and rocks altered in either metamorphic or hydrothermal conditions. The presence of these rock types on Mars were described before based on in-situ or orbital measurements [31].

Often only the relatively high summary product values are interpreted for a mineralogy, but the applied methodology in Chapters 2 and 5 requires all summary product values, including negative summary product values. In particular, the negative values display a spatially coherent pattern that might be related to the local geology [55]. The benefit of using spectral images instead of single spectra makes it possible to test which values show a spatially coherent pattern and how this can be related to rock compositional variation. This way, for the first time not only the high values are interpreted, but also at other summary product value levels, the explained mineralogy is described.

3.1 Rock selection

As mentioned before a variety of volcanic, sedimentary, and altered rocks were chosen for spectral measurements (see Table 3.1). Most of the samples were from the rock collection of the Geoscience Laboratory of the Faculty of Geo-Information Science and Earth Observation (ITC). This selection is complemented by the measurements of the basalt rock samples collected from different lava flows on Hawaii by Annelotte Weert [107]. Also, the spectral measurements of the Pilbara greenstones of Exaud Humbo are used for this study [50].

The primary surface composition of Mars is considered as basaltic [5]. However compositional studies have also discovered local volcanic sequences with richer silicate mineral composition [22, 19]. Such an enrichment indicates that magmatic evolution has taken place, and therefore a large variety of volcanic rocks are included in the rock selection. In Table 3.1 these are categorized as intrusive and extrusive volcanic rocks.

Sedimentary rocks have been observed from orbit but also in-situ by the different rovers [103, 96]. The sedimentary units are interpreted to be deposited by rivers and lakes [66]. The analog sedimentary rock collection contains a variety of rocks with different mineral assemblages and grain sizes, for example, conglomerate, sandstone, and shale (see Table 3.1).

Mineral alteration on Mars can be related to both metamorphism and aqueous alteration. Metamorphism occurs at low grades compared to the Earth, therefore only rocks up-to greenschist facies are used for the measurements [70]. Hydrothermal alteration has often been interpreted for the presence of secondary minerals on Mars such as phyllosilicates and carbonates, especially in the region of Nili Fossae [104].

Lithology			Code	Additional information
Igneous	Extrusive	Basalt	ITCVR09	
			ITCVR13	Pyroxene phenocryst
			Hawaii samples	
		Andesite	ITCVR14	
			ITCIF01	Sanidine Feldspar Phenocrysts
			ITCVR03	Sanidine feldspar phenocrysts
		Rhyolite	ITCVR07	
			ITCVR01	
			ITCVR05	
	Intrusive	Peridotite	ITCVR11	
		Phonolite	ITCVR10	
			ITCVR12	
			ITCVR15	Trachite/phonolite
		Gabbro	ITCIF03	
		Diorite	ITCIM03	
		Volcanic glass	ITCVR08	Obsidian
		Volcanic bomb	ITCVR02	
		Granite	ITCIF02	Foliated
		Tuff	ITCVR04	
			ITCVR06	Welded
Sedimentary		Shale	ITCSE02	
			ITCMS04	
		Sandstone	ITCSE03	Bundsandstein
		Greywacke	ITCSE06	
		Sulfate evaporite	ITCSE04	Anhydrite-gypsum
			GYPSUM	
		Chlorine evaporate	SALT	
		Phosphorite	ITCSE05	
		Conglomerate	ITCSR01	
		Dolomitic evaporate	ITCSE01	
Altered	Metamorphic	Greenstone rocks	179822,179825-179826,179864-179865,179867-179878	
		Serpentine	ITCIM01	
		Schist	ITCMS02	Biotite, chlorite, muscovite schist
		Phyllite	ITCMS01	
		Amphibolite	ITCMG01	
	Hydrothermal	Greenstone rocks	179822,179825-179826,179864-179865,179867-179878	
		Alunite	XRD14106	

Table 3.1 Rock selection describing the lithology and codes associated to ITC Geoscience Laboratory sample library

3.2 Measurements

In this Mars analog Mars study, spectral images were acquired of sawn samples to create a flat surface for the measurements. This surface was leveled at the focus point of the camera. The samples were placed on top of a black-painted blanket in a sand-filled box. The blank paint applied to the blanket was relatively featureless in the VNIR and SWIR and provided a contrast between the rock measurements and the background.

The images in the VNIR and SWIR wavelength ranges were taken with two separate SPECIM hyperspectral camera's [95]. The SWIR camera is placed in the lab scanner set-up with a moving platform to scan the sample box. The camera measures the reflectance for the wavelengths between 1-2.5 μm in a spectral resolution of 12 nm. The camera's OLES30 lens has an image swath of 9.8 cm and a pixel-size of $\sim 260\ \mu$m. Raw image data were converted to reflectance values using white reference and dark current measurements.

The VNIR camera is used with the SPECIM ArtScanner [95] set-up where the camera instead of the sample platform was moving. The VNIR camera had a different lens and was therefore placed further away from the camera resulting in a smaller pixel size of $\sim 350\ \mu$m. The wavelength range covered was between 0.4-1 μm and a spectral resolution of 2.8 nm.

The images were spectrally resampled to the CRISM wavelengths in multispectral mode (72 bands: 16 VNIR, 56 SWIR) [74]. The central band wavelengths and full-width half-maximum resolution of the visible and near-infrared detectors were used to do the spectral resampling. The resampled multispectral images are used to calculate the summary products using the script of the CATENVI CRISM processing software [72]. Because the SWIR instrument only measured up to 2.5 μm several products requiring reflectance spectra at wavelengths higher than 2.5 μm could not be calculated. These omitted summary products included BD3000, BD3100, BD3200, BD3400, and CINDEX.

The total dataset of this study included in total 68 rocks, and for each rock 43 summary products were calculated. Because of a large amount of data, there was decided to confine the analysis to a selection of the summary products. Several summary products describe band depths of spectral features which are commonly used in remote sensing studies and their limitations are well described in the literature. This study focused on the summary products specifically designed for the CRISM data, or those that caused confusion in the global analysis in Chapter 2 or Chapter 5. Each of the considered summary products is listed in Table 3.2 categorized as those describing spectral features of primary minerals, secondary minerals and non-minerals. In Appendix 1 it is shown what part of the spectrum the product is calculated for representative spectral library spectra.

For each of these summary products, the results present the stretching values used to analyze the rocks including corresponding colorbar. The rocks were studied for spatial coherent patterns which could represent a difference in rock composition. Spectra and other summary product combinations were used to interpret the observed spectral differences described by the summary product.

3.3 Results

Category	Minerals	Summary products
Primary minerals	Mafic (non-specified)	VAR, BDI1000IR, BDI1000VIS, BDI2000
	Olivine	OLINDEX3
	Pyroxene	HCPINDEX2, LCPINDEX2, BD860, BD920
	Felspar	BD1300
Secondary minerals	Sulfate	SINDEX
	Iron oxide	SH770, SH600, RPEAK1,
Non-mineral	Ices	ICER1
	Other	ISLOPE-1

Table 3.2 Selection of the analyzed summary products categorized as those designed to describe spectral features of primary minerals, secondary minerals or non-mineralogical features such as ice

3.3.1 Primary minerals

3.3.1.1 Olivine

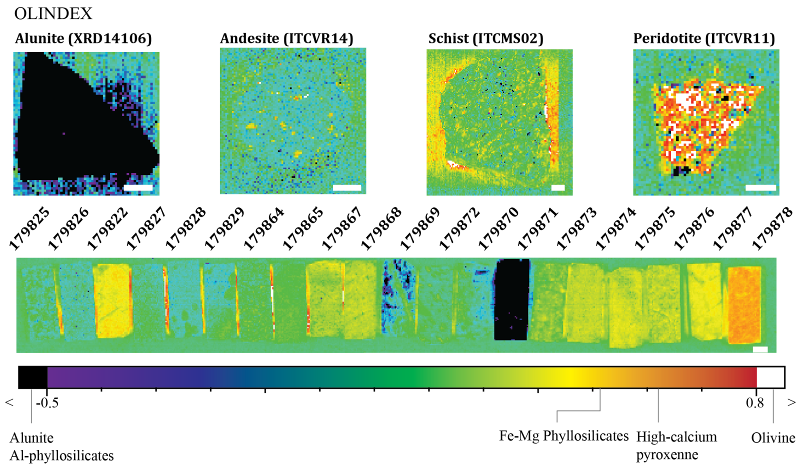

Figure 3.1 Variation in OLINDEX3 values for the rocks alunite, andesite, schist, peridotite and Pilbara rock samples.

The olivine index, OLINDEX3, is designed to describe the wide absorption feature of Fe^{2+} characteristic for olivine minerals. The high values for the peridotite (ITCVR11) in Figure 3.1 show that this product successfully describes the presence of olivine minerals. Besides olivine, the product gives relatively high values for the high-calcium pyroxenes within the peridotite (ITCVR11) and andesite samples (ITCVR14)(see later Section 3.3.1.2). The variance in OLINDEX3 values within the schist (ITCMS02) and the greenstones shows that this summary product also shows spectral differences within the spectra of secondary alteration minerals. The lowest values, negative values, represent alunite (XRD14106) and the illite/ muscovite minerals (greenstone 179871). The relatively high values are associated with Fe-Mg phyllosilicates, most likely chlorite minerals.

In Figure 3.2 the olivine index is tested whether it can be used to quantify the olivine content in basaltic rocks. Therefore, the Hawaii basalts collected by Annelotte Weert [107] were used. The olivine content percentages are based on optical microscopy of thin sections which are of the same slab measured with the imaging spectrometer and displayed in Figure 3.2. The results show that the highest olivine content for rock 18a3, based on optical microscopy, also resembles the highest OLINDEX3 values. However, between the other rocks there is no significant difference in OLINDEX3 values. None of the images show a noticeable relation in OLINDEX3 values in comparison with the observed olivine content in the rocks. Therefore the OLINDEX3 values can be used to indicate the presence of olivine but not used as a quantitative parameter for the olivine content within a rock sample.

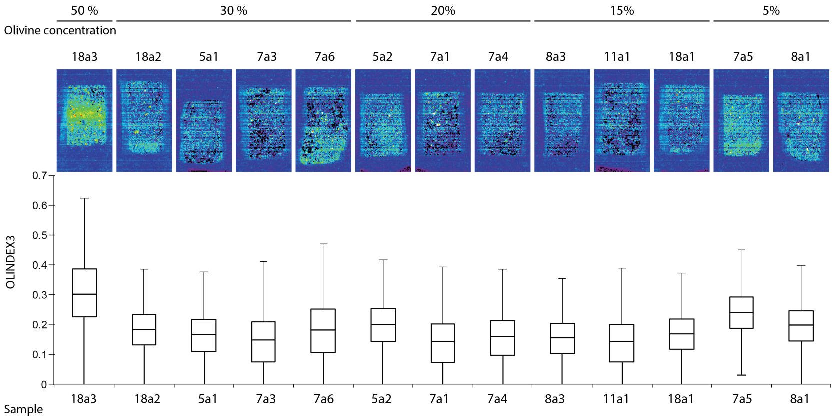

Figure 3.2 OLINDEX3 values calculated on the Hawaii basalts. Images ordered from an estimated high to low olivine concentration. Colorbar and values similar to the stretching values in Figure 3.1. the boxplots present the first, second, and third quartile and errorbars the minimum and maximum values.

3.3.1.2 Pyroxene

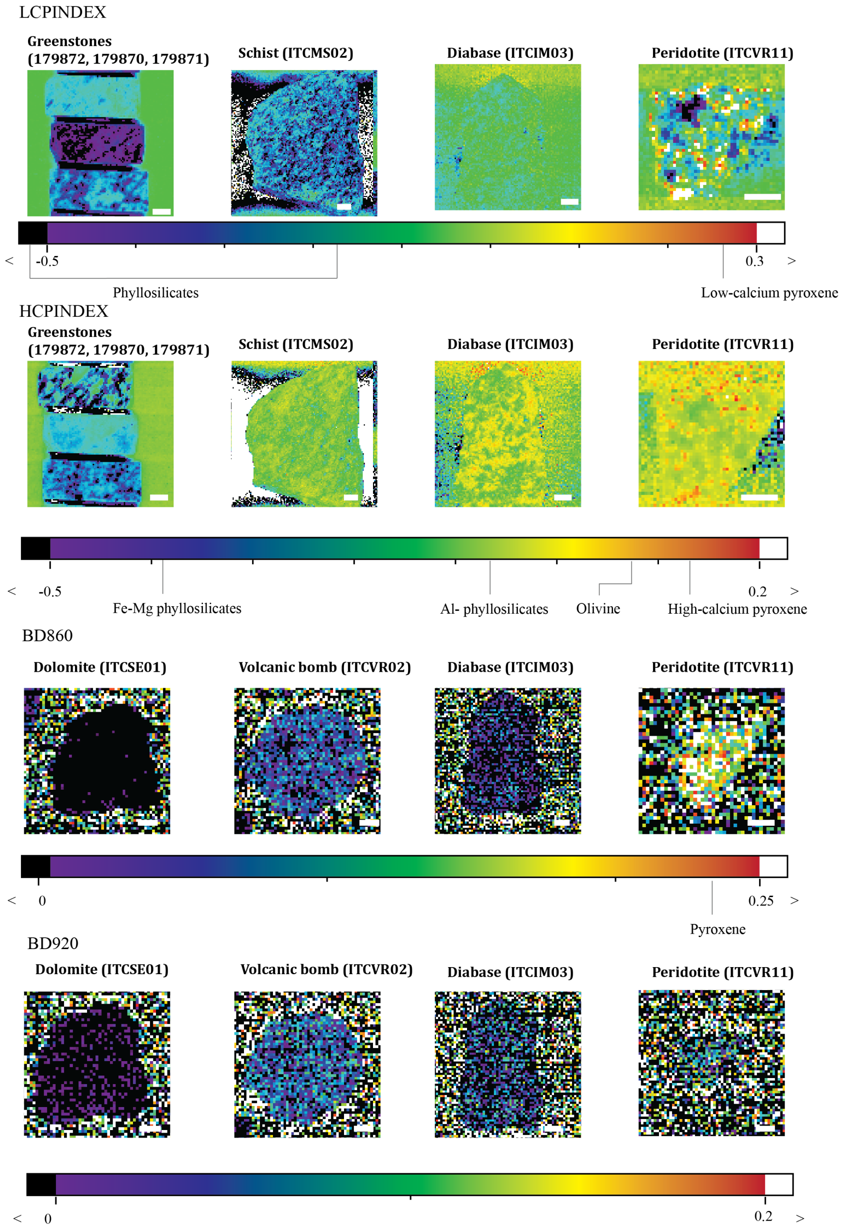

Figure 3.3 Variation in the products, LCPINDEX2, HCPINDEX2, BD860, BD920 for a variety of rocks.

The two pyroxene summary products LCPINDEX2 and HCPINDEX2, which should indicate spectral features of low-calcium and high-calcium pyroxenes respectively, show to be successful in identifying these minerals and do not contain many false positives for other types of minerals. In Figure 3.4 a color composite of mafic summary products is used to indicate the spectral variance within the peridotite. The colors display the compositional difference between olivine and differences between pyroxenes. The colors cyan and magenta show respectively the combination where LCPINDEX2 and HCPINDEX2, or OLINDEX3 and HCPINDEX2 display high values. HCPINDEX2 also shows high values for pyroxenes in the diabase (ITCIM03) and andesite (ITCVR14).
The LCPINDEX2 and HCPINDEX2 show clear differences in the production of negative values. LCPINDEX2 has low values for all hydrated minerals. HCPINDEX2, however, has relatively high values in for example the schist (Figure 3.3) for the pixels that contain the Al-phyllosilicates, illite, and muscovite.

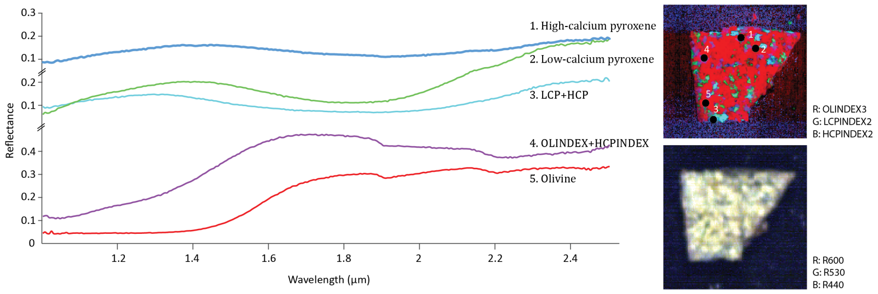

Figure 3.4 Color composite of mafic summary products of peridotite and selected spectra. R: OLINDEX3 (0-0.82) G: LCPINDEX2 (0-0.46) B: HCPINDEX2 (0-0.11)

The global maps from Chapter 2 show a correlation between the products BD860 and BD920. BD920 does not show any spatial coherent patterns. BD860 has the highest values for the peridotite, but because of the resolution of the data, it cannot be concluded whether this is related to either pyroxene or olivine minerals.

3.3.1.3 Mafic minerals

The response of the mafic summary products BDI1000IR, BDI1000VIS, and BDI2000 shows similarities to the olivine and pyroxene indices (see Figure 3.5). Just as for OLINDEX3, product BDI1000IR has the highest values for the olivine within the peridotite.

Also, BDI1000IR shows high values for the high-calcium pyroxene within the andesite (ITCVR14), and the Fe-Mg phyllosilicates within the schist (ITCMS02). BDI1000VIS is less sensitive to the spectral feature of these Fe-Mg phyllosilicates but instead has slightly higher values, for the diabase (ITCIM03), serpentine (ITCIM01) and amphibolite (ITCMG01). BDI2000 responds to the spectral features of pyroxene, especially for the peridotite rocks. Besides these higher values the variance is dominated by the low values for the phyllosilicates minerals within the rocks such as the schist (ITCMS01) and greenstones. The rationale for the VAR product in the paper of Viviano-Beck [106] is that it describes the spectral variance between 1-2.3 μm giving higher values for the spectra of the mafic minerals olivine and pyroxene. Neither of the volcanic rocks measured here show high values for the VAR summary product. Instead, the rocks containing secondary minerals for example the greenstones, dolomitic evaporite, and schist (Figure 3.5) have the highest values.

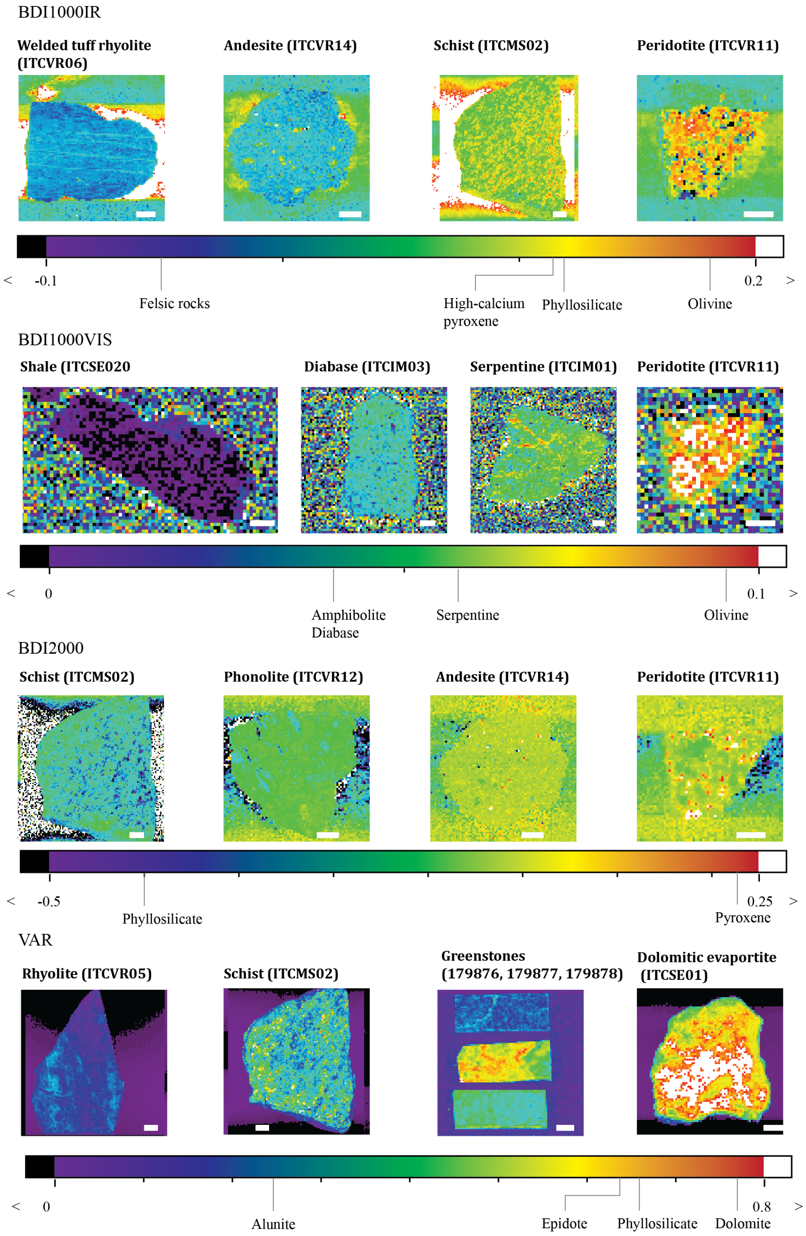

Figure 3.5 Variety in the values for products BDI1000IR, BDI1000VIS, BDI2000, VAR for various rocks

3.3.1.4 Feldspar

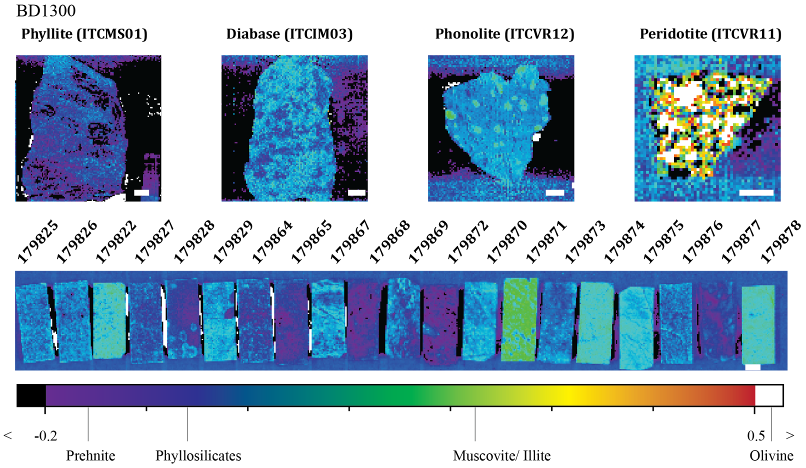

Figure 3.6 Variety in BD1300 values for the rocks phyllite, diabase, phonolite, peridotite and Pilbara basalts.

In the Viviano-Beck study [106] the BD1300 product is designed to indicate the minor Fe^{2+} substitution reaction for plagioclase minerals [106, 91]. Normally feldspar has no spectral features within the CRISM measured wavelength range but this spectral feature is locally observed in regions such as north of Hellas Basin [111]. This is a specific substitution which only locally is interpreted for the presence of feldspars. Besides the 1.3 μm absorption feature feldspar minerals are featureless in the short-wave wavelength range.
In the rocks measured for this study, neither of the high values for BD1300 is associated with a spectrum that could indicate the presence of feldspar minerals. Instead, the highest values for the BD1300 are for the olivine within the peridotite rock. Phyllite (ITCMS01) is one of the rocks with mainly negative band depth values, together with other sedimentary rocks such as greywacke (ITCSE06), conglomerate (ITCSR01), and shale (ITCSE02). All the greenstone rocks used in this study are included in Figure 3.6. Although the values of the summary product are low Figure 3.6 clearly shows differences between the different rocks.

3.3.2 Secondary minerals

3.3.2.1 Sulfate

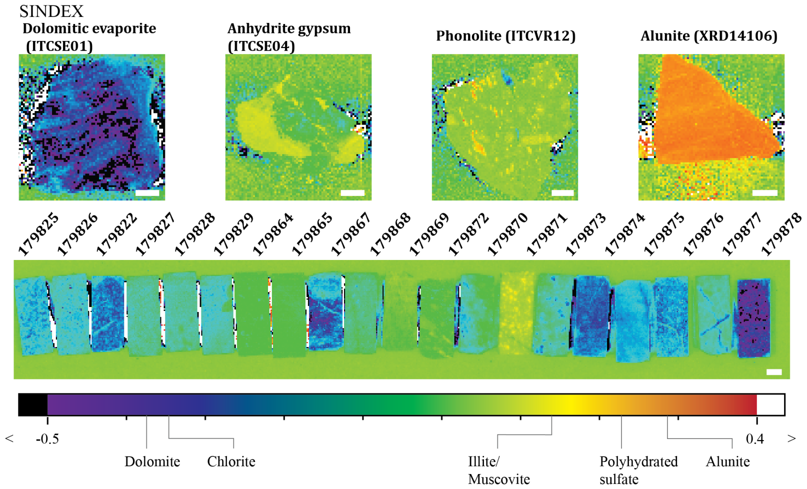

Figure 3.7 Spectral variance for the rocks dolomitic evaporite, anhydrite gypsum, phonolite and alunite of the summary product SINDEX

The highest SINDEX values are related to the alunite rock (XRD14106). For gypsum, for example (ITCSE04) the SINDEX values are not constant for the whole rock. Instead, it seems that the values relate to how well the hydroxyl feature near 1.435 μm is pronounced, indicating how hydrated the gypsum is. The high SINDEX pixels for phonolite do not show many spectral features and just strong absorption features around 1.4 and 1.9 and a dip towards 2.5 just like the gypsum ITCSE04 which probably consists of polyhydrated sulfate. The high SINDEX values for greenstone 179871 is the result of clear illite/muscovite spectral features.

The schist and the chlorite and dolomite containing rocks show the most variation within the low, negative numbers. Because the SINDEX describes the spectral convexity near 2.29 μm a negative SINDEX indicates the opposite so a concave spectral shape. Both dolomitic evaporite and some phyllosilicates have a spectral feature around 2.29 μm resulting in negative SINDEX values. Especially the Fe-Mg phyllosilicates have low values for the SINDEX and explain most of the variance of SINDEX values within the different greenstones.

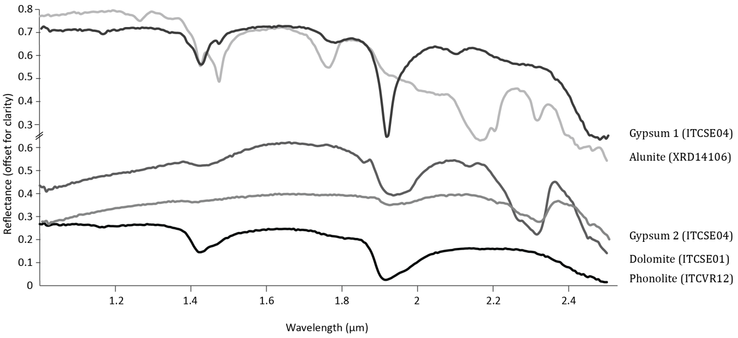

Figure 3.8 Reflectance spectra of alunite, gypsum, dolomitic evaporite and phonolite resembling unique SINDEX values

3.3.2.2 Iron oxides

None of the rocks measured contain ferric minerals such as hematite or goethite for which the shoulder products SH600 and SH770 are developed. Therefore the results in Figure 3.9 only contain potential alternative explanations or minor ferric weathering. The results however show low values for both shoulder products indicating minor spectral variation. Some variation, for example for the shoulder products for the bundsandstein and welded tuff, are found but just from the spectra, it remains difficult to conclude whether this is due to variance in ferric iron. The same applies to the product RPEAK1 which shows more variation than the shoulder products but also for this product no consistency is found with a specific spectral feature or spectral variation observed before in the infrared wavelength range. Probably this product is most suitable for surface remote sensing for which it can detect the difference between the Fe-mineralogy and dust on Mars[106]. To conclude, if this product describes ferric weathering, additional geochemical measurements are required.

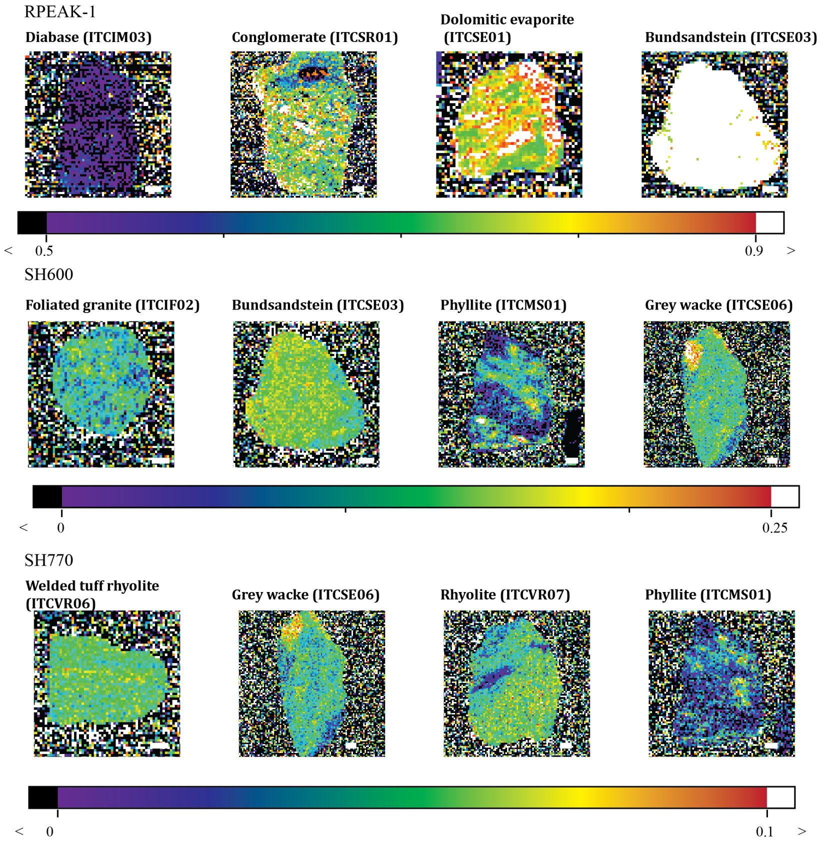

Figure 3.9 Variety in values for the products RPEAK1, SH600 and SH770 for various rocks

3.3.3 External factors

3.3.3.1 Spectral slope

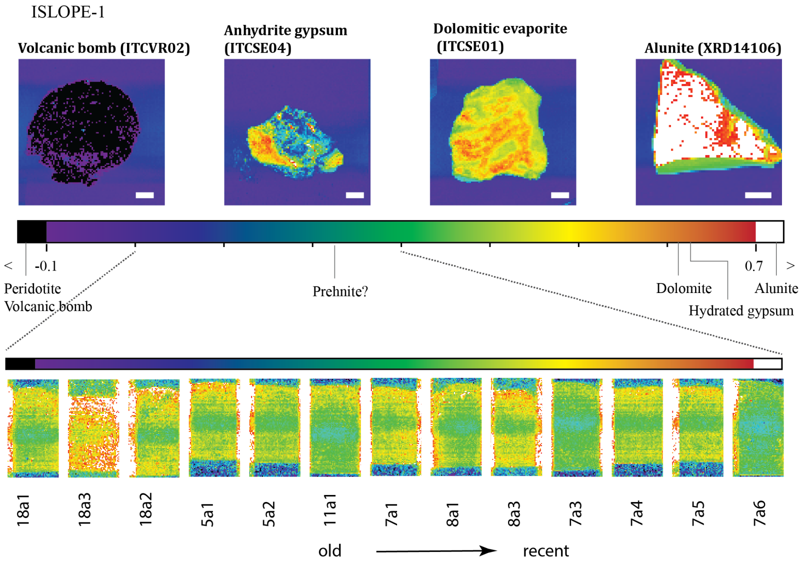

Figure 3.10 Variety of ISLOPE1 values for the rocks gypsum, volcanic bomb, dolomitic evaporite, alunite and hawaii basalts

The ISLOPE1 product describes a continuous spectral slope, with decreasing reflects towards longer wavelengths, between 1.8 and 2.5 μm which is characteristic for, for example, the spectral from the northern lowlands on Mars (Chapter 2). Here, non of the spectra of the Mars analog rocks has this characteristic spectral feature. Instead, the high ISLOPE1 values in this rock selection seem to be related to the minerals and rocks with absorption features near 2.5 μm. In Figure 3.10 this is shown for the gypsum (ITCSE04), alunite (XRD14106), and dolomitic evaporite (ITCSE01). The effect of this 2.5 μm absorption feature on the ISLOPE1 values is not described in the literature, and therefore we cannot conclude whether the ISLOPE1 values for the spectra on Mars are related to the continuous slope or affected by these spectral absorption features.

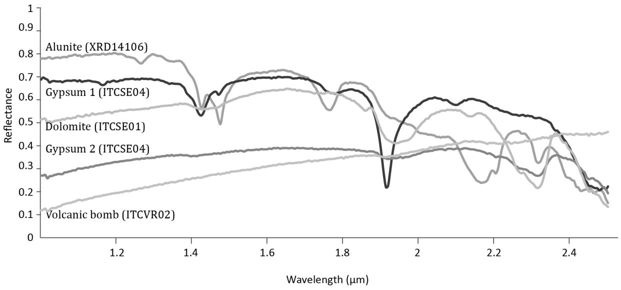

Figure 3.11 Reflectance spectra of alunite, gypsum, dolomitic evaporite and phonolite resembling unique SINDEX values

The basalt rocks selection from Hawaii were considered as a good analog to test for ISLOPE1 features and whether these can be related to weathering processes. In Figure 3.10 all measured rocks are shown ordered from old to recent, assuming that older basalt flows are more weathered, and therefore have higher ISLOPE1 values. However, just like the other rocks, the relatively high ISLOPE1 values do not resemble the continuous slope as observed for Mars spectra [75], but minerals with lower reflectance values near 2.5 μm instead. The Hawaii rocks are characterized by low ISLOPE1 values in the center of the rocks. The spectra of these pixels in the middle of the rock have higher reflectance values and no clear other spectral differences indicating a mineralogical difference. Therefore it is found most likely that this is an illumination artifact within these measurements. Similar differences in reflectance were not found for any of the other rocks.

3.3.3.2 Ices

Chapters 2 and 5 also included the ice product ICER1, describing the ratio between CO_2 and H_2O absorption features, for global surface studies. Therefore this product was tested for its applicability to describe geochemical variance. Figure 3.12 shows some of the results for the rocks peridotite, schist, anhydrite gypsum, and phosphorite. Because most minerals, except for epidote, have no spectral feature around 1.5 μm, the product ICER1 has a lot of similarity to the variance described by the summary product BD1435. Many products that describe a spectral feature around 1 μm are sensitive for olivine, as is ICER1. Other rocks that have high values for ICER1 contain hydrate minerals such as phyllosilicates or gypsum. How these product values relate to those of ice is difficult to determine. Especially because high ICER1 values are related to the presence of

CO_2 ice for which no representative spectra was found.

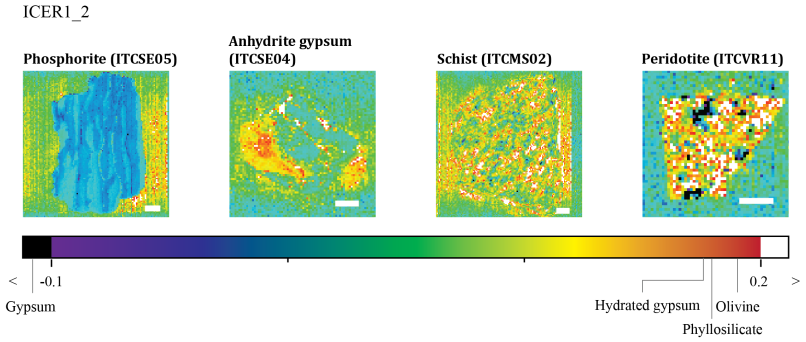

Figure 3.12 Variety of ICER1 values for the rocks phosphorite, gympsum, schist and peridotite.

3.4 Discussion

The results presented here emphasize the complexity of summary product interpretation. Besides the alternative interpretations, or caveats, which are consistent with those described in the publications of Pelkey and Viviano-Beck [82, 106], the results show some new caveats. In Table 3.3 the caveats described in the Results section are summarized and summary product combinations are proposed to verify the alternative interpretation. Only the products BD1300, ISLOPE-1, ICER1, and VAR contain new interpretations for the highest summary product values, other potential caveats for summary product interpretations are at lower summary product values. Each of these products is described in detail in the Results section.

Most of the products described for this study are non-unique and at different summary product values the interpreted mineralogy varies. Without any context of a spectrum or summary product combination it is difficult to conclude on a mineralogy. In general, the highest summary product values are for the mineralogy the products are designed for (e.g. OLINDEX3 for olivine). The alternative interpretations are presented in the Results section along the color gradient of the image to indicate how the different interpretations relate to each other at different summary product values. These different interpretations at various summary product value levels are also indicated in the summary product sensitivity matrix of Viviano-Beck et al [106] although only for the higher summary product values.

Differences in modes of different spectral instruments could cause differences in how well spectral features are pronounced. Therefore the stretching threshold values described in this study cannot be considered as absolute values that can be used as direct comparison with spectral data of other instruments. To do a mineralogical interpretation based on the summary products it is of importance that the interpretation is supported by examining summary products in combinations or by displaying the spectra (see proposed combinations in Table 3.3).

Not just the relatively high values are interpreted in this study, but as indicated before, also the low/negative values show spatial coherent patterns that can be related to mineralogical variation within a rock. As with the other interpretations of summary products these results are described within the range of values for each specific summary product discussed in the Results section 3.3. So far, this has never been done and therefore it is described here explicitly for the products OLINDEX3, LCPINDEX2, HCPINDEX2, BDI2000, VAR, and SINDEX in the Results section.

Summary product	**Rationale Viviano-Beck**	**Caveat**	**Combination product**
OLINDEX3	Olivine		
		Fe-Mg phyllosilicates	BD2250
		Pyroxene	HCPINDEX2
LCPINDEX2	Low-calcium pyroxene	-	-
HCPINDEX2	High-calcium pyroxene		
		Phyllosilicate	BD2250
		Olivine	OLINDEX3
		Pyroxene	HCPINDEX2
BD1300	Feldspar		
		Phyllosilicate	BD2250
		Olivine	OLINDEX3
BDI1000IR			
		Phyllosilicate	BD2250
		Olivine	OLINDEX3
		Pyroxene	HCPINDEX2
BDI1000VIS			
		Olivine	OLINDEX3
BDI2000			
		Pyroxene	LCPINDEX2,HCPINDEX2
VAR	Olivine and pyroxene		
		Carbonate	BD2350
		Phyllosilicate	BD2210
SINDEX	Sulfate		
ICER1	Ice ratio		
		Olivine	OLINDEX3
		Anhydrite gypsum	SINDEX
		Phyllosilicates	BD2250
ISLOPE1	Ferric weathering		
		Sulfate	SINDEX
		Carbonate	BD2350
		Phyllosilicates	BD2250

Table 3.3 Caveats of the studied summary products and recommended combination of summary product to verify the alternative interpretation

3.4.1 Instrumental uncertainties

As described before, the summary product values cannot be considered as absolute numbers that can be compared directly to spectral data of other instruments. The uncertainty of the data of the SPECIM instrument is that its spectra have a slightly convex shape for which the data is not corrected yet. The lower reflectance values towards the higher and lower wavelengths could impact some of the summary product calculations. Especially the product ISLOPE-1 could be sensitive for this spectral shape artifact because it calculates the slope between 1.8 μm and 2.5 μm, of which the latter is at the detection limit of the instrument. Because all data here are acquired in the same instrument set-up it is expected that this does not affect the observed relative trend, but must be considered when data are compared with those of other instruments.

3.5 Conclusion

In various ways, the work done in this study complements the previous summary product studies of Pelkey [82] and Viviano-Beck [106]. Before this study the revised summary products of Viviano-Beck were only tested at CRISM's hyperspectral spectral resolution for Mars analog rock spectra and here their applicability is tested for the first time at multispectral resolution. For most of the studied summary products, the spectral interpretation of the multispectral images is similar to those of the spectra at the hyperspectral spectral resolution of Viviano-Beck et al [106]. But, besides the already known caveats, some new alternative interpretations are included, for example for the products, VAR, ISLOPE, ICER1, SINDEX, BDI1000IR, BDI1000VIS, BDI2000. The mineralogical interpretations are presented along the range of the minimum and maximum summary product values of the rock samples. This way it was also found that the products do not only describe spectral difference for the high values but also in the low, negative values. The different interpretations at different summary product values emphasize the importance of defining the threshold values when using the summary products. As a result of the uncertainties of using summary products, the mineralogical interpretations need to be supported by either summary product combinations or by visual verification of the reflectance spectra.

Greenstones and a red planet[*]

4

4.1 Introduction

Both robotic and orbital measurements have confirmed the presence of phyllosilicates on the surface of Mars. Its occurence is of importance because it has indicated a wet and neutral acidity conditions in the Noachian period [9]. Minerals of the phyllosilicates mineral group can be formed in various alteration conditions, varying from hydrothermal alteration, diagenetic, and low-grade metamorphic conditions [28].

Each of these conditions have been interpreted for different regions of Mars [33, 104]. Metamorphism is restricted till low-grade metamorphic facies up to zeolite and sub-greenschist facies [70]. Hydrothermal alteration is often interpreted to explain the presence of the mineral groups carbonate, phyllosilicates [32], in for example Nilli Fossae region [104]. Here volcanic activity in Elysium provided the required heat source for the hydrothermal water circulation.

Understanding in which conditions the phyllosilicate minerals forms is crucial to understand the past conditions on Mars. For example hydrothermal conditions are suggested as one of the potential locations in which life could have started.

In western Australia, specifically the Pilbara craton, is build up of rocks which are considered to be a good Mars analogue for the two processes described above [17]. These rocks are similar in basaltic lithology and are formed around the same age (∼3.5 Ga [1]). Chlorite is one of the abundant minerals in these rocks. Chlorite minerals are mineral sub-group of phyllosilicates, that are known to form in the different conditions. Spectral orbital studies have detected this mineral for various locations on Mars [104]. In this study the rock samples from the Pilbara Craton sampled by Brauhart [13] and Smithies [1, 94] are studied for spectral variations which can be interpreted for the geological origin.

---

[*] This chapter is based on: Kamps, O. M., Van Ruitenbeek, F. J., Mason, P. R., Van der Meer, F. D. (2018). Near-infrared spectroscopy of hydrothermal versus low-grade metamorphic chlorites. Minerals, 8(6), 259.

4.2 Pilbara Craton

Samples were investigated from the Pilbara Craton, Western Australia, a region formed by a combination of vertical and horizontal tectonic processes [62]. Despite its age, the craton has experienced little deformation and stayed relatively stable for a long time [44]. The craton can be divided into multiple terranes, basins, granitic complexes, and greenstone belts [101]. The rocks used in this study were taken from greenstone belts that have been metamorphosed from lower greenschist up to amphibolite facies [94]. The hydrothermally altered rocks are from a volcanogenic massive-sulfide (VMS) deposit in the Panorama district in the Soanesville greenstone belt. Alteration processes involving seawater and heat from the granitic intrusion modified the rocks and formed the VMS deposits [13].

4.3 Method

4.3.1 Samples

This study requires a selection of samples with a well documented geological context. The samples collected by [94] are especially collected so that they are unaltered. On the other hand, are the samples of [13] collected to study the alteration processes.
The rocks used in the metamorphic dataset of this study were originally collected by [94] as transects in seven different greenstone belts in the Pilbara Craton. In total 243 samples of metamorphic rocks were sampled from 19 different transects. For the hydrothermally altered dataset, we used samples collected by Brauhart [12]. They include 445 outcrop samples from the Panorama district in the Soanesville greenstone belt.

4.3.2 Geochemical analysis

Bulk rock geochemical data, chlorite compositions as well as spectral measurements are taken from previously published studies [102, 1, 94, 14, 12]. The hydrothermally altered dataset contains bulk rock major and trace element measurements determined by X-ray fluorescence (XRF) [14], chlorite compositions measured by electron microprobe microanalysis (EMP) [12], and spectral analysis [102]. In addition to the elemental and spectral measurements, the hydrothermally altered dataset contains temperature estimates for a selection of the rocks [11]. The metamorphic dataset contains measurement of the bulk rock composition (XRF) [94] and spectral analysis [1].
Since the metamorphic dataset lacked comprehensive chlorite compositional data, a selection of 13 representative rocks were measured using a JEOL JXA-8530F HyperProbe (JEOL, Akishima, Tokyo,

Japan) equipped with a Field Emission gun, at a beam current of 15 keV at the Faculty of Geosciences, Utrecht University. The selection contains two samples per lithology, that all contained chlorite as dominant mineral in the spectrum. One ultra-mafic sample, metamorphosed in the amphibolite-facies, was included to test the influence of amphibole minerals on the spectrum and bulk rock composition. The number of measurements per sample varies from 4 to 53, without preference for specific chlorite minerals in thin section. The variation in measurements per samples can be explained by the differences in chlorite content per sample aswell as variations across-mineral transects. These transect measurements measure multiple points from the core to the rim of the chlorite mineral, which would make it possible to study element variation inside individual chlorite minerals.

4.4 Results

Two examples of chlorite reflection spectra were selected from both datasets based on the highest and lowest magnesium number, as measured by [89, 1], and are shown in Figure 4.1. The vertical lines show the characteristic absorption features of chlorite, including: 1400 nm OH, 2250 nm Fe-OH, and 2350 nm Mg-OH absorption. Comparing these chlorite reflection spectra in Figure 4.1, shows some shifts in the absorption depth and wavelength.

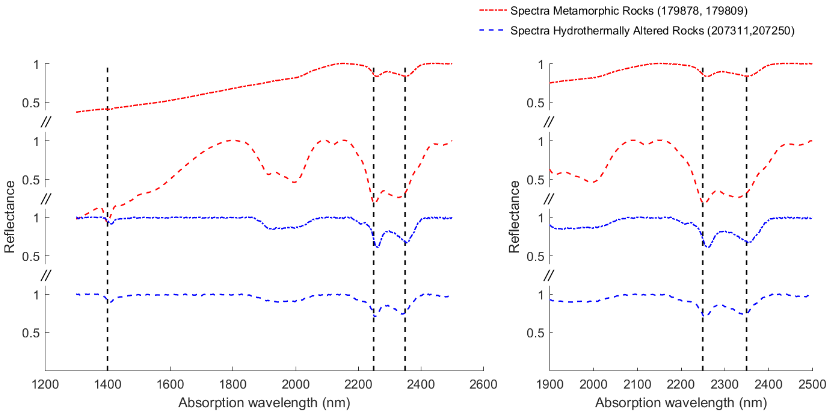

Figure 4.1 (a) Four chlorite specifc reflection spectra from both the hydrothermal and metamorphic datasets; (b) zoom-in area of soame spectra between 2150-2450 nm. The vertical lines highlight the characteristic absorption features of chlorite used in this study. 1400 nm: -OH absorption feature; 2250 nm: Fe-OH absorption feature; 2350 nm: Mg-OH absorption feature

To test these variations in spectral features, all reflection spectra from basaltic rocks containing chlorite have been compared.The results show that there is a significant difference, $p < 0.001$ for the Wilcoxon signed rank test, between the Mg-OH absorption wavelength near 2350 nm of the metamorphic rocks and the hydrothermally altered rocks. Figure 4.2 shows a scatter plot including a corresponding boxplot in which the spectral features are compared with the magnesium number calculated from the bulk rock composition.

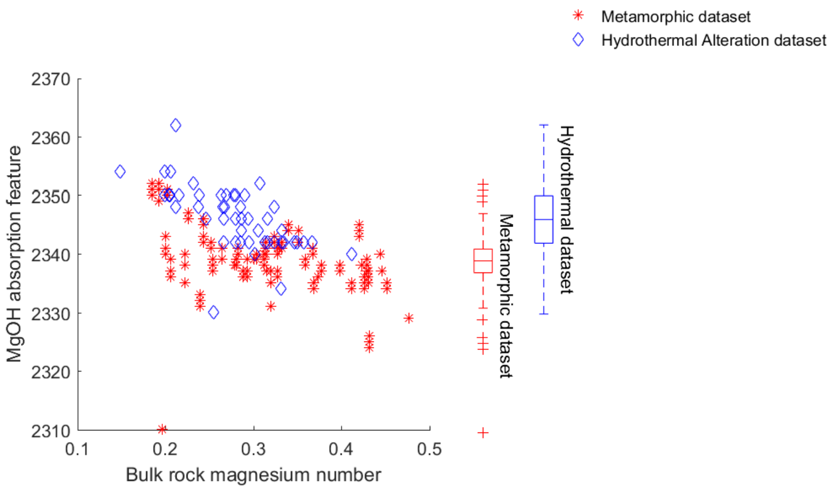

Figure 4.2 (a) Comparison of the absorption wavelengths of the Mg-OH absorption feature of chlorite for both the hydrothermal and metamorphic datasets (y-axis) and the magnewsium number calculated from the bulk rock composition (x-axis); (b) Boxplots show the quantiles of the absorption wavelengths for both groups of data

To gain a better understanding of the absolute concentration of magnesium and iron, these elements are plotted in Figure 4.3a. It can be seen that the variation in magnesium content is greater for the metamorphic dataset, while the hydrothermal dataset shows a greater variation for iron. These differences must be taken into account when comparing the magnesium numbers of both datasets.

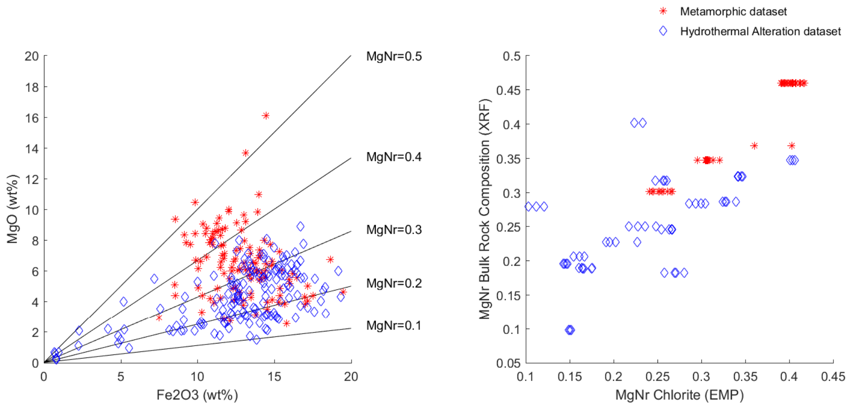

Figure 4.3 (a) Absolute bulk rock weight percentages (wt %) of MgO and Fe2O3; (b) Comparison of magnesium numbers of chlorite (x-axis) and bulk rock composition (y-axis).

When the bulk rock magnesium number is compared with the magnesium number calculated for the chlorite minerals in the same sample, a linear trend can be observed (Figure 4.3b). Two theories can explain this observation. First, chlorite is the only ferro-magnesium mineral in the rock. Second, chlorite is a secondary mineral and has overgrown prior ferro-magnesium minerals, and therefore has a similar magnesium to iron ratio as that for the initial bulk rock composition.
The results of the comparison of chlorite's spectral features and its mineral composition is shown in Figure 4.4. It was hypothesized that a similar trend to the one from Figure 4.2, with a decrease in absorption wavelength with an increase of the magnesium number, would be observed, because the magnesium number of chlorite relates to the bulk rock magnesium number. This hypothesis is supported by the results from Figure 4.4. The Mg-OH absorption feature near 2350 nm shows the highest correlation, that is why it is used for the other plots in this study. One of the samples selected for the EMP measurements mainly contains amphibole minerals, and is marked with the text “Amph” in Figure 4.4. This sample will be discussed later in this section.

For the calculations of the magnesium number in Figure 4.4, it was assumed that the octahedral sites of chlorite are occupied by either magnesium or iron. However, there are 10 different end-members of the chlorite group recognized as named minerals in the official classification published by the International Mineralogical Association Commission on Minerals and Mineral Names [81]. Chamosite and clinochlore, respectively, are the iron and magnesium end-members [28]. Figure 4.5 shows the relation between the Fe and Mg

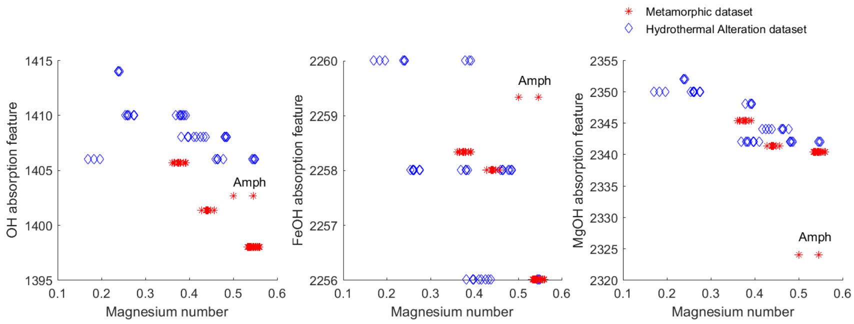

Figure 4.4 Comparison of the absorption wavelengths (y-axis) of chlorite specific absorption features and the magnesium number of chlorite (x-axis). (a) -OH absorption feature; (b) Fe-OH absorption feature; (c) Mg-OH absorption feature. “Amph” highlights measurements of the sample metamorphosed in the amphibolite facies.

cations in chlorite. Both groups of data show a linear correlation between the magnesium and iron cation concentration, where the hydrothermal altered rocks plot closer to the origin than the metamorphic rocks. According to published data, which is supported by our measurements, this is because these hydrothermal altered chlorites have more octahedral aluminum compared to the metamorphic chlorites [28]. Cation calculations show that iron and magnesium are the most dominant elements in the octahedral sheet which results in vibrations which can be observed in the NIR spectrum.

The plots shown as Figure 4.6 were used to compare the rock composition of both datasets and test the hypothesis made for this analysis. The first hypothesis is that both groups of basalts are the same and therefore can be compared. The second hypothesis addresses the difference between both datasets, and whether one group is indeed altered by hydrothermal alteration and the other by low-grade metamorphism.

Figure 4.6a is a so-called alteration-boxplot first described by Large et al. [63]. The solid line box shows where non-altered samples should appear on the plot. The more felsic the volcanic rocks, the lower the CCPI. Other than some outliers the data from the metamorphic datasets cluster on top of the non-alteration box. Clustering of the hydrothermal alteration dataset is in the upper-right corner where chlorite–pyrite alteration products are expected [63].
Figure 4.6b is a Winchester plot with two ratios of incompatible elements. The rocks plot around the same Zr/TiO2 ratio, which was reported by Winchester and Floyd [109] as sub-alkaline basalt to andesitic rocks. Some variation can be found in the Nb/Y ratio at which

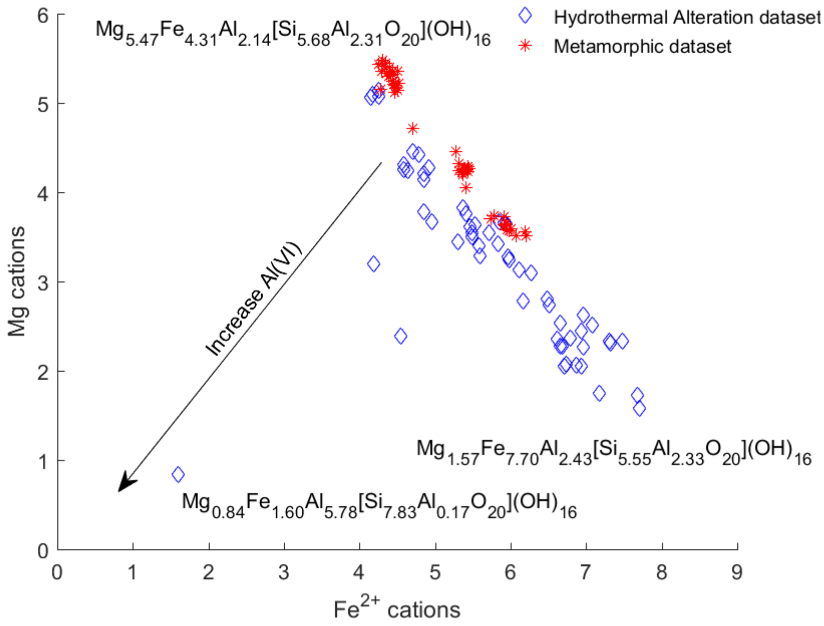

Figure 4.5 Calculated cation contributions of iron and magnesium in the octahedral sites of chlorite. More octahedral aluminum (Al(VI) in the figure) results in less magnesium, and iron and therefore plots closer to the origin. Chemical formula's presents the composition of the most Fe- and most Mg-rich chlorite measured, and the outlier containing more octahedral aluminum.

samples from the metamorphic dataset have a lower ratio compared to the hydrothermal alteration dataset.
The AFM-diagram (Figure 4.6c) shows that the basalts from the metamorphic dataset cluster where the proportion of the alkaline elements Na2O and K2O is lower than 20%. However, the hydrothermal alteration data shows more variation in the alkaline elements relative to Fe and Mg.

4.5 Discussion

Our results show that there is a significant difference between the Mg-OH absorption wavelengths of hydrothermal and metamorphic rocks. Earlier studies [30] concluded that the absorption wavelengths of chlorite are dependent on the magnesium number of chlorite. A similar trend was observed in our samples where the Mg-OH absorption wavelength, from all chlorite-specific absorption features, shows the highest inverse correlation with the mag-

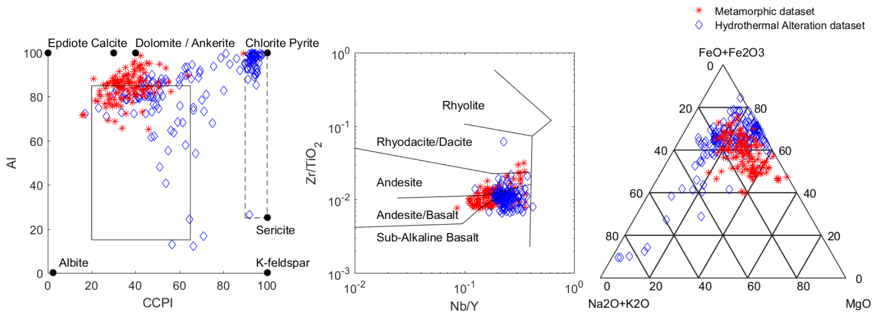

Figure 4.6 (a) Alteration boxplot plotting the CCPI against AI. Solid line box indicates the area where non-altered samples are expected to plot, dashed box indicates the area where samples altered by chlorite–sericite alteration are expected to plot. Dots represent the area's where some minerals would plot. (b) Winchester plot of incompatible elements; (c) AFM-diagram of bulk rock element concentrations.

nesium number of chlorite. Therefore, based on the higher absorption wavelengths for the hydrothermal dataset, we conclude that chlorites from the hydrothermal dataset are richer in iron than those from the metamorphic dataset.

The Mg-OH absorption feature was also compared with temperature estimates from Brauhart et al. [11]. As can be seen in Figure 4.7, the absorption wavelength shows, other than two outliers, a weak negative correlation with temperature. Based on these results we suggest that the hydrothermal chlorites formed at lower temperatures than the chlorites from the metamorphic dataset. However, this cannot be tested as temperature estimates are not available for the metamorphic dataset. Three theories to explain the difference between the two groups of basalts, and the relation between the Mg-OH absorption wavelength, are discussed below.

4.5.1 Precursor Bulk Rock Composition

Although the lithologies used in both datasets are the same, the basalts may have had differences in their initial bulk rock composition. This is one possible explanation for the observed difference in absorption wavelengths between chlorites from the two groups. If this was the case, it would suggest that the protolith of the metamorphic rocks was richer in Mg than the hydrothermal rocks. This could have been caused by differences in magma source, or crystallization in a different magma series. Based on the Winchester plot of incompatible elements (Figure 4.6b), we conclude that the initial composition of the basalts of both datasets was similar. The clustering of both basalts in the AFM-diagram in Figure 4.6c supports the rock

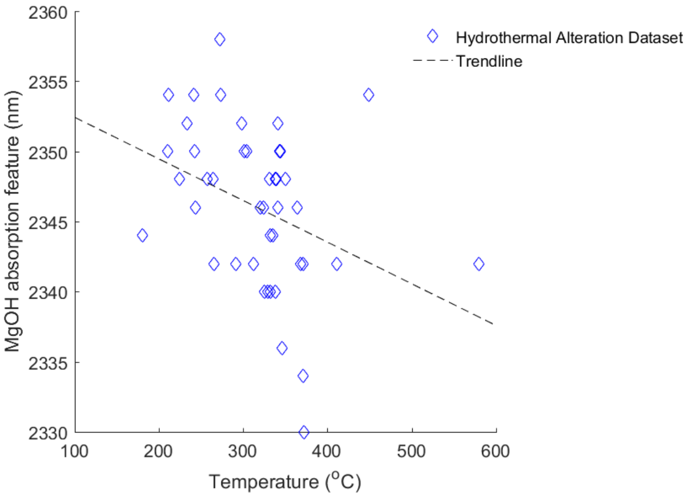

Figure 4.7 Comparison of the absorption wavelength of the Mg-OH absorption feature against the temperature of the hydrothermal altered dataset as calculated by Brauhart et al. [11].

descriptions of Smithies et al. and Brauhart [94, 12] that the volcanic rocks were formed from the tholeiitic magma series [52]. However, the hydrothermal dataset shows a larger scattering towards the alkali corner. This suggests that a process other than magmatic crystallization was involved, which resulted in the current rock compositions. This is supported by the alteration boxplot on Figure 4.6 in which the chlorite–carbonate–pyrite index differentiates the hydrothermal rocks from the metamorphic rocks.

4.5.2 Temperature

Although there are no independent temperature estimates for the metamorphic dataset, the metamorphic facies in which the rocks were formed have a similar temperature range to that reported by Brauhart et al. [11] for the hydrothermal dataset. Literature shows that depending on the pressure, the temperature of peak metamorphism under greenschist and amphibolite facies ranges between circa 350–750 °C [83]. Based on these observations, it is expected that chlorites formed at amphibolite facies (at higher temperatures) will have lower absorption wavelengths than those in greenschist facies rocks. This coincides with the observations of Abweny et al. [1], who concluded that amphibolite facies rocks can be distinguished from greenschist facies rocks because the latter have a lower absorption wavelength near 2350 nm. Doublier et al. [30] concluded that spectral features of chlorite could be used to differentiate low-grade metamorphic grades. Furthermore, the use of compositional or structural changes in chlorite as a response to changing temperature has been discussed in several previous studies [27, 108, 34, 92, 20] The investigation of EMP measurements in the metamorphic rocks made it possible to test the influence of spectral features of amphibole on the relation between the spectral features of chlorite and its magnesium number. One rock, used for the EMP analysis, contains a mixture of amphibole and chlorite minerals. Figure 4.4 shows that this sample fits the linear trends of both the -OH and Fe-OH absorption feature but is a clear outlier for the Mg-OH absorption feature (Figure 4.4). A comparison of chlorite reflection spectra both with and without the presence of amphibole (4.8) shows that only the Mg-OH absorption feature displays any spectral difference. This coincides with the observation resulting from the EMP measurement. Therefore, it is thought that amphibole minerals, which share the Mg-OH absorption feature with chlorite, cause the difference in absorption wavelengths between the two metamorphic facies. If either the mineral composition or the temperature influenced the difference, then the amphibolite facies rocks would be expected to be outliers in all the absorption features and not only for the Mg-OH absorption feature.

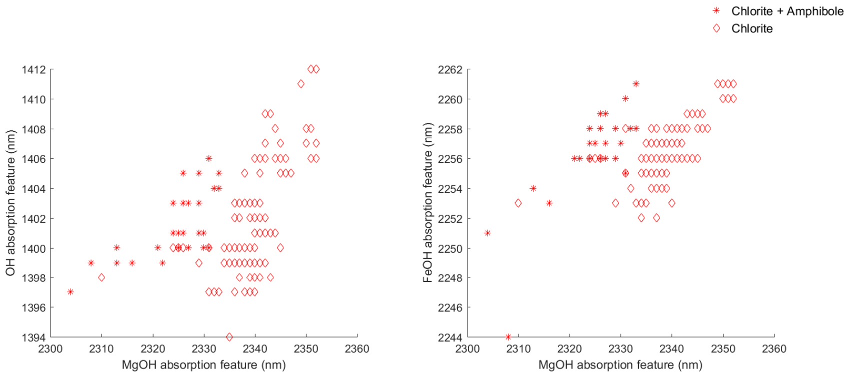

Figure 4.8 Comparison of the characteristic absorption features of chlorite and the influence of amphibole minerals. (a) Mg-OH absorption wavelength against the -OH absorption wavelength (b) Mg-OH absorption wavelength against Fe-OH absorption wavelength.

4.5.3 Metasomatism

Another process that can explain the difference in absorption wavelengths between the two basalt groups is the difference in mass transfer. In a previous section, that discussed the influence of the precursor bulk rock composition, it was mentioned that there are differences in element concentration between the two datasets. Figure 4.3 shows that the magnesium number of chlorite and the bulk rock composition are related. Brauhart et al. [14] showed that mass-transfer of major elements resulted from hydrothermal circulation. Figure 4.6a,c support these observations because the data from the hydrothermal dataset plots outside the area where non-altered data are expected. In the ternary diagram, the data for the hydrothermal dataset is dispersed whereas the basalts of the metamorphic dataset cluster together in one corner. Brauhart [12] also described variations of the magnesium number of chlorite and found that there is a difference between the magnesium number of chlorite in the ground mass and larger chlorites associated with other ferromagnesian phases.

In the same study, Brauhart [12] concluded that the larger chlorite crystals did not reach equilibrium with the hydrothermal fluid, which resulted in differences in magnesium numbers inside the rocks. So, the influence of precursor lithologies was excluded based on the observations. For the metamorphic dataset there are no indicators that the element concentrations had changed from the precursor composition. An interaction between temperature and metasomatism is likely, although it was not specifically mentioned by Brauhart and co-workers [11, 14].

The difference between mass transfer in the hydrothermal rocks and no mass transfer shown in the metamorphic dataset seems the most likely explanation for the observed spectral differences. However, it is possible that temperature and mass transfer are related to each other in the hydrothermal dataset. This is difficult to conclude from the spectral data, because these describe ratios rather than absolute element concentrations. It was emphasized by Cathelineau [20] that various geological processes and variables can influence the chlorite composition. Not all of these can be studied here because of the data availability.

The results show that the Mg-OH absorption wavelength is defined by the magnesium number of both chlorite and the bulk rock. The absorption wavelength also shows a relationship with alteration temperature. This suggests that the alteration temperature and magnesium number of chlorite and bulk rock are correlated. Since the variation in magnesium number is caused by metasomatic processes, it is likely that alteration temperature and type and degree of metasomatism are related, where more intense metasomatism occurs at higher temperatures. This relationship was not addressed by Brauhart and co-workers [11, 14], and should therefore be studied in more detail to with more data to test this hypothesis.

Although there were spectral differences between the metamorphic facies of the rocks, it seems more likely that this was strongly influenced by the presence of amphibole minerals, and less by the composition of chlorite. Zane et al. [113] attempted to use the composition of chlorite as an indicator for the metamorphic grade, but concluded that the composition of chlorite was instead defined by bulk rock composition. Results of this study will be applicable to greenstone belts in other areas if: (i) the precursor of the metamorphic rocks are of a similar basaltic composition; and (ii) the type and intensity of metasomatism of chlorite–quartz alteration zones of the hydrothermally altered rocks are similar to those identified in this study.

4.6 Conclusion

Studying the Mg-OH absorption wavelength in chlorite was found effective to distinguish between the Mars analogue basalts altered by low-grade metamorphism from basalts altered in a hydrothermal alteration system in the Pilbara Craton, Western Australia. The absorption wavelength shows a strong correlation with the magnesium number of chlorite, which was closely correlated to the bulk rock composition. Metasomatism has altered the bulk rock composition and the composition of chlorite in the hydrothermal system. Based on these results, there is no indication of changes in mineral or bulk rock composition that can be attributed to metamorphism. Observed changes in the reflection spectra between the greenschist and amphibolite rocks seem to have been caused by a shared absorption feature of amphiboles and chlorite. The difference between metasomatism in the hydrothermal system, and no changes in precursor rock composition for the metamorphic dataset, seems to be the most probable explanation for the observed spectral differences. Temperature also showed some relation with the Mg-OH absorption wavelength for the hydrothermal dataset but it is thought that this might also be related to the degree of metasomatism. We concluded that the Mg-OH absorption wavelength of chlorite near 2350 nm can be used to differentiate between metamorphic chlorites and hydrothermal chlorite that were formed by intense metasomatism. The similarity in age and lithology between the basalts on Mars and those from the Pilbara Craton indicates the potential of this study for planetary exploration. With a similar approach using wavelength mapping of the 2350 nm of chlorite absorption features within the OMEGA or CRISM images might explain the alteration process related to the presence of phyllosilicate minerals on the surface of Mars.

Modelling surface geochemistry [*]

5

5.1 Introduction

Gamma-ray remote sensed element maps present crucial information to assess the surface geology of Mars. From gamma-ray spectrometer (GRS) measured gamma-ray and neutron fluxes, global maps are produced for the elements K, Th, Fe, Cl, H (expressed as equivalent H_2O), Si, Ca, Al, S. Several hypotheses have been proposed to explain the distribution of these elements including volcanism, aqueous weathering and the dust coverage [57, 10, 36, 47]. The resolution of the element maps, which ranges between 200-500 km/pixel, complicates comparisons with other global mineralogical or geomorphological datasets, in turn challenging interpretations of possible geological processes that influence element distributions.
Hypothetically, when similar geological processes underlie both element and mineral distributions, a spatial correspondence between both is expected. In addition, the elements detected by GRS are key to crystallographic structures of many common minerals on Mars and so you would expect correspondence between mineral and element maps, though differences in methodology from GRS to optical methods complicate this correspondence. These notions have motivated many comparisons between GRS data and infrared spectral observations as a method connect low-resolution chemical data with higher-resolution mineralogical data. Previous data-integration studies between infrared data and gamma-ray geochemistry information include Rogers and Hamilton [87] and Viviano et al. [105]. These studies focus on the geochemical variance between mineralogically defined surface types based on the thermal emission spectrometer (TES) data [87], and the mineralogical variance of the crust underlying the dust in the Tharsis region [105].
In this study, we propose a statistical approach to model the global

---

[*] This chapter is based on: Kamps, O. M., Hood, D.R., Hewson, R. D., van Ruitenbeek, F. J. A., Karunatillake, S., Viviano, C.E. van der Meer, F. D. (in preparation) Modelling GRS chemical maps of Mars with CRISM Multispectral Summary Product Maps. Icarus

element distribution based on mineralogical data, without asserting focus on any specific regions. The global summary product maps from Kamps et al. [56] are used as input for the mineralogical data. That dataset contains the calculated summary products of Viviano-Beck et al. [106] on the CRISM (Compact Reconnaissance Imaging Spectrometer) multispectral mapping mode dataset [74]. The products describe reflectance values, spectral slopes, absorption features and spectral indices, and are developed to capture the spectral variance in the CRISM data [106].

In this study, a novel approach of multivariate linear regression is proposed to examine how well the CRISM summary products can model the element concentrations measured with the GRS instrument. The benefit of the models used here is that they do not require prior assumptions to test for relations (i.e., unsupervised correspondence), minimizing interpretive bias. The output of such models highlights the spectral parameters that are most significant in modelling the element distribution and can be interpreted for the geological processes related to the individual element distributions. The effectiveness of the models is also evaluated for the geochemical provinces of Gasnault et al. [36], the Medusae Fossae formation [79], and the dust-covered regions [88].

5.2 Methods

The methodology applied in this study consists of several consecutive processes of (1) data preparation (2) modelling (3) accuracy analysis and (4) defining important variables for each model. The processes are summarized as a flow-chart in Figure 5.1 and further explained in the following sections.

5.2.1 Datasets

Comparing CRISM and GRS data is difficult because of the substantial differences in modes of measuring. The element concentrations are modelled based on the measured peaks of gamma-photon energy spectra using the gamma-ray spectrometer instrument on the Mars Odyssey mission. Gamma photon energies are functions of elemental decay process, as well as nuclear emission because of neutron scatter or capture, generating compositionally diagnostic spectral features. For this instrument, the measured gamma-rays can originate from up to 1 m depth [10], making the observed chemistry an average of the near-surface. The instrument does not have a collimator and therefore produces limb-to-limb cumulative spectra with some collimation from the Martian atmosphere. Accordingly, about 50 % of the cumulative spectrum of gamma photons comes within

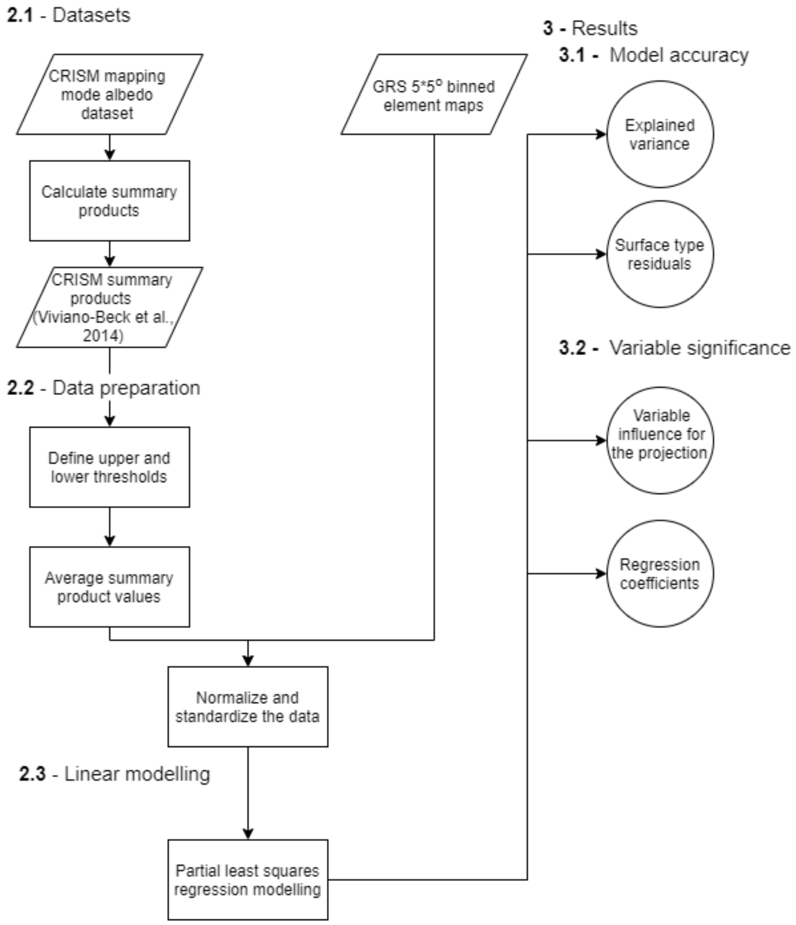

Figure 5.1 Flow-chart diagram of the consecutive steps in our method and the produced results. Bold numbers indicate the sections in this paper in which the topic is addressed.

a radius of 240 km from nadir, varying with peak energies. Consequently, the spectra are processed into element maps, modelled in a region of interest of 2*2o or 5*5o cylindrical grids.

The mineralogical information comes from the CRISM instrument, which orbits Mars on the Mars Reconnaissance Orbiter (MRO). CRISM is an imaging spectrometer which measures visible and infrared light in the wavelength range from 0.4-4 μm. That wavelength range restricts sensitivity to the surface of the planet, shallower than a few tens of micron depths. For global-scale studies, the CRISM instrument has a mapping mode with a spatial resolution of 200 m/pix, 72 band multispectral resolution, and 80% surface coverage. Summary products are calculated for this dataset which describe spectral

features such as band depth, reflectance, slopes, peaks, or reflection indices. Each of these products is intended to describe a specific mineralogy or surface characteristic. The first version of 33 summary products was developed by Pelkey et al. [82], and later revised by Viviano-Beck et al. [106].
The spectral summary products of Viviano-Beck et al. [106] are evaluated for global geological analysis in Kamps et al. [56] (see Appendix Appendix Table 1). In the 2020 study it was found that the global distributions of the primary minerals olivine and pyroxene are well described by their respective summary products OLINDEX and LCPINDEX, HCPINDEX and BD920. However, the spectral features of secondary minerals such as sulfate, carbonate, phyllosilicates overlap and more geological information, or spectral feature combinations are required to confirm for decisive mineralogy. Kamps et al. [56] group and name those as secondary mineral summary products.

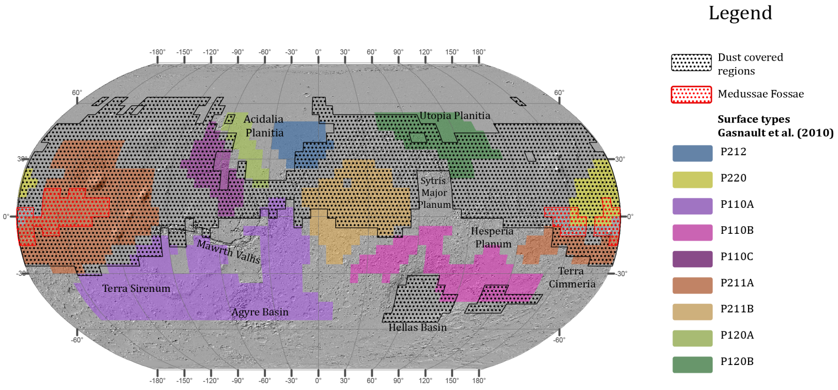

Figure 5.2 Global map of Mars presenting the geochemical provinces of Gasnault et al. [36], GRS-pixels covering Medusae Fossae Formation [79], and GRS-pixels with a dust-coverage index (DCI)<0.96 [88]

5.2.2 Data preparation

The chemical maps are mostly restricted to specific latitudes (55^oS to 45^oN) and all these pixels are considered for the modelling. The maps of potassium and thorium have a coverage up to 65^o latitude, and these extra pixels are included in their analyses.
Because of the difference in lateral spatial resolution between the datasets, some data preparation is required. The difference in spatial resolution is addressed by averaging the summary product values of all CRISM pixels within the 5 by 5 binned GRS pixel. The global maps of the CRISM summary products maps at both the original resolution and the averaged gamma-ray pixel resolution are

attached as a dataset in the supplementary material (Data Set S3.1 and S3.2).

As a result of the calculation of CRISM summary products, the maps of summary products have some anomalous pixel values: extreme values for the summary products which deviate significantly from surrounding pixels. Therefore, for each summary product, upper and lower thresholds are calculated for each summary product based on the global map and are used to mask unlikely pixel values. The minimum and maximum of threshold values are based on the quartile distances where the minimum is 1.5 times the inter-quartile distance (IQD) below the first quartile, and the maximum is 1.5*IQD above Q3. For all products related to spectral band depths, the minimum data values are set to zero. Just like the study of Kamps et al. [56] the summary products that are thought to be affected more by the atmosphere conditions rather than the surface composition, are discarded. The effect of the atmosphere thickness on the summary products is tested with a Pearson's correlation coefficient with the MOLA digital elevation, which is assumed to be inversely related with the atmosphere thickness. The summary products with a correlation coefficient, $r < -0.6$ or $r > 0.6$, with the MOLA digital elevation, are taken out from the analysis. This applies for the products: BD1400, BD1435, BD1900R2, D2200, BD2355, ICER2, and BD3000, and are also mentioned as separate category in Appendix Table 1. While this threshold certainly removes the summary products most strongly related to atmospheric thickness, some remaining parameters inevitably have correlation coefficients close to this threshold, and should be interpreted cautiously. For example the product BD31002 versus digital elevation with a correlation coefficient of -0.58, where some effect of the atmosphere cannot be excluded.

Some averaged grid pixels have no-data values. These are mainly the pixels around Hellas Basin which have no spectral data for the wavelengths larger than 3μm. All products using the reflectance in this wavelength range have no-data values (BD3000, BD3100, BD3200, BD3400, CINDEX). In these cases, the pixel values with no-data values for these products are manually set to zero such that these can still be included in the modelling.

No processing is possible to deal with the difference in measuring the sensing depth of both datasets as described in Section 5.2.1. Here, we will refer to the depth sensitivity limit of the gamma-ray spectrometer as the subsurface (1 m depth). This difference between the measuring depths leads to a key simplification when both datasets are compared, namely that the subsurface is homogeneous. However, such simplifications have proven useful in prior works as well, including constraints on Mars's geothermal flux. [38]

5.2.3 Linear Modelling

To develop a model that connects CRISM summary parameters to element concentration on Mars we apply the Partial Least Squares Regression (PLSR) method [110]. This modelling technique is favored over other multivariate regressions techniques because it can handle covariance in predictor variables (i.e. CRISM summary products data), which is apparent in our dataset according to the correlation matrix by Kamps et al. [56]. For each element the modelling is done with and without the dust-covered pixels to test the influence of dust-covered areas on the models because the model assumption of subsurface homogeneity is most challenged in these areas. The dust-covered pixels are considered to be the pixels which have an average dust-coverage index (DCI) [88] less than 0.96 (see Figure 5.2).

PLSR has similar principles as principal component analysis (PCA) where the number of axes is reduced by creating so-called principal components. In PCA these axes describe the most variance in the data, for PLSR these principal components are rotated such that they have the most covariance with the response variable (i.e. the element concentration).

The modelling is done in MATLAB using the libPLS toolbox [64]. This toolbox makes use of the PLS NIPALS (Non-linear Iterative PArtial Least Squares) algorithm to calculate the score and loadings of the PLS-model. For each element, we use 70 % of the GRS-pixels to develop the PLSR model (calibration). The 30 % that is not considered is used to test the accuracy of the model dataset (validation). This process is repeated a thousand times, in a so-called Monte-Carlo simulation. In each repetition, a new calibration and validation subsets of the data are selected randomly. The Monte-Carlo simulations ensure that models are not biased due to initial calibration and validation dataset selection and provide estimates of model variability. All parameters presented in the Results section, such as the VIP-values and regression-coefficients, are averaged over all these simulations.

The model gives various outputs which we can use to consider how well the CRISM and GRS data relate to each other and how much each summary product contributes to the model. The accuracy of the model is indicated here by the explained variance of the response variable. To test which summary products have the highest contribution to the model, the VIP (variable influence for the projection) values are used. The VIP indicates how much variance the input variable (i.e. summary product) describes in the variable and predicted dataset. The VIP-values are calculated with a weighted sum of squares of the PLS-weights. The weights are based on the explained variance for each PLS-component and the average VIP-score for all variables is 1. Therefore, the variables with a VIP-score larger than one, are considered as important for the model

[110]. The regression coefficients from the linear model are used to test whether the summary product has a positive or negative effect on the model. Both the individual element distributions and the geochemical provinces are studied here in relation to the CRISM data.

5.3 Results

Our modeling tests how well the infrared spectral information relates to the element concentrations and which summary products have the most effect on such a model. Both objectives are discussed in the following sections. Two models are made for each element (with or without dust-covered regions), making eighteen models in total. Below, we discuss the general results and more detailed results that are of immediate interest for the conclusions. Results of all the other models can be found attached as supplementary material.

5.3.1 Model accuracies

The accuracy of each element model is evaluated here in three ways, namely as the explained variance (Figure 5.3), comparison of global maps (Figure 5.4), and a comparison of model and GRS data with median values for the chemical provinces by Gasnault et al. [36] (Figure 5.5).

Figure 5.3 presents the explained variances for each model of the surface chemistry. The explained variance is a statistical measure expressed as a percentage to indicate the accuracy of the model. A hundred percent explained variance for a model means here that the geochemical concentration predicted by the model, using the summary products as input variables, is exactly the concentration measured by the gamma-ray instrument. The lower the explained variance, the less variance of the original input data is predicted well by the model. In Figure 5.5 a high explained variance would show that all pixel values align linearly. In the global maps of a model with higher explained variance, the result should be the increased similarity between the original and modelled maps (Figure 5.4).

In general, the explained variance for the various geochemical models is between 30-50%, and dust-free models (white bars) are generally better than models that include the dust-covered pixels (grey bars). Notably, the volatile elements H_2O and S have comparable dust-free and dust-included models, while the models for Cl and Si are improved when dust-covered pixels are included. The effect of excluding the dust-covered pixels is most noticeable for the elements Fe, K and Th where the explained variance is significantly higher compared with the model that includes these pixels. Of all models, the model for Fe without dust-covered pixels has the highest explained variance of 60%. By contrast, the model for Ca is the poorest model both with and without the dust-covered pixels. These explained variances are those included within the validation subset, and consists of the thirty percent of the data that are not used to calibrate the model. The error-bars present the standard deviations of the thousand Monte-Carlo simulations where the calibration and validation data were randomly selected. The original chemical map, together with the model and its residuals, are presented as global maps, to give a spatial impression of the variance explained by the models. In Figure 5.4 the elements Si and H_2O are used as examples because their spatial variance is described in more detail in the Discussion section. The maps for the other element models are included as supplementary material (S1.1 - S1.18).

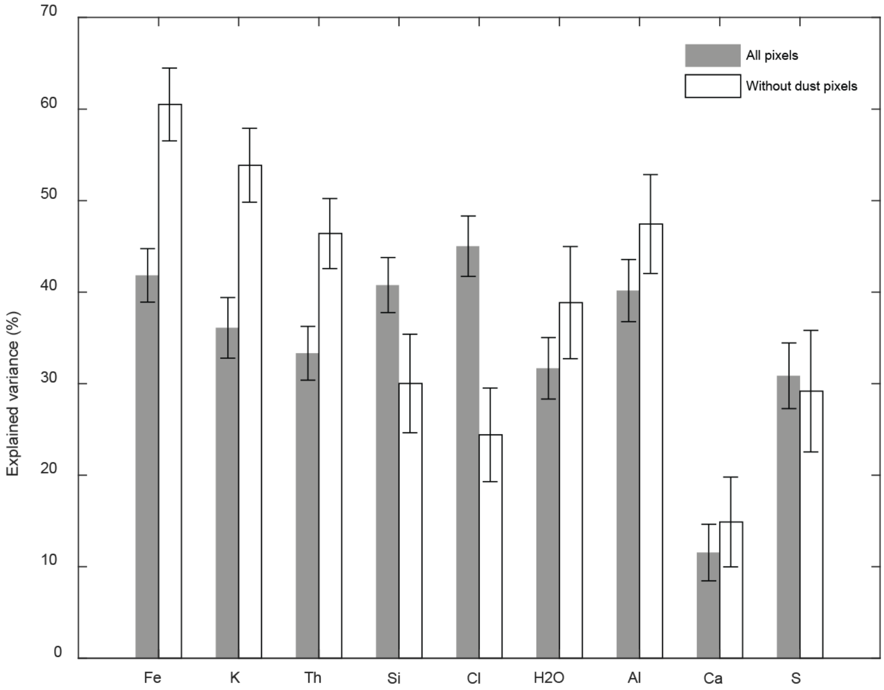

Figure 5.3 Explained variance for each of the elements according to the PLSR modelling. Solid bars indicate the explained variance where all GRS-pixels are considered, outlines where dust-covered (DCI<0.96) pixels are excluded.

The white lines present the outlines of some of the polygons in Figure 5.2. High dust-regions are outlined in the Si map, as Si is later discussed in relation with the dust-coverage. The maps for H_2O present the outline of the Medusae Fossae formation due to its remarkable enrichment in the other volatile elements, S and Cl. For Si, Figure 5.4 shows that except for some local enrichments, the general variance of this element is well explained, this is also reinforced by Figure

5.5. The model for H_2O seems to generally under predict most of the values. In particular, the enriched region in the center of the map is not predicted well by our model, which is indicated by high residual values.

Figure 5.5 summarizes the accuracy of the model for the geochemically distinct GRS provinces, where the median concentration of the surface type in the original dataset and the model are presented. The geochemical provinces are included in Figure 5.5 for spatial context of the linear trend between the original and modelled pixel values, and to examine the accuracy of our models in well-established geochemical provinces. The red dashed line in Figure 5.5 indicates the identity-line. The further away from the identity line the median of the province plots, the less accurate the model is for that province. The blue dashed line is the linear regression: a perfect model would

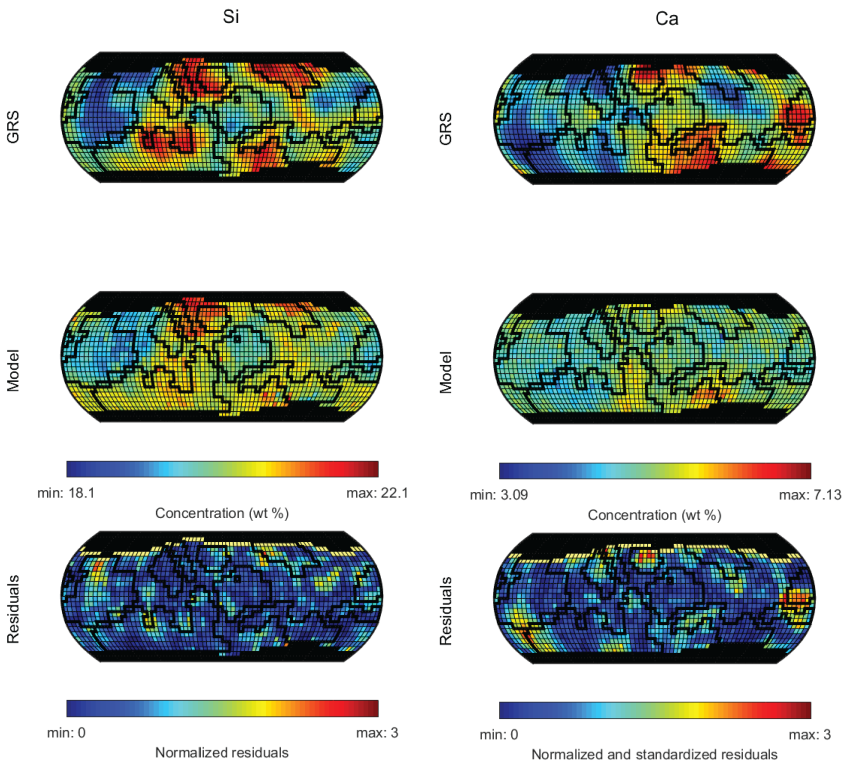

Figure 5.4 Original, modelled, and residuals for Si and Cl. GRS and modelled data are in weight percentage. Residuals are the normalized residual values. The white outline for Si presents the dust-covered regions, and for H_2O the Medusae Fossae formation. These outlines are the same as the polygons in Figure 5.2.

have both lines overlapping. For all models the blue line plots flatter than the identity-line, which means that all models are under predicting deviations from the mean. With this figure it becomes clear which provinces are well-explained with the model. For example, for Fe, the enrichment of geochemical province P220 near Elysium is not well explained by the model. The low quality of the model for Ca becomes apparent here since the regression line (blue line) is close to horizontal.

5.3.2 Effect of summary products on models

Figure 5.6 shows the summary products with VIP-values larger than one for most models. The values of the model for Ca are not presented because earlier results have shown that the model does not explain much variance of the element distribution. Because the models for Fe, K, and Th are significantly better when dust-covered pixels are excluded, the VIP-results of these models are presented in Figure 5.6, indicated by the grey boxes. For the other elements the VIP-values of the models including all pixels are presented. The VIP-values and regression coefficients of all models, including Ca, and those with and without dust-covered pixels, are included in the supplementary material (S2.1 and S2.2). These products are ordered from high to low based on their VIP values (blue bars) and the red plus-symbols present the regression coefficients (i.e. positive or negative relationship). Descriptions of the mentioned summary products can be found in Appendix Table 1.

For each element, the distribution of VIP values varies. The elements Cl, H_2O and S have individual variables that stand out with noticeably higher VIP-values in comparison with the other variables. However, for the element Al, most variables have similar VIP-values with no single variable that has significantly more importance for the model relative to the others.

5.4 Discussion

The results of multi-variate modelling show that for most of the elements the general trend of the element concentrations are well predicted by the CRISM summary products. The accuracy of such a linear model, however, varies for the different elements. When all pixels are included in the model (grey bars in Figure 5.3), most models have an explained variance between 30-50 %. Both the global maps (Figure 5.4) and the chemical province plots (Figure 5.5) have proven to be useful to assess the spatial locations where the variance is well explained, and where the model lacks accuracy. In the following sections we focus on specific regions and discuss these in relation to

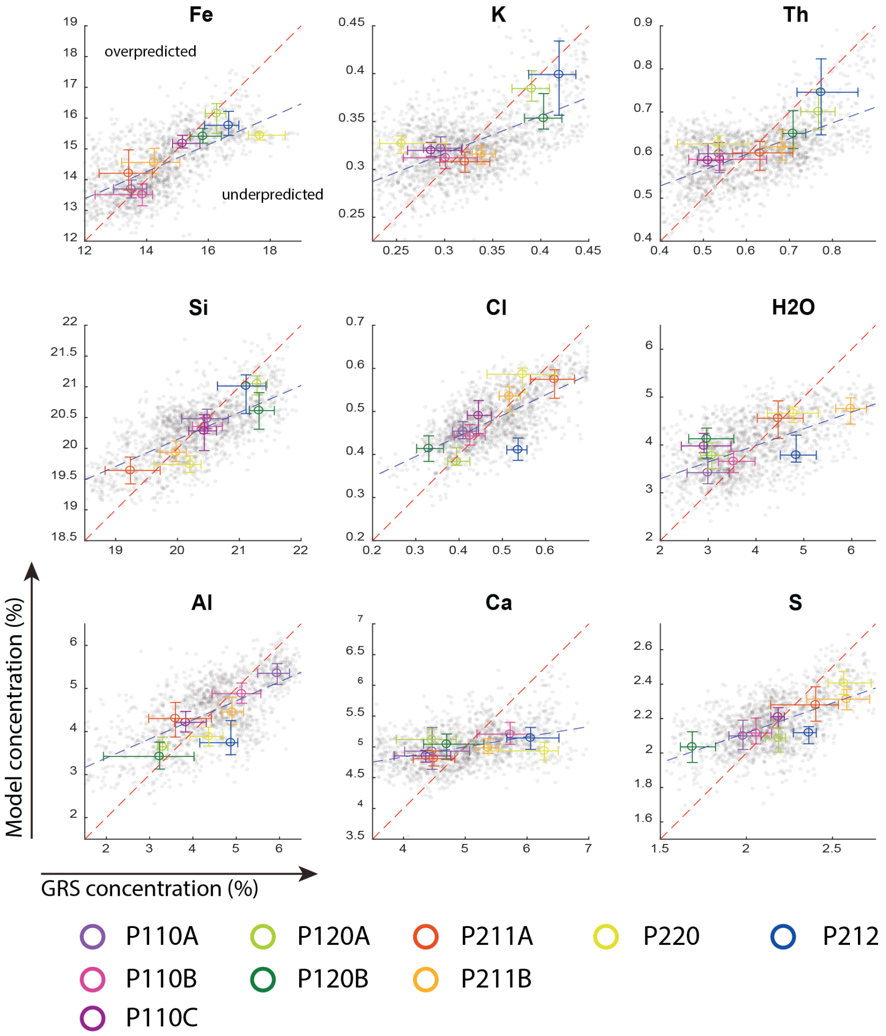

Figure 5.5 For each element the original (horizontal) and modelled (vertical) median values of the various chemical provinces defined by Gasnault et al. [36]. The red dashed line indicates the identity line, the blue the regression line through all the data values.

the summary products that had significant influence on explaining the variance. The summary products are interpreted for the geology of that region.

5.4.1 Low accuracy in the calcium model

One of the benefits of the modelling results presented is that the low accuracy models can also be interpreted. Figure 5.3 shows that the

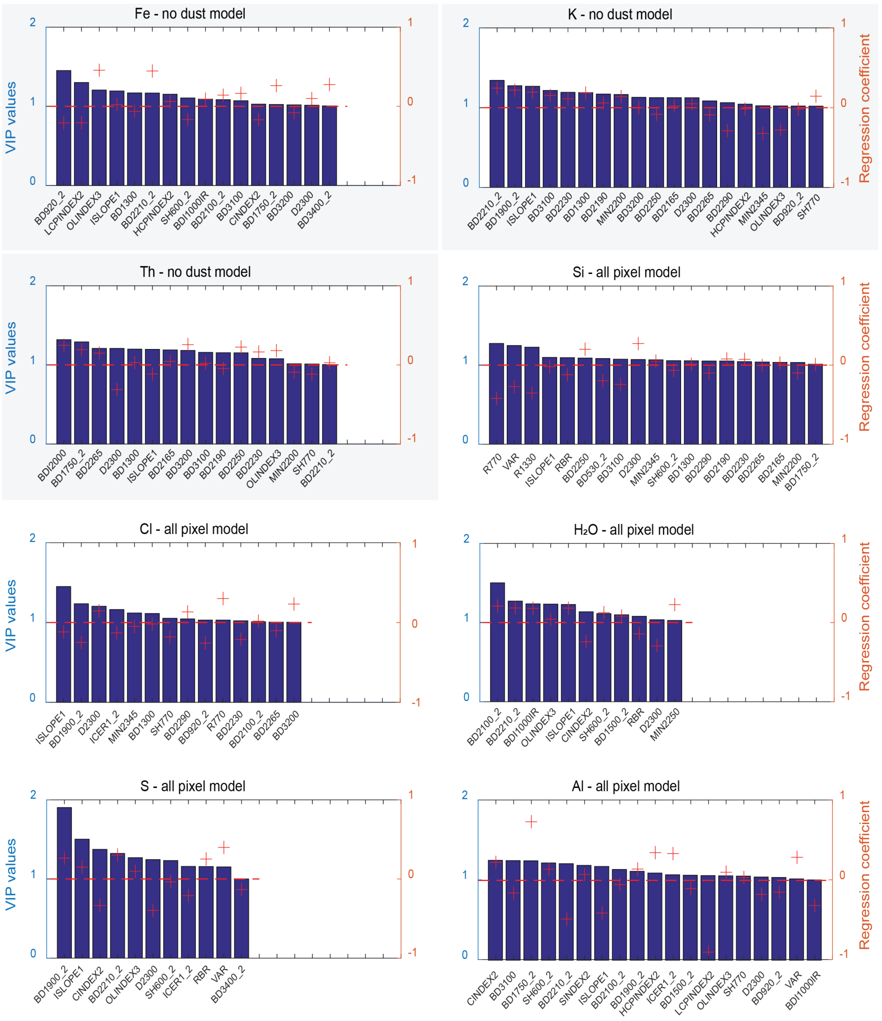

Figure 5.6 Summary products with VIP values > 1 ordered based on the VIP values. For each element the most accurate model is chosen which means the model without dust-covered pixels for the elements Fe, K, Th, (grey box) and with all pixels for all other elements. VIP values (blue bars) and regression coefficients (red plus sign).

model for calcium with 11% explained variance is the least accurate compared to the models of other elements. This is also apparent in Figure 5.5 where the median model values of the geochemical provinces are all similar. This low accuracy can be explained in two possible ways. One possibility is that the variance of calcium is related to a mineralogy which cannot be observed by CRISM. Feldspar minerals are one of the major components of the basaltic rocks on Mars which cannot be detected in the CRISM wavelength range. Because the concentration of calcium is relatively high (4-7 wt %), it is considered as a prominent element for Mars. A global study of feldspar by Milam et al. [71] concluded that the feldspars on Mars are chemically homogenous, and can be classified as labradorite and bytownite, which are both calcium-rich (>An 50) feldspars. What can be concluded based on the results presented here is that the variance of calcium is not well explained by the distribution of pyroxenes, nor secondary minerals such as carbonates, sulfates or phyllosilicates at the surface of Mars. Another possibility is that calcium is more vertically heterogeneous compared to the other elements such that the disparity between CRISM measurements and GRS measurements is larger for Ca than for the other elements. While it is likely that vertical heterogeneity plays a role in limiting the modelling capabilities for all elements, it is unclear why calcium would have greater heterogeneity than the other elements. Further investigation of the distribution of the calcium-rich minerals in the subsurface remains work for future study.

5.4.2 Effect of dust

The gamma-ray data are often discussed in relation to the dust-coverage, often referred as dust mantling in literature [58, 98, 46]. With the PLS modelling we evaluate the effect of the dust by studying the models with and without the dust-covered pixels, and by studying the VIP values for the dust covered summary products for each model.

Of all elements the Si concentration shows the strongest relationship with the dust-related summary parameters. The summary products that have the most effect on the model for silicon (i.e. highest VIP-values in Figure 5.6) are R770, R1330 and VAR. For each of those products the global variance is mostly influenced by the dust-coverage [56]. The model over-predicts the Si concentration for the geochemical province covering the Tharsis region (P211A) (see Figure 5.5). This region is studied in detail by [105], where they suggested that this region has a low Si content due to the dust thickness and that the surface composition of the bedrock was not unusually Si depleted. They concluded based on the findings of Harmon et al. [42], that the composition of the rocks below the dust around Tharsis has a similar composition of other Hesperian units on Mars. Although the dust thickness cannot be evaluated based on the summary product values, the significant influence of these summary products on the Si model would argue that Si-depletion due to dust cover may be an important global influence of observed Si abundance.

The model for Cl (Figure 5.3) is also unique in that it is substantially improved when the dust-covered pixels are included, rising from circa 25% to 45%. Despite this increase in model performance, the highest VIP summary parameters in the Cl model are not dust-related (ISLOPE 1, D2300, BD19002) though, R770 does have a VIP>1 (Figure 5.6). This may indicate a correlation of Cl with dusty areas that it is not strictly related to the dust, and is instead caused by mineralogical connections with the other volatile elements, as suggested in Hood et al. [46].

5.4.3 Volatile elements and Medusae Fossae formation

The S, Cl and H_2O enrichments in the vicinity of Medusae fossae have been the topic of a number of investigations (e.g. Ojha et al. [79]). Several hypotheses have been proposed in literature to explain the compositional uniqueness of this formation with pyroclastic flow or fall, or aeolian deposition considered as viable possibilities [65]. In Figure 5.7 the model accuracy is assessed for these regions by highlighting the pixels that cover Medusae Fossae (see Figure 5.2) with red plus-signs. The models for the elements sulfur and chlorine have a good prediction of the enrichments in Medusae Fossae. For H_2O however, the enrichments cannot just be explained by the Medusae Formation. The latter is also noticeable in Figure 5.4 where not all pixels within Medusae Fossae have high H_2O concentration values.

The summary product BD19002 has a positive high effect on the models sulfur and chlorine (Figure 5.6). That product describes the 1.9 µm water feature, which can be related to either bound or unbound water [106]. The feature is most likely from either hydrated minerals (e.g. phyllosilicates, sulfates) or unbound water in either liquid or ice phase. The high impact of the spectral water feature, as well as good model prediction within the Medusae Fossae formation is here interpreted to confirm that the material in Medusae is volatile rich as suggested in Ojha et al. [79]. If this is volcanic material it could indicate that the eruptions sourced from a hydrated mantle source [2]. Unfortunately, none of the high-VIP spectral parameters are uniquely related to particular mineral features, so it is difficult to distinguish between bound and unbound H_2O in this feature.

The VIP values for the H_2O model show that BD21002 and BD22102 have the highest impact on the model. Both are common water and hydroxyl features for phyllosilicates and sulfates, implying that water is bound in a mineral structure. However, the global maps of both products show that the averaged values for each GRS-pixels are based on few, high-valued CRISM pixels, which gives these products a high uncertainty (see supplementary dataset S1). So, although the model for H_2O suggests that the enrichments are most likely related to bound water in hydrated minerals like phyllosilicates and sulfates, there is a high uncertainty in these findings. Water as ice in this region, especially in the subsurface can therefore not be excluded.

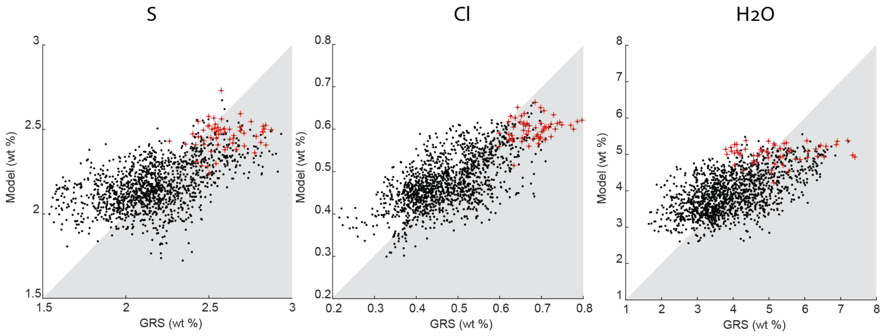

Figure 5.7 Scatter plot of the model and original element concentrations. In red the pixels overlapping with the Medusae Fossae formation are highlighted

5.4.4 Northern Lowlands

The northern lowlands are characterized by a compositional enrichment of the elements Fe, K and Th [57, 99]. However, the models show that different summary products are considered as important for the different elemental models, though there is substantial overlap in the important parameters for K and Th. This supports the findings of Karunatillake et al. [57] that the potassium and thorium generally co-vary but that iron varies independently across Mars.

The model for Fe has the highest explained variance of all models when the dust-covered pixels are not considered in the analysis (60% see Figure 5.3). The summary products with highest VIP-values are all related to the mafic mineralogy, such as the olivine and pyroxene indices, which all have low values for the northern lowlands. These lower values coincide with the extent of surface type 2 in Bandfield et al. [5], which concluded that the northern lowlands have an andesitic composition. Later studies on the chemical maps have indicated that the silicon content in this region is too low for an andesitic composition [112, 57]. There are several geological processes that can explain the inverse relation of the mafic summary products on the iron enrichment in the north. These processes include either a different magmatic origin for the rocks in the northern lowlands [5, 86], aqueous in-place alteration of the olivine and pyroxene minerals [112], or a more recent sedimentary coverage that overlays buried mafic minerals [76]. However, based on these results we cannot conclude on either of these geological processes.

The elements potassium and thorium are both enriched in north Acidalia and the summary product BD22102 has the highest VIP-value for both elements in the dust-free and dust-included models. This summary product describes the Al-OH spectral feature of phyllosilicates and sulfates [106], most of which do not incorporate

K fundamentally into their structure. The chemical distribution of potassium shows overlap with the TES-based surface type 'northern Acidalia' by Rogers et al. [85]. With the TES-instrument they have found indicators, for sulfates in this region. Rogers and Hamilton [87] compared this surface type, among others, with the chemical maps. However, because of the lack of spectral evidence and the lack of a sulfur concentration map, they could not make a strong argument of sulfates in this region. The sulfur map presented here, however, show that sulfur is slightly enriched in this area. Combining these observations, aqueous alteration can be supported as an explanation for the enrichment of K and Th rather than a difference in magmatic origin, even though K and Th do not appear to fractionate spatially. The combination of the higher values for BD22102, the TES spectral interpretation of sulfates and the slight increase of sulfur in this region could indicate the presence of sulfate minerals in this region. This would suggest acidic conditions in which the immobile elements potassium and thorium can also be mobile according to [99, 29]. These findings contrast with Karunatillake et al. [57] findings which supported a distinct magma provenance for surface type 2 as the best explanation for potassium and thorium enrichment. While no single piece of evidence for aqueous alteration is particularly robust, these small pieces of evidence warrant a more detailed site specific study.

5.4.5 Uncertainties and limitations

Although the modelling itself does not require any assumptions about the relation between the CRISM and GRS data, some assumptions in the pre-processing must be mentioned here. Here it is assumed that the dominance of a specific mineral is linearly related to the value of the summary product. However, it is known that spectral features in the shortwave infrared wavelength range are not linearly related [24]. Also, the summary product values are normalized and stretched prior to the modelling. In our model the products explaining shallow spectral absorption features have the same impact on the model as more prominent spectral features. So, the stretched summary product values quantify the spectral features, but it is difficult to interpret changes in these spectral features relative to each other. Such a stretching also makes that spectral features with little spatial variance could be stretched within the noise level of the data, possibly resulting in an overestimation of the presence of a mineralogy.

Another difficulty in the interpretation of the modelling results is that a linear correlation does not automatically imply a causation. For some models the causation is interpreted as variable A caused B, although it can easily be turned around that variable B causes A. We attribute such correlations to a common cause; e.g. mantling

processes, volcanic degassing, aqueous alteration when possible and geologically reasonable processes [6]. In addition, the correlation causation effects discussed here may have regional variability, so causes of correlation do not have to be the same for all regions.
As mentioned before in the introduction, the summary products can rarely be attributed to a single mineralogy, and many may be partially influenced by non-geologic factors. The advantage of including all products is that we do not have to make prior assumptions on the processes or mineralogy that underlie the element distribution. However, for example for the element aluminum, it seems that for some of the summary products with the highest impact (e.g. BD3100) some effect of the atmosphere cannot be excluded.

5.5 Conclusion

The modelling work has proven useful for testing the relation between the global maps of the gamma-ray element concentrations and CRISM mineralogy. The results show that for none of the elements a single process is sufficient to explain all the variance of the element concentrations. For most elements the general variation can be explained. Also using different visualization method we have displayed for which regions on Mars the modeling is most accurate. Most element models have an explained variance between 40-50%. In general, heterogeneity in the subsurface, or minerals that do not have spectral features in the wavelength range of CRISM are the most likely causes of low model accuracy. The model for calcium has the lowest accuracy, where the variance is mostly unexplained. We consider that this inaccuracy may indicate variance primarily caused by Ca-rich feldspars in basalts, which cannot be measured with the CRISM data. From several models, we are able to improve previous interpretations for the geological processes that have influenced elemental distributions. The models for silicon and Cl show that mantling processes can be of significant influence for some element distributions. The enrichment of the volatile elements H_2O, Cl and S, in the Medusae Formation is best explained by the product BD19002, mostly related to bound and unbound H_2O. This supports the interpretation of these elements being enriched due to volcanic degassing in this region. The predictive modelling for K and Th shows the significance of the summary product BD22102 to explain the element enrichment in the northern lowlands. That product describes a common spectral feature of sulfate minerals. The relation would favor the notion of aqueous alteration in acidic conditions in the northern lowlands, which causes K and Th to become mobile.

Synthesis: CRISM's perspective on Martian global geology

6

The first chapter of this thesis introduces the underlying motivation for the performed studies, which states that new global geological insights could come from either new data or new data approaches. The new data presented in this thesis are the global CRISM MRDR summary product maps and the Mars analog rock spectral images. Each chapter contains a novel analysis strategy performed on either of these datasets. In this last synthesis chapter, the implications of the new datasets (Section 6.1) and novel application of methods (Section 6.2) are evaluated regarding the impact on Martian geological remote sensing. In Section 6.3 the geological insights resulting from the studies are discussed.

6.1 New data

As described before, in contrast to OMEGA and TES datasets, the CRISM MRDR data is not a commonly used dataset for Mars geological studies. Despite the difficulties with this data, such as inter-observational differences and shallow absorption features, the work in this thesis has demonstrated its potential for global geological remote sensing studies.

The Mars remote sensing work in this thesis is performed based on the spectra itself rather than analyzing modeled mineral dominance. The latter is how most recent global studies analyze the OMEGA [84] and TES [87] infrared spectral data where spectral endmembers are used to fit the Mars spectra for mineral phase quantification. Instead, for the first time, the revised spectral parameters of Viviano-Beck [106] are evaluated globally for the multispectral mapping mode data of CRISM (Chapter 2).

The fact that the surface types classified from the CRISM data are consistent with earlier surface type studies [85, 87, 84] supports the applicability of this data for geological remote sensing. Also individual summary product maps for especially the primary minerals olivine and pyroxene are consistent with earlier mapping studies such as Koeppen et al. [59], Bandfield et al [3], Riu et al. [84], and Ody et al. [77]. The spectral features of secondary alteration minerals are rather shallow, and especially after averaging the summary product values are low. Nevertheless, some products have been important to distinguish compositional distinct regions such as Nili Fossae and Meridiani.

The new spectral images of Mars analog rocks in Chapter 3 have been a useful dataset to verify some of the interpretations of summary products. With this dataset, the summary products are tested for the first time at a multispectral resolution, for Mars analog rocks. By analyzing the rocks for spatial coherent patterns the different interpretations for each summary product are presented along a colorbar. This way it is tested to what mineralogy, and at which summary product value, the summary product responds, besides the intended mineralogy. This resulted in some new alternative interpretations of the products in addition to those of Pelkey [82] and Viviano-Beck [106]. Also, application of non-mineral products, such as ICER-1, are tested, since these are also used for the global analysis. This product which is originally developed to differentiate CO_2 and H_2O ice shows to explain a similar distribution as product BD1435 related to hydrated minerals.

In conclusion, the CRISM MRDR data was successfully used for global geological studies. However, it must be mentioned that the analysis presented here is based on averaged summary product values. At the original resolution, it remains complicated to distinguish between spectral differences related to differences in surface geology and which are artifacts in the data. Within the work in Chapters 2 and 5 the averaging helped to overcome most of these problems with the data. The MSc work of Rachael Marshal has shown that also at original resolution information can be extracted to characterize the local geology for the northern lowlands [67]. There is ongoing work regarding updated CRISM MRDR data to reduce the inter-observational differences [90]. These updated data products would significantly improve the potential of the data.

6.2 Novel application of methods

The exploratory research presented here intended that the methods needed to be transparent and unsupervised. For this reason, most of the studies within this thesis have a data-driven approach in common. Both global remote sensing studies in Chapters 2 and 5 present novel multi-variate data analysis techniques and in Chapter 4 it was tested whether the absorption wavelength can be used to relate with the geochemistry and related geological history of the rocks.

The summary products resemble the transparent, data-driven approach of this research. How the summary product maps compare to other mineralogical studies is described already in the previous section (6.1). The benefit of using the summary products for the applied statistical approach is that these give continuous values for each pixel. This makes the products useful for the averaging and the statistical clustering method presented in Chapter 2 and the linear modeling in Chapter 5. For these methods, however, the summary products had to be normalized and standardized to make it possible to compare the values of different products. The downside of this stretching of summary product values is that it can exaggerate the dominance of a mineralogy and complicates the information is reduced to relative dominance on the global surface. This way you lose the information of, for example, the absorption depth of the feature which could be an indicator of the mineralogical dominance on the surface. Chapter 3 shows that depending on applied stretching values, the summary product can be interpreted differently.

Although the multi-variate data does not require a prior variable selection, this also complicates the interpretation. Both global remote sensing studies in this thesis required an additional statistical method to indicate the importance of each variable on defining the surface type (Chapter 2) or the linear model (Chapter 5). These statistical methods helped to better understand the importance of some of the variables but often the individual global maps were still required to verify the significance of the variable.

The benefit of not doing the variable selection is that all summary products are used including those related to chemical weathering (ISLOPE-1), dust, and hydration (BD1900). These products have been of importance in both global remote sensing studies. Although they are not related to mineralogy the products characterize interesting geological conditions in specific regions such as Medusae Fossae, northern lowlands and Ophir Planum.

In both Chapters 4 and 5 the geochemistry is modeled from spectral information. The global model has proven to be useful to test how much variance within the element concentration can be explained by the CRISM data. The benefit of the used model is that it did not overestimate the relationships between data and therefore also allows for bad models. This way it was shown that none of the variance for Ca could be explained by the CRISM data.

The analog study with Pilbara greenstones indicates that not just absorption depths but also absorption wavelengths can be used to predict the rock geochemistry. This methodology has not been applied for Mars remote sensing studies yet, but the results are promising to distinguish diagenetic rocks from hydrothermal rocks on Mars.

6.3 Implications global geology

Although the remote sensing studies within this thesis are performed at a global level, the geology is interpreted locally. This corresponds to how it was described in Ehlmann et al [31] that although there are global geological trends, the conditions along the surface have not been homogeneous. The CRISM data analysis studies have touched some of the most debated regions on Mars. Because of the earlier described limitations of the data the geological interpretations in the surface type analysis (Chapter 2) and geochemical modeling (Chapter 5) are always mentioned within some degree of uncertainty. Nevertheless, the aim of this thesis to give the CRISM perspective on the global geology of Mars is still achieved.

Differences between the northern lowlands and southern highlands of Mars have been described elaborately in the literature regarding differences in the topography [18], thermal spectral differences [5], and geochemical differences [36, 57]. The work of Chapter 2 includes the CRISM perspective on this dichotomy. The findings are consistent with the thermal infrared observations in that the northern lowlands is characterized by a low mafic mineral (i.e. olivine and pyroxene) concentration. Different from other remote sensing studies, however, are the elevated values for the summary products in the northern lowlands describing hydroxyl absorption features of secondary alteration minerals. Earlier studies such as the one carried out by Mustard et al [76] have concluded that the northern lowlands do not contain hydrated minerals because of the lack of distinct hydroxyl absorption features in the OMEGA dataset. Although the summary product values are small, which relates to shallow absorption features, this observation adds new information to the debate whether the northern lowlands have a distinct composition due to weathering conditions or differences in the volcanic material. A follow-up MSc work of Rachael Marshall [67] studying the northern lowlands at the original CRISM MRDR resolution ($\sim$ 200 m/pix) shows that the northern lowlands can be subdivided in northern Acidalia and southern Acidalia, where the transition coincides with the one observed by Rogers et al. [85]. Also at the original CRISM resolution the products BD2210, BD2100, BD1750, BD3400 show slightly higher values, but the level of noise in the data complicates to be conclusive on the presence of evaporite minerals [67].

Similar to what was found by other remote sensing studies the fine nano-phase ferric oxide dust has a significant influence on the reflectance spectra of the CRISM data and is dominant especially around the equator on Mars [88]. Spectrally the dust-covered region appears to be rather homogeneous. Only a few CRISM mosaic tiles covering the Medusae Fossae formation have slightly higher BD1900

values which is interesting as the result of a spectral water feature of water.
The sensitivity of the spectra for the dust made it possible to study the impact of the dust on the geochemical element maps (Chapter 5). Especially for the model of Si the summary products that are categorized as dust products in Chapter 2 have a high impact. This is consistent with the findings of Viviano et al [105] who concluded that the depletion of Si does not relate to the bedrock underneath the dust and should therefore be related to the dust coverage thickness. The variance explained by the models for Fe, K, Th increased when the dust-covered pixels were not considered which could indicate that the dust is obscuring interesting spectral variance relate to these elements.
Within the southern highlands, the mineralogical variation within the CRISM is consistent with earlier studies of the regions Nilli Fossae, Syrtis Major, and Meridiani. Although the findings in Chapter 2 have not resulted in new interpretations, the fact that these regions were characterized as unique regions was of importance to indicate the potential of the CRISM data for geological studies. Besides similarities with previous surface type studies, the main difference is that in the study in Chapter 2 the Hesperian terrains and Noachian terrains were not classified as distinct clusters, while this was the case in the OMEGA [84] and TES [87] data. On the other hand, the CRISM surface type study did distinguish new regions that were not observed before. In Chapter 2 these regions, Solis Planum, Ophir Planum, and Hellas, are described as clusters with a potential geological origin. The uncertainty is because it is unsure whether the spectral difference is related to atmospheric effects or geological variance.

6.4 Conclusion and future work

All together, the work in this thesis has given an overview of the possibilities and limitations of the CRISM dataset. The CRISM data in combination of novel application of methods has contributed to new perspectives on the Martian geology by defining new surface types and provide new information or earlier defined surface types. In combination with the geochemistry the correlation between the geochemical gamma-ray element concentration maps and mineralogical infrared maps is quantified for the first time. The importance of the summary product on the predictive model is used to interpret the local geology using both geochemical and mineralogical information.
The geochemical modeling could be extended by adding more information, possibly of other datasets such as those from the TES dataset. This way it could be tested whether adding mineral inform-

ation that is not well described by the CRISM data, such as feldspar minerals, would improve the modeling results. The new datasets, such as the global summary product maps are publicly available and can therefore be used for future studies, possible at the original, non-averaged resolution. The spectral images of Mars analog rocks have shown to be useful for verification of the summary products. Future work on this dataset could focus on requires adding more data, for example, thin section analysis, to better conclude on all the variance explained by each summary product. The Mars analog work on the Pilbara Rocks shows that mapping the absorption wavelength could be of interest for future work on Mars remote sensing to differentiate between rocks formed in hydrothermal and low-grade metamorphic conditions.

Bibliography

[1] M. S. Abweny, F. J. van Ruitenbeek, B. de Smeth, T. Woldai, F. D. van der Meer, T. Cudahy, T. Zegers, J.-K. Blom, and B. Thuss. Short-wavelength infrared (swir) spectroscopy of low-grade metamorphic volcanic rocks of the pilbara craton. *Journal of African Earth Sciences*, 117:124–134, 2016.

[2] J. B. Balta and H. Y. McSween Jr. Water and the composition of martian magmas. *Geology*, 41(10):1115–1118, 2013.

[3] J. L. Bandfield. Global mineral distributions on mars. *Journal of Geophysical Research: Planets*, 107(E6):9–1 – 9–20, 2002.

[4] J. L. Bandfield, T. D. Glotch, and P. R. Christensen. Spectroscopic identification of carbonate minerals in the martian dust. *Science*, 301(5636):1084–1087, 2003.

[5] J. L. Bandfield, V. E. Hamilton, and P. R. Christensen. A global view of martian surface compositions from mgs-tes. *Science*, 287(5458):1626–1630, 2000.

[6] H. Beebee, C. Hitchcock, and P. Menzies. *The Oxford handbook of causation*. Oxford University Press, 2009.

[7] J. L. Benson, P. B. James, B. A. Cantor, and R. Remigio. Interannual variability of water ice clouds over major martian volcanoes observed by moc. *Icarus*, 184(2):365–371, 2006.

[8] J. Bibring, Y. Langevin, J. F. Mustard, F. Poulet, R. Arvidson, A. Gendrin, B. Gondet, N. Mangold, P. Pinet, F. Forget, M. Berthé, J. Bibring, A. Gendrin, C. Gomez, B. Gondet, D. Jouglet, F. Poulet, A. Soufflot, M. Vincendon, M. Combes, P. Drossart, T. Encrenaz, T. Fouchet, R. Merchiorri, G. Belluci, F. Altieri, V. Formisano, F. Capaccioni, P. Cerroni, A. Coradini, S. Fonti, O. Korablev, V. Kottsov, N. Ignatiev, V. Moroz, D. Titov, L. Zasova, D. Loiseau, N. Mangold, P. Pinet, S. Douté, B. Schmitt, C. Sotin, E. Hauber, H. Hoffmann, R. Jaumann, U. Keller, R. Arvidson, J. F. Mustard, T. Duxbury, F. Forget, and G. Neukum. Global mineralogical and aqueous mars history derived from omega/mars express data. *Science*, 312(5772):400–404, 2006.

[9] J. P. Bibring, Y. Langevin, A. Gendrin, B. Gondet, F. Poulet, M. Berthé, A. Soufflot, R. Arvidson, N. Mangold, J. Mustard, and P. Drossart. Mars surface diversity as revealed by the omega/mars express observations. *Science*, 307(5715):1576–1581, 2005.

[10] W. V. Boynton, G. J. Taylor, L. G. Evans, R. C. Reedy, R. Starr, D. M. Janes, K. E. Kerry, D. M. Drake, K. J. Kim, R. M. S. Williams, M. K. Crombie, J. M. Dohm, V. Baker, A. E. Metzger, S. Karunatillake, J. M. Keller, H. E. Newsom, J. R. Arnold, J. Brückner, P. A. J. Englert, O. Gasnault, A. L. Sprague, I. Mitrofanov, S. W. Squyres, J. I. Trombka, L. d'Uston, H. Wänke, and D. K. Hamara. Concentration of h, si, cl, k, fe, and th in the low and mid latitude regions of mars. *Journal of Geophysical Research: Planets*, 112(E12), 2007.

[11] C. Brauhart, D. Huston, and A. Andrew. Oxygen isotope mapping in the panorama vms district, pilbara craton, western australia: applications to estimating temperatures of alteration and to exploration. *Mineralium Deposita*, 35(8):727–740, 2000.

[12] C. W. Brauhart. *Regional alteration systems associated with Arcean volcanogenic massive sulfide deposits at Panorama, Pilbara, Western Australia.* PhD thesis, University of Western Australia, 1999.

[13] C. W. Brauhart, D. I. Groves, and P. Morant. Regional alteration systems associated with volcanogenic massive sulfide mineralization at panorama, pilbara, western australia. *Economic Geology*, 93(3):292–302, 1998.

[14] C. W. Brauhart, D. L. Huston, D. I. Groves, E. J. Mikucki, and S. J. Gardoll. Geochemical mass-transfer patterns as indicators of the architecture of a complete volcanic-hosted massive sulfide hydrothermal alteration system, panorama district, pilbara, western australia. *Economic Geology*, 96(5):1263–1278, 2001.

[15] R. G. Brereton and G. R. Lloyd. Partial least squares discriminant analysis: taking the magic away. *Journal of Chemometrics*, 28(4):213–225, 2014.

[16] A. J. Brown, W. M. Calvin, P. C. McGuire, and S. L. Murchie. Compact reconnaissance imaging spectrometer for mars (crism) south polar mapping: First mars year of observations. *Journal of Geophysical Research: Planets (1991–2012)*, 115(E2), 2010.

[17] A. J. Brown, S. J. Hook, A. M. Baldridge, J. K. Crowley, N. T. Bridges, B. J. Thomson, G. M. Marion, C. R. de Souza Filho, and J. L. Bishop. Hydrothermal formation of clay-carbonate alteration assemblages in the nili fossae region of mars. *Earth and Planetary Science Letters*, 297(1):174–182, 2010.

[18] M. H. Carr and J. W. Head. Geologic history of mars. *Earth and Planetary Science Letters*, 294(3):185–203, 2010.

[19] J. Carter and F. Poulet. Ancient plutonic processes on mars inferred from the detection of possible anorthositic terrains. *Nature Geoscience*, 6:1008, 2013.

[20] M. Cathelineau. Cation site occupancy in chlorites and illites as function of temperature. *Clay minerals*, 23(4):471–85, 1988.

[21] P. R. Christensen, D. L. Anderson, S. C. Chase, R. N. Clark, H. H. Kieffer, M. C. Malin, J. C. Pearl, J. Carpenter, N. Bandiera, F. G. Brown, et al. Thermal emission spectrometer experiment: Mars observer mission. *Journal of Geophysical Research: Planets*, 97(E5):7719–7734, 1992.

[22] P. R. Christensen, H. Y. McSween, J. L. Bandfield, S. W. Ruff, A. D. Rogers, V. E. Hamilton, N. Gorelick, M. B. Wyatt, B. M. Jakosky, H. H. Kieffer, M. C. Malin, and J. E. Moersch. Evidence for magmatic evolution and diversity on mars from infrared observations. *Nature*, 436(7050):504–509, 2005.

[23] P. R. Christensen, R. Morris, M. D. Lane, J. L. Bandfield, and M. Malin. Global mapping of martian hematite mineral deposits: Remnants of water driven processes on early mars. *Journal of Geophysical Research: Planets*, 106(E10):23873–23885, 2001.

[24] R. N. Clark, T. V. V. King, M. Klejwa, G. A. Swayze, and N. Vergo. High spectral resolution reflectance spectroscopy of minerals. *Journal of Geophysical Research: Solid Earth*, 95(B8):12653–12680, 1990.

[25] J. Cohen. Statistical power analysis for the behavioral sciences new york. *NY: Academic*, 1988.

[26] J. Cohen. Statistical power analysis. *Current directions in psychological science*, 1(3):98–101, 1992.

[27] P. De Caritat, I. Hutcheon, and J. Walshe. Chlorite geothermometry: a review. *Clays and Clay Minerals,*, 41, 1993.

[28] W. A. Deer, R. A. Howie, and J. Zussman. *Rock-forming minerals. Vol. 3B, Layered silicates excluding micas and clay minerals.* Geological Society, 2009.

[29] J. M. Dohm, V. R. Baker, W. V. Boynton, A. G. Fairén, J. C. Ferris, M. Finch, R. Furfaro, T. M. Hare, D. M. Janes, J. S. Kargel, S. Karunatillake, J. Keller, K. Kerry, K. J. Kim, G. Komatsu, W. C. Mahaney, D. Schulze-Makuch, L. Marinangeli, G. G. Ori, J. Ruiz, and S. J. Wheelock. Grs evidence and the possibility of paleooceans on mars. *Planetary and Space Science*, 57(5):664–684, 2009.

[30] M. P. Doublier, T. Roache, S. Potel, and C. Laukamp. Short-wavelength infrared spectroscopy of chlorite can be used to determine very low metamorphic grades. *European Journal of Mineralogy*, 24(5):891–902, 2012.

[31] B. L. Ehlmann and C. S. Edwards. Mineralogy of the martian surface. *Annual Review of Earth and Planetary Sciences*, 42(1):291–315, 2014.

[32] B. L. Ehlmann, J. F. Mustard, R. N. Clark, G. A. Swayze, and S. L. Murchie. Evidence for low-grade metamorphism, hydrothermal alteration, and diagenesis on mars from phyllosilicate mineral assemblages. *Clays and Clay Minerals*, 59(4):359–377, 2011.

[33] B. L. Ehlmann, J. F. Mustard, G. A. Swayze, R. N. Clark, J. L. Bishop, F. Poulet, D. J. Des Marais, L. H. Roach, R. E. Milliken, J. J. Wray, O. Barnouin-Jha, and S. L. Murchie. Identification of hydrated silicate minerals on mars using mro-crism: Geologic context near nili fossae and implications for aqueous alteration. *Journal of Geophysical Research: Planets*, 114(E2), 2009.

[34] E. Essene and D. Peacor. Clay mineral thermometry-a critical perspective. *Clays and clay minerals*, 43(5):540–553, 1995.

[35] E. M. Fischer and C. M. Pieters. The continuum slope of mars: Bidirectional reflectance investigations and applications to olympus mons. *Icarus*, 102(2):185–202, 1993.

[36] O. Gasnault, G. Jeffrey Taylor, S. Karunatillake, J. Dohm, H. Newsom, O. Forni, P. Pinet, and W. V. Boynton. Quantitative geochemical mapping of martian elemental provinces. *Icarus*, 207(1):226–247, 2010.

[37] A. Gendrin, N. Mangold, J. Bibring, Y. Langevin, B. Gondet, F. Poulet, G. Bonello, C. Quantin, J. Mustard, R. Arvidson, and S. LeMouélic. Sulfates in martian layered terrains: The omega/mars express view. *Science*, 307(5715):1587–1591, 2005.

[38] B. Hahn, S. McLennan, and E. Klein. Martian surface heat production and crustal heat flow from mars odyssey gamma-ray spectrometry. *Geophysical Research Letters*, 38(14), 2011.

[39] V. E. Hamilton, H. Y. McSween, and B. Hapke. Mineralogy of martian atmospheric dust inferred from thermal infrared spectra of aerosols. *Journal of Geophysical Research: Planets*, 110(E12), 2005.

[40] A. Hardy. *An examination of procedures for determining the number of clusters in a data set*, pages 178–185. Springer, 1994.

[41] J. Harloff and G. Aarnold. The near-infrared continuum slope of martian dark region reflectance spectra. *Earth, Moon, and Planets*, 88(4):223–245, 2000.

[42] J. K. Harmon, M. C. Nolan, D. I. Husmann, and B. A. Campbell. Arecibo radar imagery of mars: The major volcanic provinces. *Icarus*, 220(2):990–1030, 2012.

[43] T. Hastie, R. Tibshirani, and J. Friedman. *Unsupervised Learning*, pages 485–585. Springer New York, New York, NY, 2009.

[44] A. H. Hickman. Review of the pilbara craton and fortescue basin, western australia: crustal evolution providing environments for early life. *Island Arc*, 21(1):1–31, 2012.

[45] T. M. Hoefen, R. N. Clark, J. L. Bandfield, M. D. Smith, J. C. Pearl, and P. R. Christensen. Discovery of olivine in the nili fossae region of mars. *Science*, 302(5645):627–630, 2003.

[46] D. Hood, S. Karunatillake, O. Gasnault, A. Williams, B. Dutrow, L. Ojha, S. Kobs, K. Kim, J. Heldmann, and C. Fralick. Contrasting regional soil alteration across the topographic dichotomy of mars. *Geophysical Research Letters*, 46(23):13668–13677, 2019.

[47] D. R. Hood, T. Judice, S. Karunatillake, D. Rogers, J. M. Dohm, D. Susko, and L. K. Carnes. Assessing the geologic evolution of greater thaumasia, mars. *Journal of Geophysical Research: Planets*, 121(9):1753–1769, 2016.

[48] B. H. Horgan, E. A. Cloutis, P. Mann, and J. F. Bell III. Near-infrared spectra of ferrous mineral mixtures and methods for their identification in planetary surface spectra. *Icarus*, 234:132–154, 2014.

[49] B. H. Horgan, R. J. Smith, E. A. Cloutis, P. Mann, and P. R. Christensen. Acidic weathering of basalt and basaltic glass: 1. near-infrared spectra, thermal infrared spectra, and implications for mars. *Journal of Geophysical Research: Planets*, 122(1):172–202, 2017.

[50] E. J. Humbo. Hyperspectral imaging in swir and lwir of low-grade metamorphic rocks. Master's thesis, Faculty of Geo-Information Science and Earth-Observation (ITC), University of Twente, 2019.

[51] W. Härdle and L. Simar. *Applied multivariate statistical analysis*, volume 22007. Springer, 2007.

[52] T. Irvine and W. Baragar. A guide to the chemical classification of the common volcanic rocks. *Canadian journal of earth sciences*, 8(5):523–548, 1971.

[53] M. Kahre, R. Haberle, J. Hollingsworth, and M. Wolff. Marci-observed clouds in the hellas basin during northern hemisphere summer on mars: Interpretation with the nasa/ames legacy mars global climate model. *Icarus*, 338:113512, 2020.

[54] O. Kamps. Defining surface types of mars using global crism summary product maps. DANS.

[55] O. M. Kamps, R. D. Hewson, F. J. A. van Ruitenbeek, and F. D. van der Meer. Defining surface types of mars using global crism summary product maps. *Journal of Geophysical Research: Planets*, 125(8):e2019JE006337, 2020.

[56] O. M. Kamps, R. D. Hewson, F. J. A. van Ruitenbeek, and F. D. van der Meer. Defining surface types using global crism summary product maps. 2020.

[57] S. Karunatillake, S. W. Squyres, G. J. Taylor, J. M. Keller, O. Gasnault, L. G. Evans, R. C. Reedy, R. Starr, W. Boynton, D. M. Janes, K. E. Kerry, J. M. Dohm, A. L. Sprague, B. C. Hahn, and D. Hamara. Composition of northern low-albedo regions of mars: Insights from the mars odyssey gamma ray spectrometer. *Journal of Geophysical Research: Planets*, 111(E3), 2006.

[58] S. Karunatillake, J. J. Wray, S. W. Squyres, G. J. Taylor, O. Gasnault, S. M. McLennan, W. Boynton, M. R. El Maarry, and J. M. Dohm. Chemically striking regions on mars and stealth revisited. *Journal of Geophysical Research: Planets*, 114(E12), 2009.

[59] W. C. Koeppen and V. E. Hamilton. Global distribution, composition, and abundance of olivine on the surface of mars from thermal infrared data. *Journal of Geophysical Research: Planets*, 113(E5), 2008.

[60] R. F. Kokaly, R. N. Clark, G. A. Swayze, K. E. Livo, T. M. Hoefen, N. C. Pearson, R. A. Wise, W. M. Benzel, H. A. Lowers, R. L. Driscoll, and A. J. Klein. Usgs spectral library version 7. Report 1035, 2017.

[61] M. D. Kraft, J. R. Michalski, and T. G. Sharp. Effects of pure silica coatings on thermal emission spectra of basaltic rocks: Considerations for martian surface mineralogy. *Geophysical Research Letters*, 30(24), 2003.

[62] M. J. V. Kranendonk, A. H. Hickman, R. H. Smithies, D. R. Nelson, and G. Pike. Geology and tectonic evolution of the archean north pilbara terrain, pilbara craton, western australia. *Economic Geology*, 97(4):695–732, 2002.

[63] R. R. Large, J. B. Gemmell, H. Paulick, and D. L. Huston. The alteration box plot: A simple approach to understanding the

relationship between alteration mineralogy and lithogeochemistry associated with volcanic-hosted massive sulfide deposits. *Economic geology*, 96(5):957–971, 2001.

[64] H.-D. Li, Q. Xu, and Y.-Z. Liang. libpls: An integrated library for partial least squares regression and linear discriminant analysis. *Chemometrics and Intelligent Laboratory Systems*, 176, 03 2018.

[65] K. E. Mandt, S. L. de Silva, J. R. Zimbelman, and D. A. Crown. Origin of the medusae fossae formation, mars: Insights from a synoptic approach. *Journal of Geophysical Research: Planets*, 113(E12), 2008.

[66] N. Mangold, G. Dromart, V. Ansan, F. Salese, M. G. Kleinhans, M. Massé, C. Quantin-Nataf, and K. M. Stack. Fluvial regimes, morphometry, and age of jezero crater paleolake inlet valleys and their exobiological significance for the 2020 rover mission landing site. *Astrobiology*, 2020.

[67] R. M. F. Marshal. Characterising the compositional variations of the martian northern lowlands: insights from crism and omega datasets. Master's thesis, Faculty of Geo-Information Science and Earth-Observation (ITC), University of Twente, 2020.

[68] P. C. McGuire, J. L. Bishop, A. J. Brown, A. A. Fraeman, G. A. Marzo, M. Frank Morgan, S. L. Murchie, J. F. Mustard, M. Parente, S. M. Pelkey, T. L. Roush, F. P. Seelos, M. D. Smith, L. Wendt, and M. J. Wolff. An improvement to the volcano-scan algorithm for atmospheric correction of crism and omega spectral data. *Planetary and Space Science*, 57(7):809–815, 2009.

[69] H. Y. McSween, G. J. Taylor, and M. B. Wyatt. Elemental composition of the martian crust. *Science*, 324(5928):736–739, 2009.

[70] H. Y. McSween Jr., T. C. Labotka, and C. E. Viviano-Beck. Metamorphism in the martian crust. *Meteoritics & Planetary Science*, 50(4):590–603, 2015.

[71] K. A. Milam, H. Y. McSween Jr., J. Moersch, and P. R. Christensen. Distribution and variation of plagioclase compositions on mars. *Journal of Geophysical Research: Planets*, 115(E9), 2010.

[72] M. Morgan, F. Seelos, and S. Murchie. The crism analysis toolkit (cat): Overview and recent updates. *LPICo*, 1986:7121, 2017.

[73] R. Morris, T. Graff, C. Achilles, D. Agresti, D. Ming, and D. Golden. Visible and near-ir reflectance spectra of mars analogue materials under arid conditions for interpretation of martian surface mineralogy. In *Lunar and Planetary Science Conference*, 2011.

[74] S. Murchie, R. Arvidson, P. Bedini, K. Beisser, J.-P. Bibring, J. Bishop, J. Boldt, P. Cavender, T. Choo, R. T. Clancy, E. H. Darlington, D. Des Marais, R. Espiritu, D. Fort, R. Green, E. Guinness, J. Hayes, C. Hash, K. Heffernan, J. Hemmler, G. Heyler, D. Humm, J. Hutcheson, N. Izenberg, R. Lee, J. Lees, D. Lohr, E. Malaret, T. Martin, J. A. McGovern, P. McGuire, R. Morris, J. Mustard, S. Pelkey, E. Rhodes, M. Robinson, T. Roush, E. Schaefer, G. Seagrave, F. Seelos, P. Silverglate, S. Slavney, M. Smith, W.-J. Shyong, K. Strohbehn, H. Taylor, P. Thompson, B. Tossman, M. Wirzburger, and M. Wolff. Compact reconnaissance imaging spectrometer for mars (crism) on mars reconnaissance orbiter (mro). *Journal of Geophysical Research: Planets*, 112(E5):1–57, 2007.

[75] S. Murchie, L. Kirkland, S. Erard, J. Mustard, and M. Robinson. Near-infrared spectral variations of martian surface materials from ism imaging spectrometer data. *Icarus*, 147(2):444–471, 2000.

[76] J. F. Mustard, F. Poulet, A. Gendrin, J.-P. Bibring, Y. Langevin, B. Gondet, N. Mangold, G. Bellucci, and F. Altieri. Olivine and pyroxene diversity in the crust of mars. *Science*, 307(5715):1594–1597, 2005.

[77] A. Ody, F. Poulet, Y. Langevin, J.-P. Bibring, G. Bellucci, F. Altieri, B. Gondet, M. Vincendon, J. Carter, and N. Manaud. Global maps of anhydrous minerals at the surface of mars from omega/mex. *Journal of Geophysical Research: Planets*, 117(E11):1–14, 2012.

[78] K. Ogohara and T. Satomura. Northward movement of martian dust localized in the region of the hellas basin. *Geophysical research letters*, 35(13), 2008.

[79] L. Ojha and K. Lewis. The density of the medusae fossae formation: Implications for its composition, origin, and importance in martian history. *Journal of Geophysical Research: Planets*, 123(6):1368–1379, 2018.

[80] M. Panalytical. Malvern panalytical- a spectris compony. Retrieved October 1st 2020 from `https://www.https://www.malvernpanalytical.com`.

[81] M. Pasero. The new ima list of minerals – a work in progress– updated: March 2018. 2018.

[82] S. M. Pelkey, J. F. Mustard, S. Murchie, R. T. Clancy, M. Wolff, M. Smith, R. Milliken, J. Bibring, A. Gendrin, F. Poulet, Y. Langevin, and B. Gondet. Crism multispectral summary products: Parameterizing mineral diversity on mars from reflectance. *Journal of Geophysical Research: Planets*, 112(E8):1–18, 2007.

[83] R. J. Phillips, M. T. Zuber, S. C. Solomon, M. P. Golombek, B. M. Jakosky, W. B. Banerdt, D. E. Smith, R. M. Williams, B. M. Hynek, O. Aharonson, et al. Ancient geodynamics and global-scale hydrology on mars. *Science*, 291(5513):2587–2591, 2001.

[84] L. Riu, F. Poulet, J. P. Bibring, and B. Gondet. The m3 project: 2 - global distributions of mafic mineral abundances on mars. *Icarus*, 322:31–53, 2019.

[85] A. D. Rogers, J. L. Bandfield, and P. R. Christensen. Global spectral classification of martian low-albedo regions with mars global surveyor thermal emission spectrometer (mgs-tes) data. *Journal of Geophysical Research: Planets*, 112(E2):1–29, 2007.

[86] A. D. Rogers and P. R. Christensen. Surface mineralogy of martian low-albedo regions from mgs-tes data: Implications for upper crustal evolution and surface alteration. *Journal of Geophysical Research: Planets*, 112(E1):1–18, 2007.

[87] A. D. Rogers and V. E. Hamilton. Compositional provinces of mars from statistical analyses of tes, grs, omega and crism data. *Journal of Geophysical Research: Planets*, 120(1):62–91, 2015.

[88] S. W. Ruff and P. R. Christensen. Bright and dark regions on mars: Particle size and mineralogical characteristics based on thermal emission spectrometer data. *Journal of Geophysical Research: Planets*, 107(E12):2–1 – 2–22, 2002.

[89] F. J. A. Ruitenbeek, P. Debba, F. D. van der Meer, T. Cudahy, M. Meijde, and M. Hale. Mapping white micas and their absorption wavelengths using hyperspectral band ratios. *Remote Sensing of Environments*, 102(3):211–222, 2006.

[90] F. Seelos and S. Murchie. Crism mapping data empirical radiometric reconciliation for the next-generation mars global multispectral map. In *Lunar and Planetary Science Conference*, volume 49, 2018.

[91] G. Serventi, C. Carli, M. Sgavetti, M. Ciarniello, F. Capaccioni, and G. Pedrazzi. Spectral variability of plagioclase–mafic mixtures (1): Effects of chemistry and modal abundance in reflectance spectra of rocks and mineral mixtures. *Icarus*, 226(1):282 – 298, 2013.

[92] N. Shikazono and H. Kawahata. Compositional differences in chlorite from hydrothermally altered rocks and hydrothermal ore deposits. *Canadian Mineralogist*, 25(3):465–474, 1987.

[93] D. E. Smith, M. T. Zuber, and G. A. Neumann. Seasonal variations of snow depth on mars. *Science*, 294(5549):2141–2146, 2001.

[94] R. H. Smithies. *Geochemistry of volcanic rocks of the northern Pilbara Craton*. Geological Survey of Western Australia, 2007.

[95] SPECIM. Specim - hyperspectral imaging cameras and systems. Retrieved September 28th 2020 from `https://www.specim.fi`.

[96] S. W. Squyres and A. H. Knoll. Sedimentary rocks at meridiani planum: Origin, diagenesis, and implications for life on mars. *Earth and Planetary Science Letters*, 240(1):1–10, 2005.

[97] K. L. Tanaka, J. A. Skinner, J. M. Dohm, R. P. Irwin Iii, E. J. Kolb, C. M. Fortezzo, T. Platz, G. G. Michael, and T. M. Hare. Geologic map of mars. Report 3292, 2014.

[98] G. J. Taylor, L. M. V. Martel, S. Karunatillake, O. Gasnault, and W. V. Boynton. Mapping mars geochemically. *Geology*, 38(2):183–186, 2010.

[99] G. J. Taylor, J. D. Stopar, W. V. Boynton, S. Karunatillake, J. M. Keller, J. Brückner, H. Wänke, G. Dreibus, K. E. Kerry, R. C. Reedy, L. G. Evans, R. D. Starr, L. M. V. Martel, S. W. Squyres, O. Gasnault, S. Maurice, C. d'Uston, P. Englert, J. M. Dohm, V. R. Baker, D. Hamara, D. Janes, A. L. Sprague, K. J. Kim, D. M. Drake, S. M. McLennan, and B. C. Hahn. Variations in k/th on mars. *Journal of Geophysical Research: Planets*, 111(E3), 2006.

[100] J. W. Tukey. *Exploratory data analysis*, volume 2. Reading, Mass., 1977.

[101] M. J. Van Kranendonk. *Revised lithostratigraphy of Archean supracrustal and intrusive rocks in the northern Pilbara Craton, Western Australia*. Geological Survey of Western Australia, 2006.

[102] F. J. van Ruitenbeek, T. Cudahy, M. Hale, and F. D. van der Meer. Tracing fluid pathways in fossil hydrothermal systems with near-infrared spectroscopy. *Geology*, 33(7):597–600, 2005.

[103] D. T. Vaniman, D. L. Bish, D. W. Ming, T. F. Bristow, R. V. Morris, D. F. Blake, S. J. Chipera, S. M. Morrison, A. H. Treiman, E. B. Rampe, M. Rice, C. N. Achilles, J. P. Grotzinger, S. M. McLennan, J. Williams, J. F. Bell, H. E. Newsom, R. T. Downs, S. Maurice, P. Sarrazin, A. S. Yen, J. M. Morookian, J. D. Farmer, K. Stack, R. E. Milliken, B. L. Ehlmann, D. Y. Sumner, G. Berger, J. A. Crisp, J. A. Hurowitz, R. Anderson, D. J. Des Marais, E. M. Stolper, K. S. Edgett, S. Gupta, and N. Spanovich. Mineralogy of a mudstone at yellowknife bay, gale crater, mars. *Science*, 343(6169):1243480, 2014.

[104] C. E. Viviano, J. E. Moersch, and H. Y. McSween. Implications for early hydrothermal environments on mars through the spectral evidence for carbonation and chloritization reactions in

the nili fossae region. *Journal of Geophysical Research: Planets*, 118(9):1858–1872, 2013.

[105] C. E. Viviano, S. L. Murchie, I. J. Daubar, M. F. Morgan, F. P. Seelos, and J. B. Plescia. Composition of amazonian volcanic materials in tharsis and elysium, mars, from mro/crism reflectance spectra. *Icarus*, 328:274–286, 2019.

[106] C. E. Viviano-Beck, F. P. Seelos, S. L. Murchie, E. G. Kahn, K. D. Seelos, H. W. Taylor, K. Taylor, B. L. Ehlmann, S. M. Wiseman, J. F. Mustard, and M. F. Morgan. Revised crism spectral parameters and summary products based on the currently detected mineral diversity on mars. *Journal of Geophysical Research: Planets*, 119(6):1403–1431, 2014.

[107] A. Weert. Hydrous alteration of lava flows on mauna loa (hawaii) compared to martian volcanic soils. Master's thesis, Faculty of Science, Vrije Universiteit Amsterdam, 2019.

[108] J. J. Wilkinson, Z. Chang, D. R. Cooke, M. J. Baker, C. C. Wilkinson, S. Inglis, H. Chen, and J. Bruce Gemmell. The chlorite proximitor: A new tool for detecting porphyry ore deposits. *Journal of Geochemical Exploration*, 152:10–26, 2015.

[109] J. Winchester and P. Floyd. Geochemical discrimination of different magma series and their differentiation products using immobile elements. *Chemical geology*, 20:325–343, 1977.

[110] S. Wold, M. Sjöström, and L. Eriksson. Pls-regression: a basic tool of chemometrics. *Chemometrics and Intelligent Laboratory Systems*, 58(2):109–130, 2001.

[111] J. J. Wray, S. T. Hansen, J. Dufek, G. A. Swayze, S. L. Murchie, F. P. Seelos, J. R. Skok, R. P. Irwin III, and M. S. Ghiorso. Prolonged magmatic activity on mars inferred from the detection of felsic rocks. *Nature Geoscience*, 6(12):1013–1017, 2013.

[112] M. B. Wyatt and H. Y. McSween Jr. Spectral evidence for weathered basalt as an alternative to andesite in the northern lowlands of mars. *Nature*, 417:263, 2002.

[113] A. Zane, R. Sassi, and C. V. Guidotti. New data on metamorphic chlorite as a petrogenetic indicator mineral, with special regard to greenschist-facies rocks. *The Canadian Mineralogist*, 36(3):713–726, 1998.

[114] M. T. Zuber, D. E. Smith, S. C. Solomon, D. O. Muhleman, J. W. Head, J. B. Garvin, J. B. Abshire, and J. L. Bufton. The mars observer laser altimeter investigation. *Journal of Geophysical Research: Planets*, 97(E5):7781–7797, 1992.

Biography

Oscar Kamps is born in 1992 in Purmerend, The Netherlands. In 2010 he completed his VWO at Da Vinci college in his hometown, Purmerend. His academic career started with a study Earth Sciences at the University of Amsterdam. After three years he obtained his bachelor degree. He continued his studies at Utrecht University where he completed the master studies Earth Structure and Dynamics. During this master he was introduced to ITC - Faculty of Geo-Information Science and Earth Observation resulting in a collaborative master thesis between ITC and Utrecht University, about the spectral difference between hydrothermal and metamorphic greenstones from the Pilbara Craton, Western Australia. In the same year he did an internship at the European Space Agency (ESA) where he discovered the field of planetary sciences. In this internship he did a landing site assessment for a assumed mission near the south pole of the Moon and contributed to Moon Mars analogue field studies of the Austrian Space Form (OEWF) and Euromoonmars project of ESA. After graduation he continued doing lunar landing site studies, this time within an international team of young scientists at the Lunar and Planetary Institute (LPI) in Houston, Texas. The obtained knowledge in planetary science, geology and spectral remote sensing studies has resulted in the work presented in this thesis on the application of CRISM mapping mode data for global geological Mars research.

Publications of the author

Journal publication

Kamps, O. M., Hood, D.R., Hewson, R. D., van Ruitenbeek, F. J. A., Karunatillake, S., Viviano, C.E. & van der Meer, F. D. *(in preparation)* Modelling GRS chemical maps of Mars with CRISM Multispectral Summary Product Maps. Icarus

Kamps, O. M., Hewson, R. D., van Ruitenbeek, F. J. A., & van der Meer, F. D. (2020). Defining surface types of Mars using global CRISM summary product maps. *Journal of Geophysical Research: Planets*, e2019JE006337.

Kamps, O. M., Van Ruitenbeek, F. J., Mason, P. R., & van der Meer, F. D. (2018). Near-infrared spectroscopy of hydrothermal versus low-grade metamorphic chlorites. *Minerals, 8(6)*, 259.

Allender, E. J., Orgel, C., Almeida, N. V., Cook, J., Ende, J. J., **Kamps, O.M**, Mazrouei, S., Slezak, T. J., Soini, A.J. & Kring, D. A. (2019). Traverses for the ISECG-GER design reference mission for humans on the lunar surface. *Advances in space research, 63(1)*, 692-727.

Magazine publication

Kamps, O.M. (2019) De geologie van Mars, een globaal perpectief. Geo brief(6)

Kamps, O.M., van der Meer, F.D. (September 2018) The Mars' surface composition puzzle. SAB newsletter

Conference proceedings

Kamps, O.M., Hood, D., Hewson, R.H., van Ruitenbeek, F.J.A., van der Meer, F.D., Karunatillake, S. (2020) GRS element modelling with CRISM summary, Oral presentation at the lunar and planetary science conference

Kamps, O.M., Hewson, R.D., van Ruitenbeek, F.J.A., van der Meer, F.D. (2019) Global mapping of mars with CRISM summary products, Poster presentation at the lunar and planetary science conference

Kamps, O.M., Hewson, R.D., van Ruitenbeek, F.J.A., van der Meer, F.D., Investigating Mars (2018) Element Distribution with CRISM Summary Products, Poster presentation at the lunar and planetary science conference

Kamps, O.M., Allender, E.J., Almeida, N.V., Cook, J., Ende, J.J., Mazrouei, S., Orgel, C., Slezak, T., Soini, A.J., Kring, D.A. (2017) Exploration of South Polar Region of the Moon: Tele-operated Traverses, Poster presentation at the lunar and planetary science conference

Kamps, O.M., Hewson, R.D., van Ruitenbeek, F.J.A., van der Meer, F.D. (2018) Investigating Martian element distribution with CRISM summary products, Poster presentation at the lunar and planetary science conference

Kamps, O.M., Foing, B.H., Batenburg, P. (2016) Towards a Moon Village: Young Lunar Explore Report, Poster presentation at the European Geosciences Union

Kamps, O.M, Foing, B.H., Flahaut, J.D. (2016) Lunar Polar Landing Sites, Poster presentation at COSPAR scientific assembly

Offringa, M.S., Foing, B.H., **Kamps, O.M.** (2016) Moon-Mars simulation campaign in volcanic Eifel: Remote science support and sample analysis, Poster presentation at COSPAR scientific assembly

Kamps, O.M., Flahaut, J.D., Foing, B.H. (2016) Lunar Polar Sites and Rover Traverse Planning for a Study on Volatiles and Ices, Poster presentation at the lunar and planetary science conference

Kamps, O.M., Foing, B.H., Offringa, M.S. (2016) Eifel field operation campaign supporting Moon Mars and NEO exploration, Poster presentation at COSPAR scientific assembly

Kamps, O.M., Offringa, M.S. & Foing, B.H. (2016) Preparations ExoGeoLab Lander for Lunar Analogue Field Campaign, Eifel, Germany, Poster presentation at the lunar and planetary science conference

Kamps, O.M., Foing, B.H, Flahaut, J.D. (2016) Traverses for lunar rovers and sample return teleoperated from Earth or cislunar orbit, Poster presentation at COSPAR scientific assembly

Kamps, O.M., Foing, B.H., Flahaut, J.D. (2016) Site Selection and Automatically Calculated Rover Traverse for a Lunar Teleoperated Landing Mission, Poster presentation at European Geosciences Union

Appendix

Table summary products

Product	Equation	Description	Rationale Viviano-Beck [106]	Additional remarks
Atmosphere				
ICER2_2	RB2600 anchor R2456 and R2530	Gauge 2.7 μm band	CO_2 vs H_2O ice/soil	High correlation atmosphere thickness
BD1400	$1\text{-}\left(\frac{R1395}{a*R1330+b*R1467}\right)$	1.4 μm band depth	Hydrated or hydroxylated minerals	Moderate correlation atmosphere thickness
BD1435	$1\text{-}\left(\frac{R1435}{a*R1370+b*R1470}\right)$	1.435 μm band depth	CO_2 ice, hydrated minerals	High correlation atmosphere thickness
BD1900R2	$1-\left(\frac{\frac{R1908}{RC1908}+\frac{R1914}{RC1914}+\frac{R1921}{RC1921}}{\frac{R1862}{RC1862}+\frac{R1869}{RC1869}+\frac{R1875}{RC1875}}, \frac{\frac{R1928}{RC1928}+\frac{R1934}{RC1934}+\frac{R1941}{RC1941}}{\frac{R2112}{RC2112}+\frac{R2120}{RC2120}+\frac{R2126}{RC2126}}\right)$ anchor at R1850 and R2060	1.9 μm band depth	H_2O	Moderate correlation atmosphere thickness
D2200	$1-\left(\frac{\frac{R2210}{RC2210}+\frac{R2230}{RC2230}}{2*\frac{R2165}{RC2165}}\right)$ anchor at R1815 and R2430	2.2 μm drop off	Al-OH minerals	Moderate correlation atmosphere thickness

Table 1 continued from previous page

	Product	Equation	Description	Rationale Viviano-Beck [106]	Additional remarks
	BD2355	$1\text{-}\left(\frac{R2355}{a*R2300+b*R2450}\right)$	2.355 μm band	Chlorite, prehnite, pumpellyite, carbonate and serpentine	Moderate correlation atmosphere thickness
	BD3000	$1\text{-}\left(\frac{R3000}{R2530*\frac{R2530}{R2210}}\right)$	μm band depth	Bound H_2O	Moderate correlation atmosphere thickness
Ice					
	BD1500_2	$1\text{-}\left(\frac{R1525}{a*R1367+b*R1808}\right)$	1.5 μm band depth	H_2O ice on surface or in atmosphere	high values in high latitudes, volcanoes and Syrtis
	BD1900_2	$0.5*\left(1-\left(\frac{R1930}{a*R1850+b*R2067}\right)\right)+ 0.5*\left(1-\left(\frac{R1985}{a*R1850+b*R2067}\right)\right)$	1.9 μm band depth	Bound molecular H_2O	
	SINDEX2*	$1\text{-}\left(\frac{a*2120+b*2400}{R2290}\right)$	Convexity at 2.29 μm	Hydrated sulfates	higher values around volcanoes
Dust					
	R770	R770	0.77 μm reflectance	Higher value more dusty or icy	High correlation with dust coverage index
	RBR	R770/R440	Red/blue ratio	Nano-phase ferric oxides	Moderate correlation with dust coverage index

Table 1 continued from previous page

Product	Equation	Description	Rationale Viviano-Beck [106]	Additional remarks
BD530_2	1-$\left(\frac{R530}{a*R614+b*R440}\right)$	0.53 μm band depth	Fine-grained crystalline hematite	High correlation with dust coverage index
RPEAK1	Wavelength where first derivative = 0 of fifth-order polynomial fit to reflectances at all valid VNIR wavelengths	Reflectance peak in VNIR	Olivine, pyroxene, or Fe-bearing glass	High correlation with dust coverage index
R1330	R1330	IR albedo 1.33 μm	Ices >dust >unaltered mafics	High correlation with dust coverage index
VAR	Fit a line from 1 to 2.3 m and find variance of observed values from fit values by summing in quadrature over the intervening wavelengths	1.0 – 2.3 μm spectral variance	Olivine and pyroxene	Moderate correlation with dust coverage index
ICER1_2	1-$\left(\frac{BD1435}{BD1500_2}\right)$	1.5 μm and 1.4 μm band depth ratio	CO_2 /H_2O ice mixtures	Moderate correlation with dust coverage index
Mafic minerals				
Mafic products (non-specified)				
BDI1000VIS*	Divide reflectances from R833 to R1023 by the modeled reflectance at RPEAK1, then integrate over (1 normalized radiances) to get integrated band depth	Integrated band depth 1μm VNIR	Olivine, pyroxene, or Fe-bearing glass	High correlation with dust coverage index

Table 1 continued from previous page

Product	Equation	Description	Rationale Viviano-Beck [106]	Additional remarks
BDI1000IR*	Divide reflectances from R1045 to R1255 by linear fit from median R (of the 15) between 1.3 and 1.87 m to median R between 2.43 and 2.6 m extrapolated backward, then integrate over (1 - normalized radiances)	Integrated band depth 1μm SWIR	Crystalline Fe2^{2} silicates	
BDI2000	Divide reflectances from R1660 to R2390 by linear fit from peak R (of 15) between 1.3 and 1.87 m to R2530, then integrate over (1 - normalized radiances) to get integrated band depth	Integrated band depth 2 μm	Pyroxene	
Olivine				
OLINDEX3*	RB1080 * 0.03 + RB1152 * 0.03 + RB1210 * 0.03 + RB1250 * 0.03 + RB1263 * 0.07 + RB1276 * 0.07 + RB1330 * 0.12 + RB1368 * 0.12 + RB1395 * 0.14 + RB1427 * 0.18 + RB1470 * 0.18 Anchor at R1750 and R2400	Broad spectral feature centered at 1 μm	Olivines will be strongly positive	Can be sensitive for high-calcium pyroxene
Pyroxenes				
LCPINDEX2*	RB1690 * 0.20 + RB1750 * 0.20 + RB1810 * 0.30 + RB1870 * 0.30 Anchor at R1560 and R2450	Broad spectral feature centered at 1.8 μm	Pyroxene is strongly positive; favors LCP	

Table 1 continued from previous page

Product	Equation	Description	Rationale Viviano-Beck [106]	Additional remarks
HCPINDEX2*	$\frac{R1470-R1050}{R1470+R1050} * \frac{R1470-R2067}{R1470+R2067}$	Broad spectral feature centered at 2.1 μm	Pyroxene is strongly positive; favors HCP	
BD920_2	1-$\left(\frac{R920}{a*R807+b*R984}\right)$	0.92 μm band depth	Crystalline ferric minerals and LCP	
Feldspar				
BD1300*	1-$\left(\frac{R1320}{a*R1080+b*R1750}\right)$	1.3 μm band depth	Plagioclase with Fe^{2+} substitution	Moderate correlation with secondary mineral products
Ferric iron				
SH600_2	1-$(\frac{a*R530+b*R709}{R600})$	0.6 μm shoulder height	Select ferric minerals	
SH770	1-$(\frac{a*R716+b*R860}{R775})$	0.77 μm shoulder height	Ferric minerals, less sensitive to LCP than SH600_2	
ISLOPE1	$\left(\frac{R1815+R2530}{W1815-W2530}\right)$	Spectral slope 1.8 - 2.5 μm	Ferric coating on dark rock	Acidic weathering of basaltic glass or bedrock exposure
Secondary minerals				
Sulfate				
BD1750_2	1-$\left(\frac{R1750}{a*R1550+b*R1815}\right)$	1.75 μm band depth	Gypsum, alunite	
BD2100_2	1-$\left(\frac{(\frac{R2120+R2130}{2})}{a*R1930+b*R2250}\right)$	2.1 μm band depth	H_2O in mono-hydrated sulfates	

Table 1 continued from previous page

Product	Equation	Description	Rationale Viviano-Beck [106]	Additional remarks
BD2265	1-$\left(\frac{R2265}{a*R2210+b*R2340}\right)$	2.265 μm band depth	Jarosite, Gibbsite, acid-leached nontronite	
BD2230	1-$\left(\frac{R2235}{a*R2210+b*R2252}\right)$	2.23 μm band depth	Hydroxylated ferric sulfate	
Phyllosilicate				
BD2190	1-$\left(\frac{R2185}{a*R2120+b*R2250}\right)$	2.19 μm band depth	Beidellite, allophane, imoglite, also kaolinite group	
BD2210_2	1-$\left(\frac{R2210}{a*R2165+b*R2250}\right)$	2.21 μm band depth	Al-OH minerals	
BD2250	1-$\left(\frac{R2245}{a*R2120+b*R2340}\right)$	2.25 μm band depth	Opal and other Al-OH minerals	
MIN2250	$minimum\left[\left(1-\left(\frac{R2210}{a*R2165+b*R2350}\right)\right),\left(1-\left(\frac{R2265}{a*R2165+b*R2350}\right)\right)\right]$	2.21 μm and 2.26 μm band depth	Opal	
BD2165	1-$\left(\frac{R2165}{a*R2120+b*R2250}\right)$	2.165 μm band depth	Pyrophyllite, kaolinite group	

Table 1 continued from previous page

Product	**Equation**	**Description**	**Rationale Viviano-Beck [106]**	**Additional remarks**
MIN2200	$minimum\left[\left(1-\left(\frac{R2165}{a*R2120+b*R2350}\right)\right), \left(1-\left(\frac{R2210}{a*R2120+b*R2350}\right)\right)\right.$	2.16 μm and 2.21 μm band depth	Kaolinite group	
MIN2345_2537	$minimum\left[\left(1-\left(\frac{R2345}{a*R2250+b*R2430}\right)\right), \left(1-\left(\frac{R2537}{a*R2430+b*R2602}\right)\right)\right.$	2.35 μm and 2.54 μm band depth	Ca/Fe carbonates; both overtones must be present	
BD2290	1-$\left(\frac{R2290}{a*R2250+b*R2350}\right)$	2.29 μm band depth	Mg, Fe-OH minerals; also CO2 ice	also carbonate overtone feature
D2300	2.3 μm drop off	Hydroxylated Fe, Mg silicates strongly >0	Also carbonate overtone feature	
Carbonate				
BD3200	1-$\left(\frac{R3320}{a*R3250+b*R3390}\right)$	3.2 μm band depth	CO_2 ice	High correlation with BD3400
BD3400	1-$\left(\frac{R3420}{a*R3250+b*R3630}\right)$	3.4 μm band depth	Carbonates	
BD3100	1-$\left(\frac{R3120}{a*R3000+b*R3250}\right)$	3.1 μm band depth	H_2O ice	Moderate correlation with CINDEX2

Table 1 continued from previous page

Product	Equation	Description	Rationale Viviano-Beck [106]	Additional remarks
CINDEX2	3.9 μm carbonate index	Carbonates will be>‘background’ values>0		
Discarded products				
BD860	$1\text{-}\left(\frac{R860}{a*R775+b*R977}\right)$	0.86 μm band depth	Select ferric minerals	Low number of pixel values after masking and lack of spatially coherent patterns
MIN2295_248	$minimum\left[\left(1-\left(\frac{R2295}{a*R2165+b*R2364}\right)\right),\left(1-\left(\frac{R2480}{a*R2364+b*R2570}\right)\right)\right.$	2.295 μm and 2.48 μm band depth	Mg carbonates; both overtones must be present	No positive band depth values
BD2500_2	$1\text{-}\left(\frac{R2480}{a*R2364+b*R2570}\right)$	2.5 μm band depth	Mg carbonates	No positive band depth values
BD640_2	$1\text{-}\left(\frac{R624}{a*R600+b*R760}\right)$	0.64 μm band depth	Select ferric minerals (especially maghemite)	error in CAT_ENVI software

Table 1 continued from previous page

Product	Equation	Description	Rationale Viviano-Beck [106]	Additional remarks

Table 1 Table indicating the summary product descriptions, equations, and rationale of the spectral feature they are describing.
Terms and abbreviations used in the equation are similar to those from the paper of Viviano-Beck [106]. R - reflectance, BD - band depth RC - central wavelength, W - wavelength, anchor points - wavelengths for which the reflectance is used to define the continuum fit

---

*Summary product explained further detail in Appendix Figure 1

Figure summary products

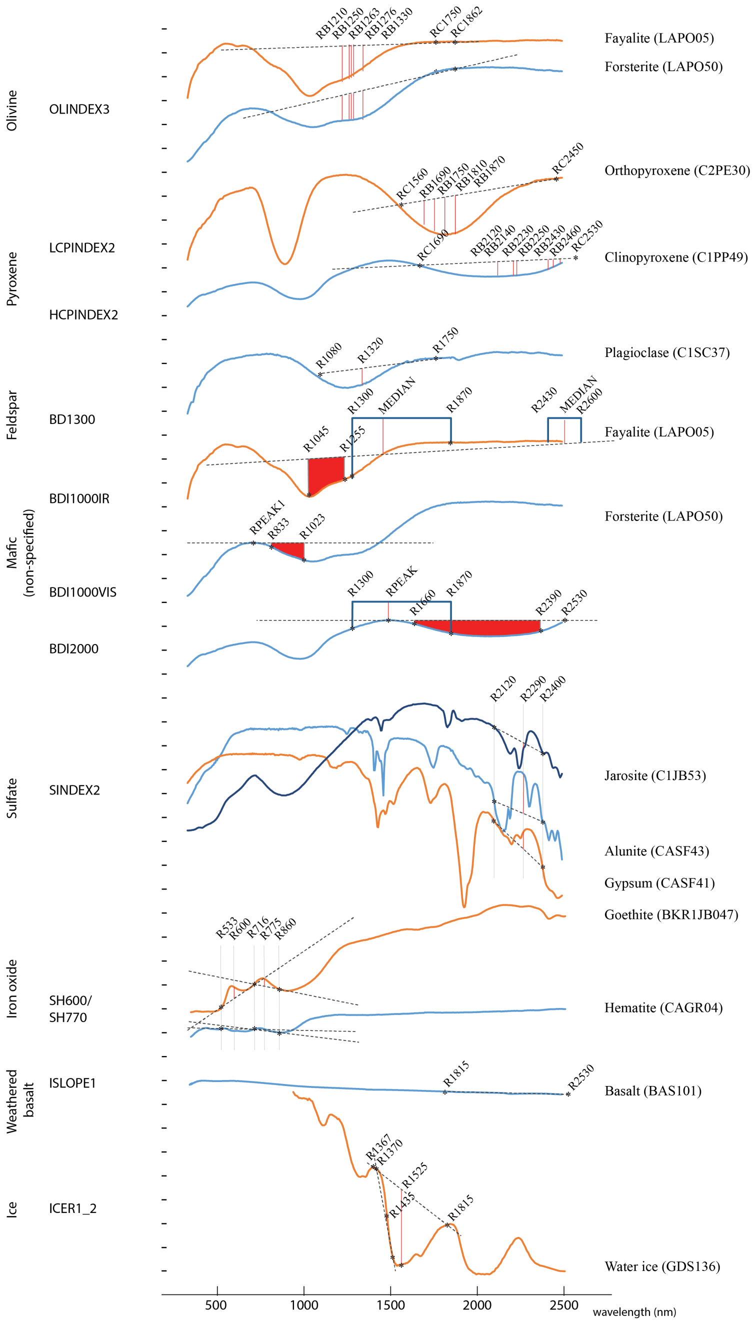

Figure 1 Formulation of summary products visualized for characteristic mineral spectra from the USGS spectral library speclib07 [60] and Horgan et al.[49]